POLITECNICO DI TORINO
DEPARTMENT OF MECHANICAL AND AEROSPACE ENGINEERING

VON KARMAN INSTITUTE FOR FLUID DYNAMICS
TURBOMACHINERY AND PROPULSION DEPARTMENT

MASTER'S THESIS

Experimental characterization of the stable operating range of a highly-loaded low-pressure compressor stage

Candidate:
NICCOLÒ FERRARI
S289390

Supervisors:
Prof. FABRIZIO FONTANETO
Mr. RICCARDO TORACCHIO
Prof. ROBERTO MARSILIO

Turin, Italy
October, 2023

Acknowledgement

Turin, Italy
October, 2023

Contents

List of Tables **7**

List of Figures **8**

Abstract **12**

Nomenclature **14**

1 Introduction **16**
1.1 General context 16
1.2 Motivation of the thesis 17
1.3 Objectives of the thesis 17
1.4 Methodology and Thesis organization 18
1.5 State of art: Aerodynamics phenomena of interest 18
1.5.1 Tip leakage flows 18
1.5.2 Hub corner separation 21

2 Experimental set-up **24**
2.1 Facility and test section 24
2.1.1 R4 facility: new configuration 26
2.1.2 DREAM booster 27
2.1.3 Test section and instrument set-up 28
2.2 Probe description and uncertainty calculation method 30
2.2.1 General uncertainty methodology 30
2.2.2 Rakes 31
2.2.3 Static Pressure taps 35
2.2.4 Traversing instrument: Pneumatic probe 36
2.2.5 Traversing instrument: Thermocouple 39
2.2.6 Fast response pressure probe 39
2.2.7 Casing Kulite pressure sensors 42
2.3 Probe Placement and acquisitions 43

3 Performance and steady-state acquisition **46**
3.1 Performance maps 48
3.1.1 Operative procedures 48
3.1.2 Parameters acquisition routine 49
3.1.3 Results 50
3.2 Span-wise distribution and maps at stator outlet using rakes 55
3.3 Span-wise distribution and performance maps at stator outlet using pneumatic probe 60

4 Detailed characterization of the flow-field at rotor exit **64**
4.1 Fast response pressure probe 64
4.2 Kulite casing sensors 72

5 Conclusions **74**

Appendix A **76**

Appendix B **78**

Appendix C **82**

Appendix D **84**

Bibliography **89**

List of Tables

2.1 Quantities characterizing the stage. 28
2.2 Normal pitch distribution of the static pressure tap 35

List of Figures

1.1 Correspondence between three-dimensional steady tip clearance flow and unsteady two-dimensional flow [1] 19
1.2 Blade pressure distribution with 0% tip clearance [2] 20
1.3 Blade pressure distribution with 4% of chord tip clearance [2] 20
1.4 Machine casing wall oil flow picture ψ=0.46 [2] 20
1.5 Machine casing wall oil flow picture ψ=0.52 [2] 20
1.6 Machine casing wall oil flow picture ψ=0.6 [2] 21
1.7 Machine casing wall oil flow picture ψ=0.68 [2] 21
1.8 Basic processes governing the formation of hub-corner-separation [3] . . . 22
1.9 Influence of incidence on the topology of separated surface flow pattern[4] 23

2.1 High Speed Compressor Facility R4 24
2.2 Detail of the DC motor and the gearbox 25
2.3 Throttle valve 26
2.4 Detail of the bypass pipes 26
2.5 Anti-surge pipe function 27
2.6 Cross-sectional view of the test section with the measurement planes . . . 29
2.7 Picture of the mechanism used to move the probes in the radial direction [5] 29
2.8 Picture of one of the outlet rakes 31
2.9 Illustration of a thermocouple device 32
2.10 Recovery factor of the outlet rakes 34
2.11 Pneumatic probe 36
2.12 Rotation of the pneumatic probe during the measurements 36
2.13 Picture of a Thermocouple 39
2.14 Active compensation configurations: Wheatstone bridge (left) and sense resistor in series with the bridge (right) [6] 40
2.15 Fast response pressure probe [7] 41
2.16 Cavity system for fast-response pressure probe 41
2.17 Typical spectrum retrieved with the FP3 probe in the VKI-R4 facility. . . . 42
2.18 Fast-response casing sensors configuration[8] 43
2.19 Rakes's head radial distribution 43
2.20 Traversing of the pneumatic probe 44

2.21 Kulite angular position . . . 45
2.22 Kulites and axial position . . . 45
2.23 Kulites axial position . . . 45

3.1 Stage total to total Pressure ratio performance map with standard deviation 51
3.2 Stage efficiency performance map with standard deviation . . . 51
3.3 Stage total to total temperature ratio performance map with standard deviation . . . 52
3.4 Performance map total to total pressure ratio with stator traversing . . . 53
3.5 Performance map efficiency with stator traversing . . . 53
3.6 Reynolds impact on averaged performance map 100Nn . . . 54
3.8 Reynolds variations . . . 54
3.9 Comparison of mass flow trends, compression ratio, and Mach number . . 55
3.10 Total pressure ratio and total temperature difference for the 2 stator pitches at 100% Nn design . . . 56
3.11 Total pressure ratio and total temperature difference 2 stator pitches at 100% Nn near stall . . . 57
3.12 Span-wise distribution of total pressure ratio and total temperature difference for one pitch. . . . 58
3.14 3D map of Pressure ratio at 100%. . . . 59
3.16 3D Map of Pressure Ratio Related to P_{t0M} at 100% Nn: . . . 60
3.18 Pitch-wise distribution of Pt4/Pt0M and Yaw angle over span obtained with a pneumatic probe at 100Nn Design point . . . 61
3.19 3D map of Pressure ratio obtained with a pneumatic probe at 100Nn . . . 62
3.21 3D map of Pressure ratio related to PT0M obtained with a pneumatic probe at 100 Nn . . . 63
3.22 3D map Yaw angle obtained with a pneumatic probe at 100Nn . . . 63

4.1 Total pressure phase locked average (PLA) map at 100% Nn . . . 65
4.3 Mach phase locked average (PLA) map at 100% Nn . . . 65
4.5 Yaw phase locked average (PLA) map at 100% Nn . . . 66
4.7 Total pressure phase locked average (PLA) map and corresponding RMS 100% Nn, design operating condition . . . 67
4.8 Total pressure phase locked average (PLA) map and corresponding RMS 100% Nn, near stall condition . . . 67
4.9 RMS signal comparison at different spans at 100% Nn . . . 68
4.11 Total pressure phase locked average (PLA) map and corresponding RMS 96% Nn, design operating condition . . . 69
4.12 Total pressure phase locked average (PLA) map and corresponding RMS 96% Nn, near stall . . . 69
4.13 PSD of the total pressure signal at midspan for 96% Nn de . . . 70

4.14 Total pressure phase locked average (PLA) map and corresponding RMS 90% Nn, design . . . 71
4.15 Total pressure phase locked average (PLA) map and corresponding RMS 90% Nn, near stall . . . 71
4.16 Wall casing static pressure ratio field at 100% Nn . . . 73

5.1 Iterative method . . . 77
5.2 Calibration curves [9] . . . 77
5.3 Total to total pressure performance map with .log file . . . 78
5.4 Efficiency performance map with .log file . . . 78
5.5 Removing outliers from total to total pressure performance map . . . 79
5.6 Removing outliers from efficiency performance map . . . 79
5.7 Example of different traces . . . 79
5.8 Raw total to total pressure performance map 100Nn . . . 80
5.9 Raw efficiency performance map 100Nn . . . 80
5.10 loading line averaging method. . . . 80
5.11 Averaged total pressure ratio performance map 100Nn . . . 81
5.12 Averaged efficiency performance map 100Nn . . . 81
5.13 Flowchart for mass flow distribution evaluation. . . . 82
5.14 Signal of $P_{central}$ after the static calibration . . . 84
5.15 Comparison between $P_{central}$ raw and $P_{central}$ after the application of the TF 85
5.16 Signal One-rev acquired with $P_{central}$ . . . 86
5.17 $P_{central}$ post TF corresponding to one revolution . . . 86
5.18 $P_{central}$ interpolated on 6080 points per revolution . . . 87
5.19 $P_{central}$ interpolated signal from fast response at 100% Nn design conditions . . . 87
5.20 PLA of pressure signal at 100% Nn design point for two different span position . . . 88

Abstract

The current environmental legislation and the growth of the aviation sector observed in the last years is demanding the development of modern aircraft architectures to reduce CO2 and NOx emissions. Short-nacelle Geared High-ByPass turbofans and Boundary-Layer-Ingestion engines have shown strong potential to overcome this problem, despite they force the engine to operate under inlet non-uniform flow conditions. Overall, a renewed interest in the analysis of distorted machines is arising in recent years as traditional methods need to be modified for the design of distortion-tolerant engines.
Despite extensive studies can be found on the front fan, the literature still lacks of information concerning the impact of real distortions on engine-representative compressors. In this context, the von Karman Institute for Fluid Dynamics is conducting leading research activities for the characterization of low-pressure compressors under distorted inflows. However, before going into the characterization of the machine under distorted conditions, it is necessary to establish a baseline understanding of the machine with a clean inlet flow, so that the impact of the distortion can be properly quantified and assessed.
The objective of this Master's Thesis is to conduct an extensive experimental campaign in the stable operating range of a high-speed low-pressure axial compressor. The main target of the present work is to provide an overview of the leading mechanisms for aerodynamic stall in clean conditions while identifying the critical flow features for stability.
Initial assessments involve the determination of the stage overall performance across different corrected speeds and operating points of the machine through time-averaged measurements. Subsequently, span-wise distributions and maps of the flow field at the rotor and stator outlet are provided by means of pneumatic and fast-response instrumentation.
From the results, it will be observed that the hub corner separation shows a critical increase close to the stability limit of the stage, due to the abrupt variation of the inlet incidence. Moreover, a tentative explanation about the development of a low total pressure region in the middle of the passage at the outlet of the stage is given.
This activity is meant to provide an experimental dataset for the analysis and characterization of highly-loaded low-pressure compressors. The outcome of the present thesis is thought to provide an important contribution to the literature and to the design of modern axial compressors.

Nomenclature

Roman Symbols

0	Total Quantities & Measurements in axial position 0
1	Measurements in axial position 1
2	Measurements in axial position 2
3	Measurements in axial position 3
4	Measurements in axial position 4
a	Speed of sound
A	Area
c	Absolute velocity
CH	Choke
D	Diameter
Hz	Hertz
$\dot{m}$	Mass-flow
Ma	Mach
Nn	Corrected speed
p	Pressure [Pa,mbar]
T	Temperature [K]
R	Radius [m]
z	Axial direction [m]
Qm	Absolute mass-flow
R	gas constant
Re	Reynolds number
u	Tangential velocity
V	Voltage & velocity
WR	Corrected mass-flow

Greek Symbols

α	Absolute yaw angle [deg]
β	Pressure ratio
Δ	Difference
η	Efficiency
μ	Dynamic viscosity $[Pa \cdot s]$
ν	Kinematic viscosity
ω	Rotation
ω_n	Natural frequency [Hz]
ρ	Density

Acronymus

BLI	Boundary layer ingestion
BPF	Blade passing frequency
CFD	Computational fluid dynamics
DE	Design conditions
DOF	Degree of freedom
HP	High-pressure
HPF	High-pass filter
IGV	Inlet guide vain
LE	Leading edge
LP	Low-pressure
LPC	Low-pressure compressors
LPF	Low-pass filter
NS	Near stall conditions
PLA	Phase Locked Average
PS	Pressure side
PSD	Power Spectrum Density
RMS	Root mean square
RPM	Revolutions per minute
SOTF	Second order transfer function
SS	Suction side
TE	Trailing edge
TLF	Tip leakage flows
TLV	Tip leakage vortex
VKI	Von Karman Institute

1
Introduction

1.1 General context

In the aviation field, the issue of reducing fuel consumption is gaining prominence. This challenge is linked to enhancing the overall efficiency of the engine, while also adhering to stringent CO2 emission regulations. Building upon this foundation, recent advancements led to new airframe-engine architectures,which will represent the next-generation aircraft:

- BLI (Boundary Layer Ingestion) engines;
- Short Nacelle Geared High by-pass Turbofan;

In a BLI aircraft the engine is integrated into the fuselage, so that the intake captures low-momentum flow from the airframe boundary-layer. Consequently, the inlet velocity and total pressure profiles become non-uniform and highly distorted. The fluid is re-energized within the engine, reducing the wasted kinetic energy in the aircraft's wake and increasing the propulsive efficiency compared with a podded engine[10]. The use of BLI engines for aircraft propulsion could enable fuel burn reductions of up to 15% compared with conventional engines.[11]

The Short Nacelle engines provide a high thrust, employing a larger fan diameter (increasing the elaborated mass flow). The short nacelle maximizes thrust-to-weight ratio employing lighter material and a smaller core component [12].
Both types of technologies show promise in terms of fuel and propulsive efficiency improvement. However, they must operate continuously under distorted conditions throughout their service life.

1.2 Motivation of the thesis

In BLI engine architecture, inlet distortions persist over a significant portion of the engine's operational lifespan, leading to adverse effects on engine performance and stability.
Despite extensive studies can be found on the front fans, the literature still lacks comprehensive information regarding the effects of distortions on compressors representative of actual engines. To quantitatively predict performance degradation and flow dynamics within a distorted compressor, it is crucial to first characterize the machine under clean inlet flow conditions. This will serve as a baseline reference for quantifying and assessing the influence of distortion.

1.3 Objectives of the thesis

This work aims to experimentally characterize a state-of-the-art booster within its stable operating range, with the goal of gaining a comprehensive understanding of the aerodynamic phenomena responsible for performance and stability reductions under a clean inlet flow.
The study will particularly focus on the design and near-stall conditions at various operating speeds. The key outcomes include:

- Compressor maps with stator traversing
- Span-wise distributions(Mach, total temperature, total pressure, incidence angle) and performance maps at the stator exit
- Span-wise distributions of Mach, total temperature, total pressure, incidence angle at rotor exit
- Time-resolved analysis with casing sensors and fast response probes at the rotor outlet.

The rotor and stator outlet, together with the rotor casing, are investigated in detail as they are the main regions where the most critical flow structures are visible.

1.4 Methodology and Thesis organization

This thesis is organized within five chapters.

- The first chapter provides an overview of the study's background, objectives, scope, and includes a literature review.
- Chapter Two offers a detailed description of the facility, focusing on the test section, and includes information about the stage's geometric characteristics, probe types, and specific measurements. It also discusses the measurement uncertainty of the probes and their spatial and temporal resolution.
- Chapter Three focuses on the performance of the stage and the steady-state acquisition:

  1 Performance maps at 100Nn, 96Nn, 90Nn by means of rakes;

  2 Span-wise distributions and 2D maps at the stage outlet by means of rake and 3-hole-virtual pneumatic probes;

  The impact of stator traversing is also investigated to understand its effect on performance and stage's outlet flow field.
- The fourth chapter describes time-resolved measurements taken at multiple locations, including the rotor casing and a fast response pressure probe traversing downstream of the rotor. These measurements hold a crucial role in the identification and characterization of the flow structures introduced in Section 1.5.
- Chapter Five presents the project's conclusions and outlines potential future steps.

1.5 State of art: Aerodynamics phenomena of interest

In highly-loaded compressors, such as the one presented in this thesis, hub corner separations, end-wall and tip-clearance flows are considered among the most detrimental phenomena impacting performance and aerodynamic stability. To enhance the understanding of the observed flow features in the investigated compressor, a concise overview of these phenomena is included.

1.5.1 Tip leakage flows

Tip leakage flow in a compressor results from the gap between the rotor tip and the casing, driven by the pressure differential between the pressure and suction sides. The presence of the clearance gap is necessary to accommodate potential blade elongation at maximum peripheral velocity.

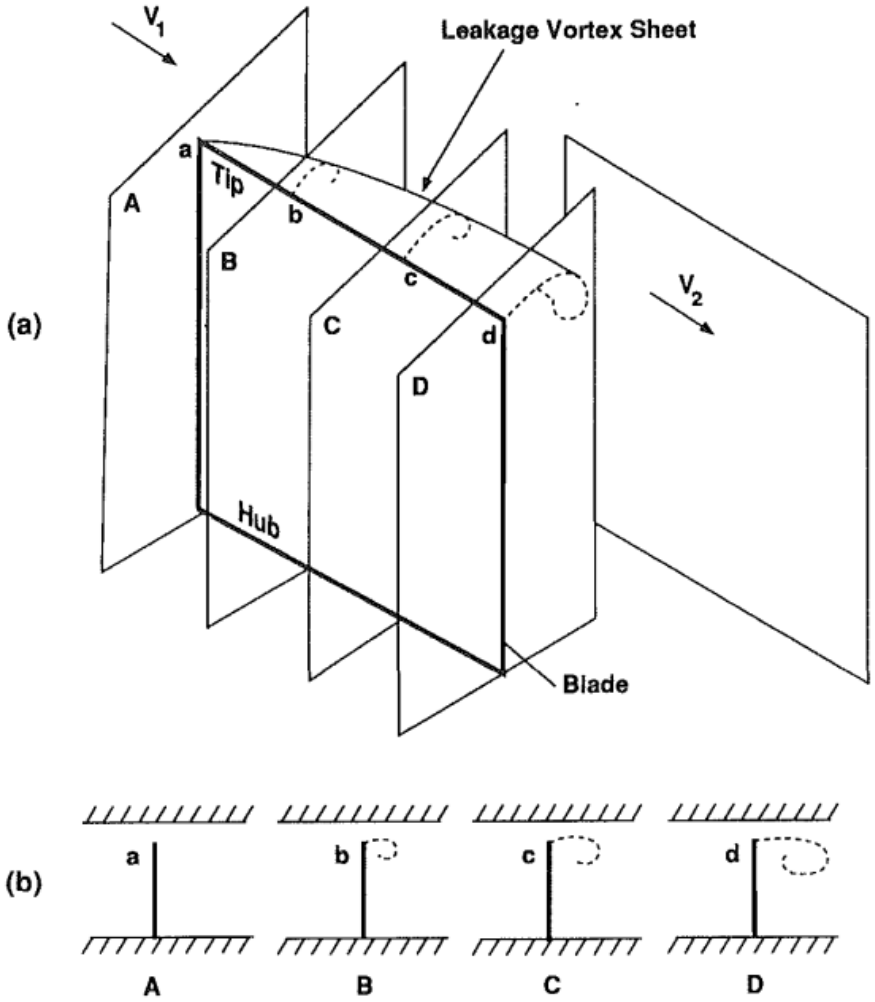

Figure 1.1: Correspondence between three-dimensional steady tip clearance flow and unsteady two-dimensional flow [1]

Examining crossflow planes A, B, C, and D at chordwise positions a, b, c, and d, as presented in fig. 1.1 upper section. Position 'a' corresponds to the leading edge, and position 'd' corresponds to the trailing edge. At station 'a', the tip clearance flow initiates, generating a flow pattern. Advancing through the blade passage, the vortex sheet shed into the clearance rolls up, yielding subsequent cross sections in planes B, C, and D as referenced in [1].
In the study conducted by J.A. Storer and N. Cumpsty [2], various tip clearances were examined. The study revealed vortex formation near the blade tip with a 4% gap between the blade and casing, whereas this vortex is absent with a 0% gap, as shown in fig.1.2 and 1.3. J.A. Storer and N. Cumpsty also observed that the location of the pressure trough shifted downstream as the tip clearance increased.

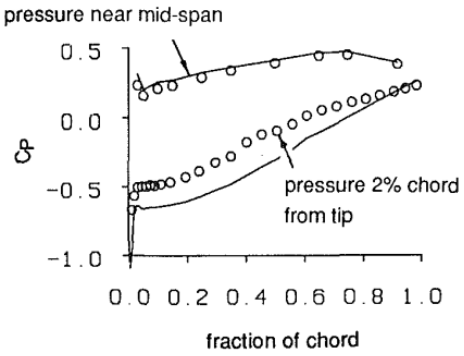

Figure 1.2: Blade pressure distribution with 0% tip clearance [2]

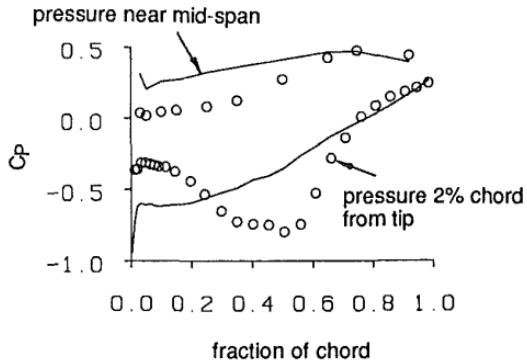

Figure 1.3: Blade pressure distribution with 4% of chord tip clearance [2]

Saathoff and Stark [13] propose a detailed study on tip clearance flow variation according to the flow rate. The position of the separation line produced by the vortex is located next to the trailing edge line at higher flow rates and moves upstream as the flow rate decreases. At flow rates close to stall the separation line is close to the leading edge. The results are presented in fig.1.4 1.5 1.6 1.7.

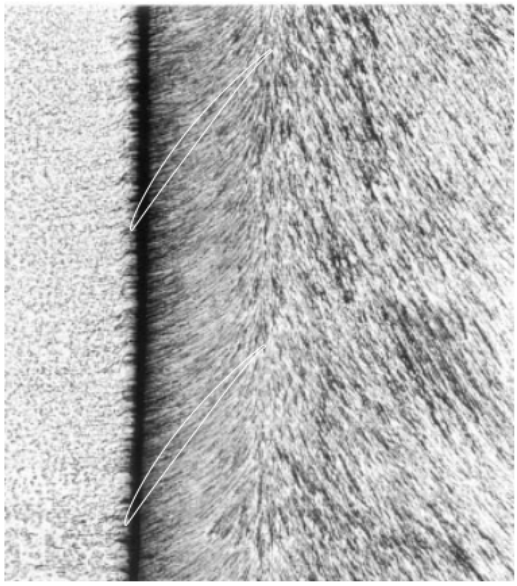

Figure 1.4: Machine casing wall oil flow picture ψ=0.46 [2]

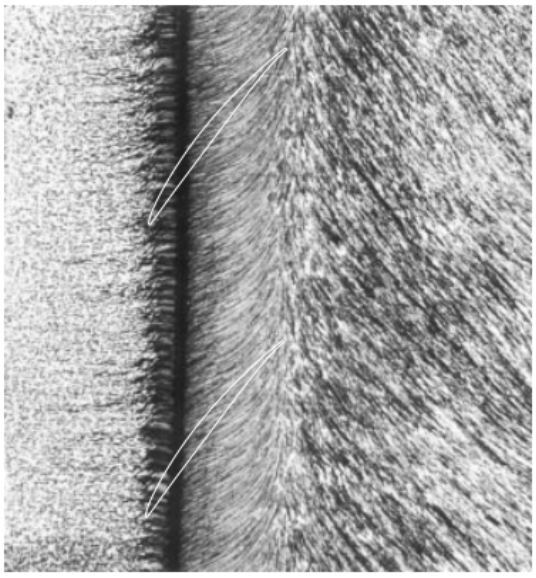

Figure 1.5: Machine casing wall oil flow picture ψ=0.52 [2]

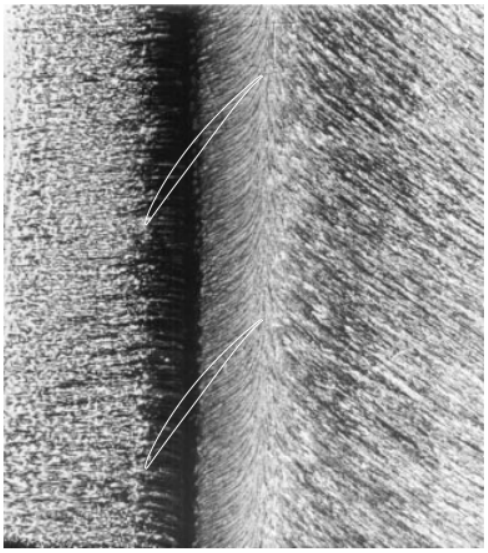

Figure 1.6: Machine casing wall oil flow picture ψ=0.6 [2]

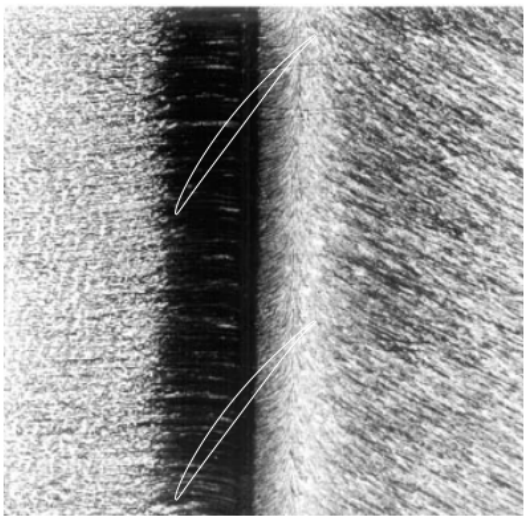

Figure 1.7: Machine casing wall oil flow picture ψ=0.68 [2]

1.5.2 Hub corner separation

The hub corner separation is a three-dimensional flow phenomenon that occurs at the end-wall corner.
The basic cause of this separation is the stagnation of low momentum fluid by such adverse gradients. If flow reversal occurs on both the blade suction surface and the endwall, the terminology used is *hub corner stall*. The primary effects that must be described to capture this phenomenon are the pressure rise and the state of the flow that is subjected to this pressure rise. In this sense the principal three-dimensional effect is the secondary flow, due to the cross passage pressure gradient, which brings low stagnation pressure, low momentum fluid, into the hub corner region.[3]
The endwall boundary layer has a lower velocity but experiences roughly the same cross-stream pressure gradient as the free stream. The streamline radius of curvature near the endwall is therefore smaller than in the free stream, leading to cross-passage motion, and the accumulation of low stagnation pressure fluid near the suction surface hub corner. At increased blade loading conditions this low stagnation pressure fluid is not able to negotiate the pressure rise in the blade passage and hubcorner stall occurs, increasing passage blockage.
This aerodynamic feature is described in fig. 1.8, which includes the limiting streamlines near the solid surfaces and the separation lines marking the region of stalled flow.

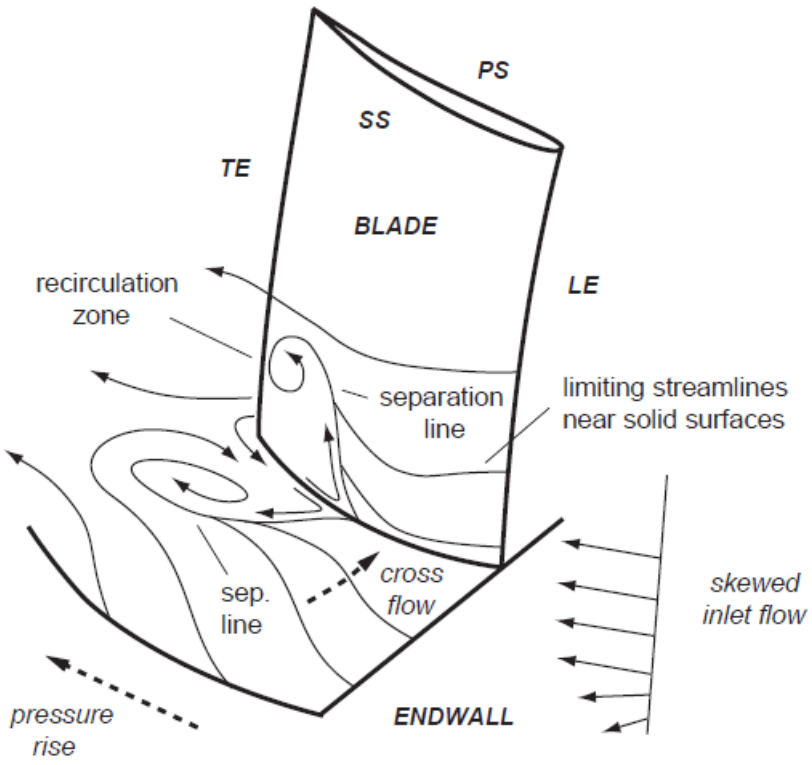

Figure 1.8: Basic processes governing the formation of hub-corner-separation [3]

In summary, the primary factors influencing the development of hub corner separation include:

- The adverse pressure gradient within the blade passage.
- The cross-flow from the pressure to the suction side
- The state and skew of the incoming end wall boundary layer flow, impacting both the strength of the cross-flow and the resistance to reversal.

Schultz et al. [14] and Gbadebo [4] examined the impact of the inlet incidence by means of the skin frictions lines on the rotor suction side and hub wall. The results are shown in fig.1.9 at different angles of incidence: -7.0, 0.0, 2.0, and 3.0 degrees.
As expected, an increase in incidence leads to a noticeable expansion of the separated region both in the chordwise direction and in the spanwise direction.

In conclusion, the literature review indicates that an increase in incidence can serve as a primary driver for the formation of critical flow structures near the hub and tip walls. Given the high blade loading in our machine, these regions will be the primary focus of the flow field analysis.

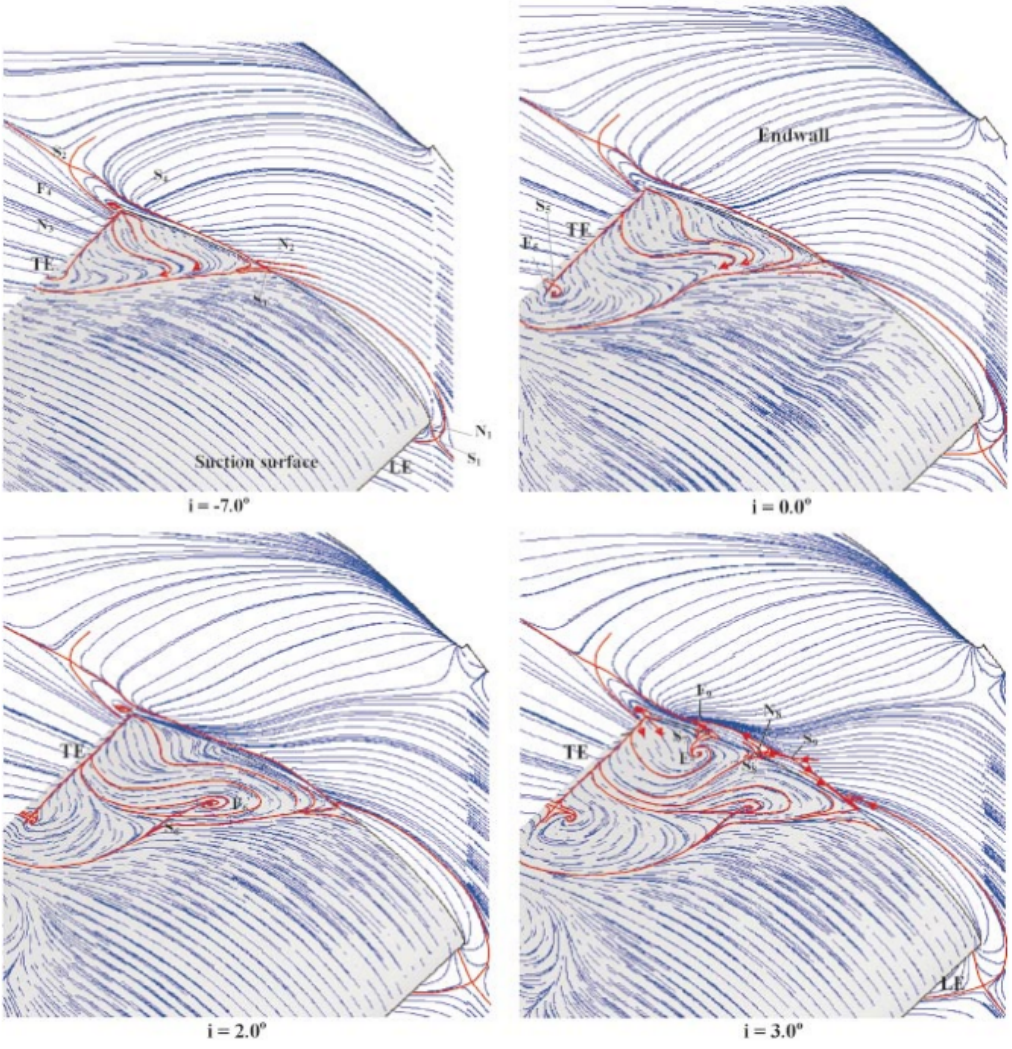

Figure 1.9: Influence of incidence on the topology of separated surface flow pattern[4]

2

Experimental set-up

2.1 Facility and test section

The VKI R4 facility, originally designed in the 1960s and upgraded in 2004, is a high-speed closed-loop test rig specifically intended for measurement campaigns on axial and radial compressors.
One of its unique features is the closed-loop configuration (fig.2.1), combined with a heat exchanger at the test-section inlet. This setup allows for independent control and variation of both Reynolds and Mach numbers, enabling the replication of realistic aircraft conditions encountered during cruise and take-off phases. The total inlet pressure is controlled using a vacuum pump/pressure source managed by an internal control system[15].

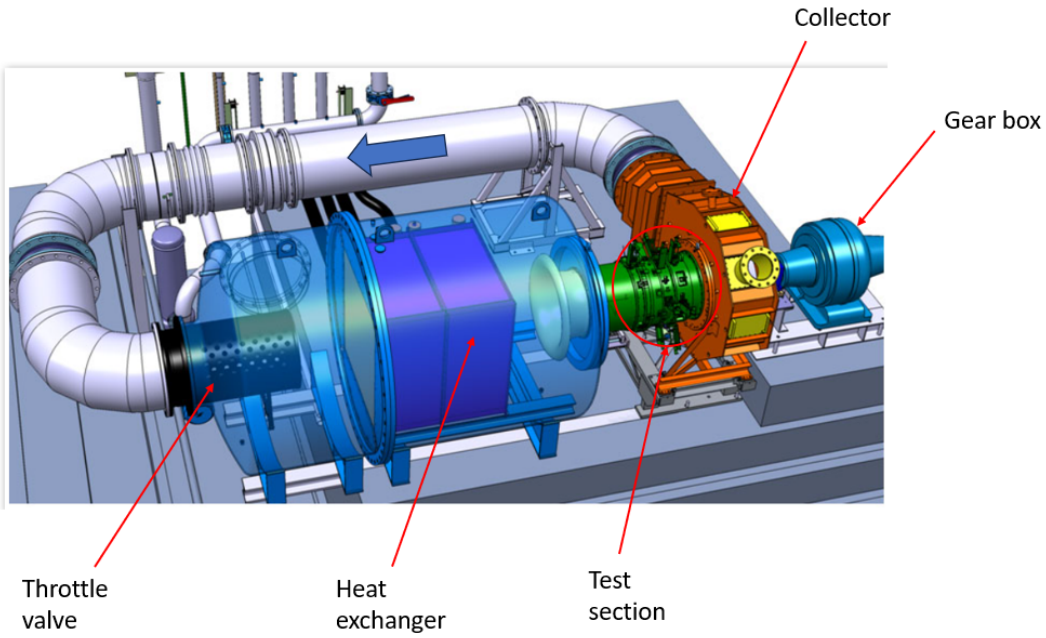

Figure 2.1: High Speed Compressor Facility R4

The compressor is powered by a 695 kW DC motor,(fig.2.2) capable of reaching a maximum rotational speed of 1000 RPM. Through a gearbox, the maximum rotational speed of the compressor can be extended to 9000 RPM. For precise monitoring and control, an optical once-per-revolution sensor is mounted on the rotor shaft. This sensor emits signals continuously monitored by a LabVIEW® routine. Additionally, a secondary oil circuit, powered by a volumetric circulator pump, provides lubrication to the bearings.

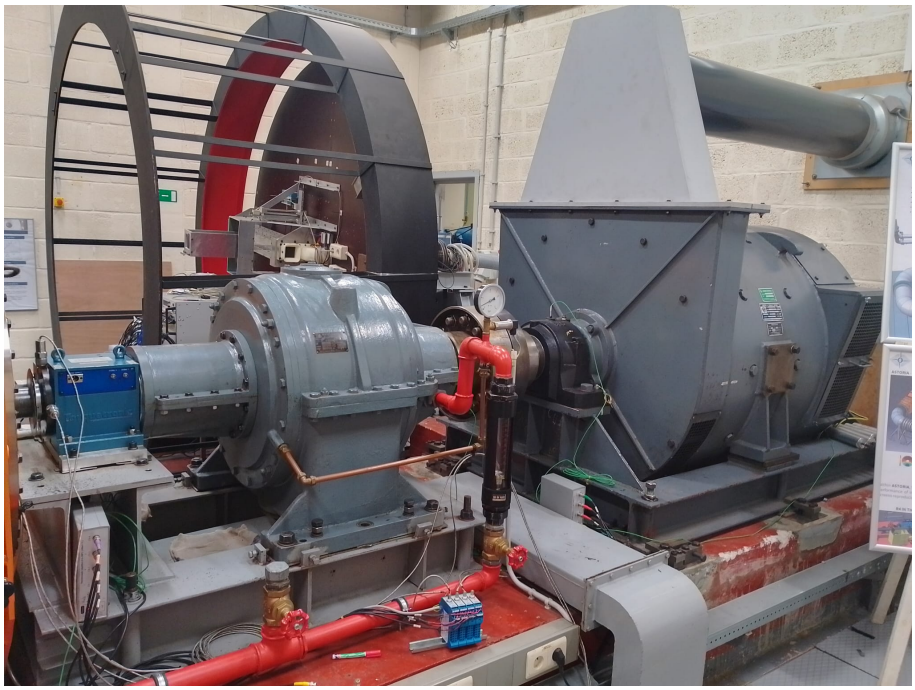

Figure 2.2: Detail of the DC motor and the gearbox

The discharged flow from the test section is collected into a collector and directed to the settling chamber/plenum through a return circuit. Mass flow at the chamber inlet is regulated by a throttle valve visible in fig.2.3. This valve includes a fixed support, a movable conical component, and a fast-opening plate. Adjusting the relative position of the conical component and the support, allows for precise control over the throttle valve's cross-sectional area and inlet mass flow. In case of surge or stall, the fast-opening plate is instantly activated to prevent potential damage.
Subsequently, the air flows into a water heat exchanger for temperature regulation. The heat exchanger features a honeycomb structure exchange surface to maximize heat transfer and reduce radial and circumferential velocity components. An additional feature permits the conversion of the closed-loop system into an open-loop configuration through a circular opening on the plenum's lateral surface.
To ensure a uniform axial flow, a convergent bell-mouth connects the plenum to the test section inlet.

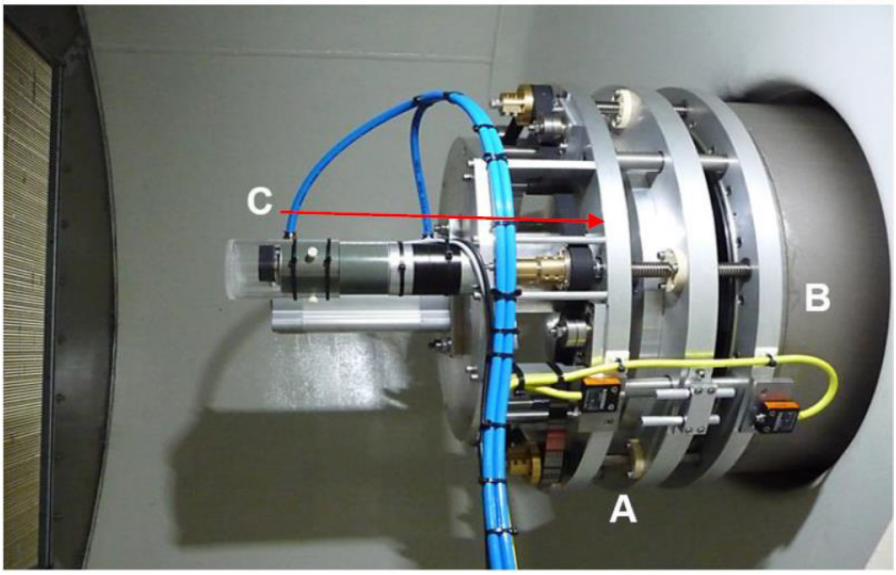

Figure 2.3: Throttle valve

2.1.1 R4 facility: new configuration

During the measurement campaign, enhancements were made to the R4 facility, including the installation of two bypass lines that connect the collector and the plenum, as reported in fig. 2.4.

Figure 2.4: Detail of the bypass pipes

One of the pipes, designated as the "Anti-surge line," serves a safety function. When the compressor operates near its stall point, a signal triggers the actuator valve to promptly open this line, thereby shifting the operating point away from the surge line, as depicted in fig 2.5. Notably, this safety feature was not utilized during the tests conducted in this thesis.

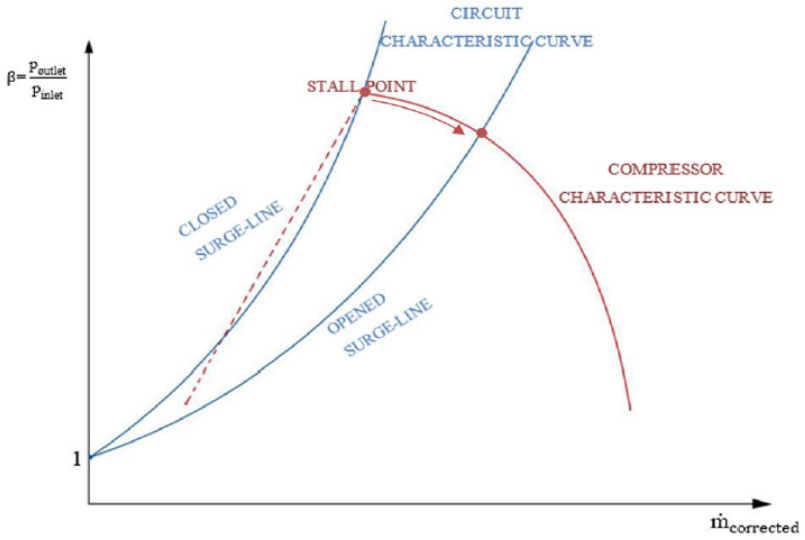

Figure 2.5: Anti-surge pipe function

The second bypass line provides a similar anti-surge function, differing primarily in valve control. The anti-surge line valve is binary, either fully open or closed. In contrast, the second bypass line employs a motor-controlled valve actuator, enabling precise mass flow adjustments. When combined with the throttle valve, this arrangement provides increased control over corrected mass flow, enhancing the system's degree of freedom.. These adjustments were essential to counteract the potential compressor stall caused by increased losses in the loop due to the presence of a second test-article positioned over the return channel.

2.1.2 DREAM booster

The DREAM booster represents the first stage of a highly-loaded low-pressure compressor, characterized by high loading and diffusion, giving rise to possible critical conditions close to the hub wall.
The booster has been scaled to fit the dimensions of the test section within the testing facility. Fixed staggered Inlet Guide Vanes (IGV) simulate the spanwise flow distribution created by the fan. The rotor blades experience an incoming relative Mach number of approximately 0.8 at the tip when the nominal rotational speed is set at 8748 rpm, equivalent to 100% of the nominal speed.
Here's a concise summary of the stage characteristics:

N IGV Blades	100
N rotor blades	76
N stator blades	100
Rotor tip gap	0.8% span
Rotor Aspect ratio	1.59
Stator Aspect ratio	1.58
Rotor solidity	1.45
Stator solidity	1.86
Nominal rotational speed (100% Nn)	8748 rpm

Table 2.1: Quantities characterizing the stage.

To account for temperature fluctuations during testing, the absolute rotational speed is continuously adjusted while keeping the corrected rotational speed constant. This adjustment is based on the standard condition as follows:

$$N_{corrected} = \frac{N_{real}}{\sqrt{\frac{T_0}{T_{0,ref}}}} \tag{2.1}$$

The reference parameters used for calculating the corrected mass flow and rotational speed are:

$$T_{0,ref} = 288.15K \qquad P_{0,ref} = 101325Pa \tag{2.2}$$

Performance maps were obtained under atmospheric pressure, temperature, and Reynolds conditions. However, during acquisition, inlet values dropped to subatmospheric levels due to loop leakage and were not subsequently adjusted to atmospheric values, despite remaining within the atmospheric range. The parameters at the inlet are used to non-dimensionalize the maps.

2.1.3 Test section and instrument set-up

The test section, illustrated in the cross-sectional view provided in fig. 2.6, is divided into measurement planes at five distinct axial positions:

- Far upstream the IGV (plane 0)
- At the IGV inlet (plane 1)
- At the rotor inlet (plane 2)
- at the rotor outlet (plane 3)
- at the stator outlet (plane 4)

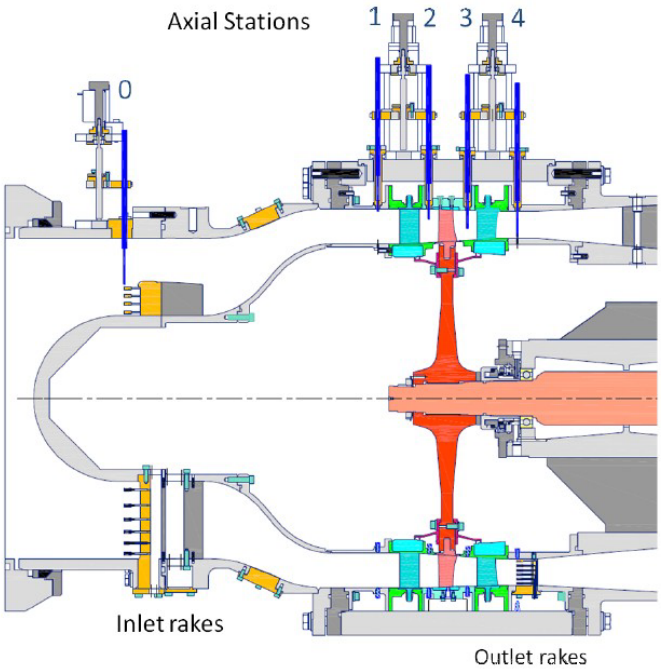

Figure 2.6: Cross-sectional view of the test section with the measurement planes

Probe traverses are available at four circumferential positions (0°, 90°, 180°, 270°) at each measuring plane, in which 0° is located at the top. A representation of the traversing system for the probes is reported in fig.2.7.
Within the experimental setup, a motor enables the stator and IGV (Inlet Guide Vane) blades to rotate relative to each other, allowing adjustments of up to 2 pitches to conduct compressor tests under different stator positions. It's important to note that, in the present test-section, the clocking between IGV and stator is fixed, and their relative position remains constant during operation. Both are therefore able to move in the tangential direction by the same amount.

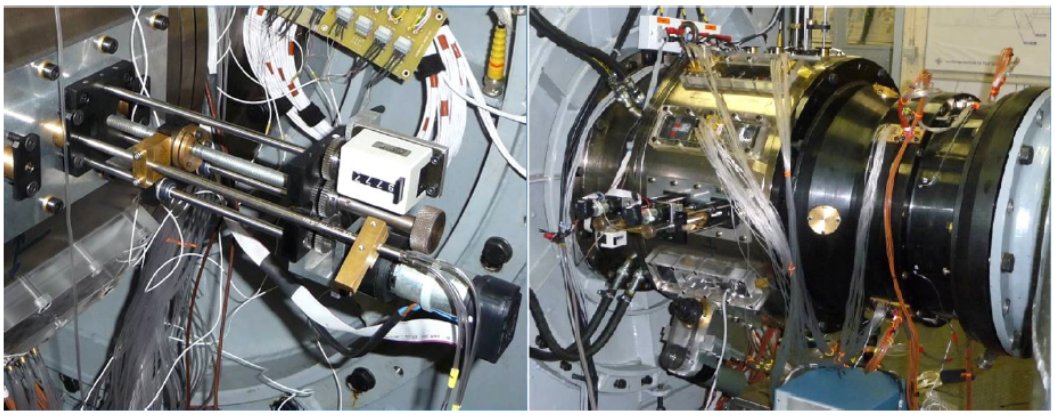

Figure 2.7: Picture of the mechanism used to move the probes in the radial direction [5]

2.2 Probe description and uncertainty calculation method

This section outlines the uncertainty related to the instrumentation used within the compressor and their respective placements. The instruments can be categorized into two groups:

- Steady-state acquisition instrumentation (Rakes, Pressure taps, Pneumatic probe, Thermocouple)
- Unsteady acquisition instruments (Fast-response pressure probe, Casing sensors)

2.2.1 General uncertainty methodology

The uncertainty methodology follows ASME guidelines, categorizing error sources into random and systematic errors (bias).

- Random errors arise from the dispersion of data samples around the mean value, acquired using the same measurement chain and conditions. Random errors, albeit unavoidable, can be mitigated with a large sample size.
  Evaluating random errors, it's essential to confirm that the dataset conforms to a Gaussian distribution. They are estimated as the standard deviation from the mean value.

$$e_r = \frac{\sum_{i=1}^{N}(x_i - \bar{x})^2}{N \cdot (N-1)} \tag{2.3}$$

  Here, N represents the number of data points, x_i is the i-th measurement value, and $\bar{x}$ signifies the overall average of the collected data.

- Systematic errors are determined considering accuracy or using the uncertainty provided in the manufacturer's instrument datasheet or prior calibration data. Denoted as b_i the systematic error of the i-th source, the total uncertainty is determined as follows:

$$e_s = \sqrt{\sum_{i=1}^{N} b_i^2} \tag{2.4}$$

The combined uncertainty, originating from both systematic and random errors, is determined as:

$$e_{tot} = \sqrt{e_s^2 + e_r^2} \tag{2.5}$$

In cases where a derived result, y, depends on other variables through a mathematical function y=f(x1, x2,. . . .xn), the uncertainty of the individual variable is propagated to the result using the following formula:

$$\delta y = \sqrt{(\frac{\delta y}{\delta x_1} \cdot \delta x_1)^2 + ...(\frac{\delta y}{\delta x_n} \cdot \delta x_n)^2} \tag{2.6}$$

2.2.2 Rakes

Four Rakes are strategically positioned in planes 0 and 4, inlet and outlet of the stage, (0°, 90°, 180°, 270°), each of them is equipped with six Kiel heads featuring an outlet diameter of 2.2 mm, fig.2.8 shows a rake in detail. Each Kiel head incorporates a Pitot tube and a T-type thermocouple junction, enabling the measurement of both total pressure and total temperature.

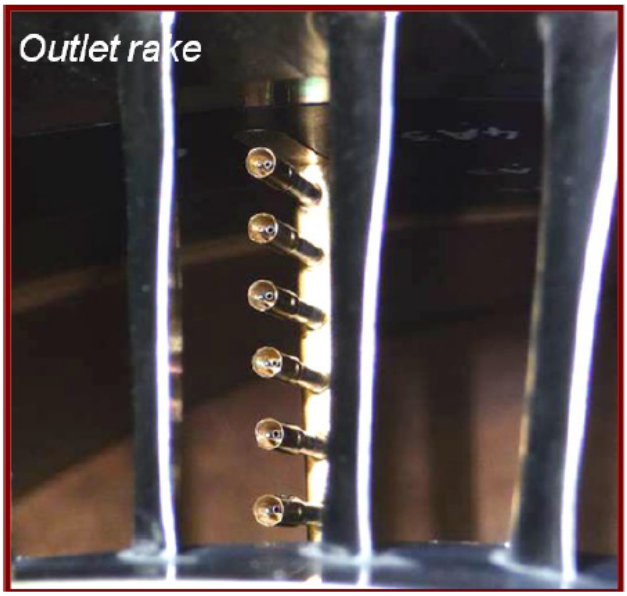

Figure 2.8: Picture of one of the outlet rakes

2.2.2.1 Rakes: Total Pressure

The physical principle of the rakes is similar to the Pitot probe.
When the airflow is aligned with the rake's head, a stagnation point is formed precisely at the location of the pressure tap. Consequently, the local pressure matches the total pressure, as the total kinetic energy is converted into pressure energy, in accordance with Bernoulli's equation.
These measurements, recorded at a 2 Hz sampling frequency, are connected to a pressure and temperature scanner. Based on these measurements in plane 0 and plane 4, parameters such as mass flow, efficiency, Mach number, and pressure ratio are continuously calculated and displayed on a screen every 0.5 seconds. This real-time data presentation enables the operator to monitor the compressor's behavior.
The operational principle of the rakes resembles that of a Pitot probe, but Pitot tubes are typically sensitive to the angle between the flow direction and the tap cavity, leading to measurements between total and static pressures when not perfectly aligned. In contrast, the rakes use a Kiel head design with a shroud shielding the pressure tap. This design efficiently redirects the flow with minimal losses toward the intake section of the probe,

allowing accurate measurement of total pressure within a specific range of flow angles (20°) while remaining insensitive to deviations.

2.2.2.2 Rakes: Total Temperature measurements

To measure the total temperature across the spans of planes 0 and 4, T-type thermocouple transducers are securely positioned within all rake heads. Thermocouples operate based on the Seebeck effect, which manifests when two dissimilar metals are integrated into an open-loop circuit.
A detailed representation of a thermocouple device is depicted in fig. 2.9.

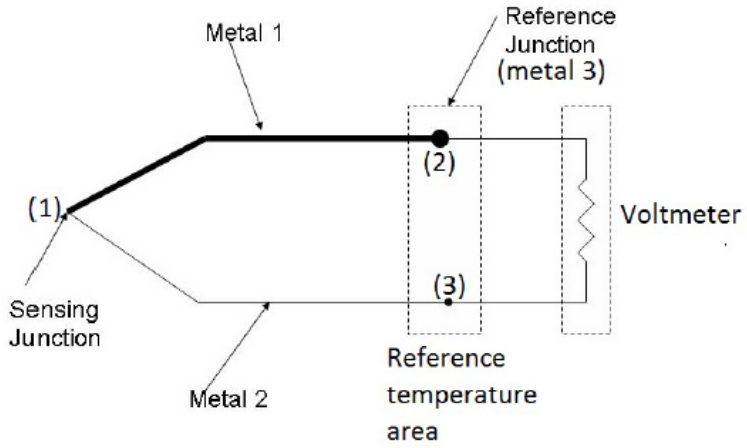

Figure 2.9: Illustration of a thermocouple device

This device consists of two different metal wires fused at one of their extremities, called the sensing junction (1).This junction is positioned at the desired location for measurements. The other ends of these wires are joined to a third metal, situated in a reference temperature zone where the temperature is precisely known and constantly maintained. This ensures that the two wire extremities (2) and (3) are identical in terms of composition and temperature. Voltage measurements are acquired at (2) and (3), and since these two endpoints are indistinguishable in composition and temperature, they have no impact on the overall voltage difference.
If the voltmeter were directly connected to the wire ends without a reference temperature area, the measured voltage would be affected by the voltmeter's temperature, which can change over time. In the current measurement circuit, the voltage difference depends solely on the temperature difference between the reference temperature and the sensing junction (1). This voltage difference is determined by the following equation:

$$V_3 - V_2 = \int_{T_{ref}}^{T_j} S_A(T) - S_B(T)\, dT \tag{2.7}$$

Where S_A and S_B represent the Seebeck coefficients of metals A and B (dependent on temperature), T_j denotes the temperature of the sensing junction (1), and T_{ref} signifies the reference temperature.
Various types of thermocouples can be constructed using different combinations of metals, each offering unique properties such as sensitivity, cost, resistance to oxidation, mechanical durability, etc. The thermocouples employed in the rake heads are of T-type and are constructed from copper and constantan (a copper-nickel alloy). Their temperature range spans from -200 °C to 350 °C. These thermocouples have a sensitivity of approximately 43 μV per degree Celsius. Due to this low voltage level, an amplification system is integrated into the measurement chain to enhance sensitivity per degree Celsius.

It is essential to consider also the deceleration process in relation to the total temperature evaluation. This deceleration process is non-adiabatic, meaning that the fluid is never brought to a complete rest. Consequently, not all of the kinetic energy present in the fluid is entirely converted into static temperature. A significant portion of this kinetic energy dissipates due to viscosity-related effects, influenced by factors such as the geometric characteristics of the rake heads and the flow behavior. This causes the temperature at the sensing junction T_j to deviate from the flow's total temperature T_0. This deviation can be quantified using the temperature recovery factor determined under different flow conditions, as shown in the equation:

$$r(Ma, \gamma) = \frac{T_j - T}{T_0 - T} \tag{2.8}$$

Where T_0 represents the total temperature of the flow, T is the static temperature, and T_j is the temperature of the thermocouple's junction, different from T_0 due to the velocity error.
The recovery factor of the rakes is illustrated in fig.2.10. A well-designed probe exhibits a recovery factor close to 1.
A protective shield is also applied to the rake head, housing both the total pressure tap and the thermocouple. This shielding arrangement serves a dual purpose: firstly, it enhances the recovery factor, optimizing measurement accuracy, and secondly, it reduces the rake's sensitivity to variations in the flow's relative yaw angle concerning the rake heads.
Once the temperature recovery factor of the rakes is determined for different flow conditions, it is possible to relate the temperature of the thermocouple's junction to the total temperature of the flow using equation 2.8.
As previously mentioned, temperature measurements in the VKI R-4 facility setup are acquired using a Scanivalve Temperature Digital Scanner (22 bits) [16]. This scanner includes a Uniform Temperature Reference (UTR) , which is a passive element consisting of an isothermal block housing the cold junction [17].

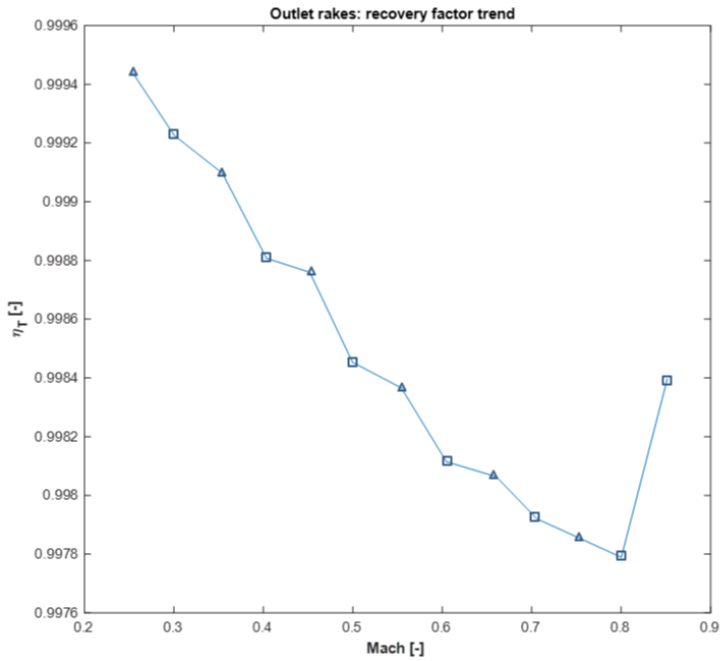

Figure 2.10: Recovery factor of the outlet rakes

2.2.2.3 Rakes: Uncertainty on the total pressure measurements

The inlet rakes are connected to a 2.5 psi relative pressure scanner, while the outlet rakes are connected to a 15 psi pressure scanner. The measurement is obtained using:

$$P = P_{transducer} + P_{atm} \tag{2.9}$$

The uncertainty is therefore computed with the contributions of the two sources:

$$\delta P = \sqrt{(\delta P_{transducer})^2 + (\delta P_{atm})^2} \tag{2.10}$$

The manufacturer reports the uncertainty value as 0.5% on the full range of the transducer:

$$\delta P_{transducer\,inlet} = 5[psi] \cdot \frac{0.5}{100} = 0.025[PSI] = 1.7mbar \tag{2.11}$$

$$\delta P_{transducer\,outlet} = 15[psi] \cdot \frac{0.5}{100} = 0.075[PSI] = 5.2mbar \tag{2.12}$$

The ambient pressure is measured by means of a Druck DPI 150 precision pressure indicator with an uncertainty of:

$$\delta P_{atm} = 0.75mbar \tag{2.13}$$

Using now equation 2.10 The resulting uncertainty on total pressure measurements are:

$$\delta P_{inlet} = \sqrt{(\delta P_{transducer\,inlet})^2 + (\delta P_{atm})^2} = 1.85mbar \tag{2.14}$$

$$\delta P_{outlet} = \sqrt{(\delta P_{transducer\,outlet})^2 + (\delta P_{atm})^2} = 5.25mbar \tag{2.15}$$

2.2.2.4 Rakes: Uncertainty on the total temperature measurements

When the rake conducts total temperature measurements during compressor operation, the recorded value is adjusted using the recovery factor r(eq.2.8):

$$T_0 = \frac{T_{meas}}{r(Ma, \gamma)} \tag{2.16}$$

From Equation 2.16, the measurement uncertainty relies on both the uncertainty associated with the measured temperature and the recovery factor. Consequently, remembering Equation 2.6, the total temperature uncertainty is derived as:

$$\delta T_0 = \sqrt{(\frac{\delta T_0}{\delta T_{meas}} \cdot \delta T_{meas})^2 + (\frac{\delta T_0}{\delta r} \cdot \delta r)^2} \tag{2.17}$$

2.2.3 Static Pressure taps

Each axial measurement plane is equipped with static pressure taps at both the hub and casing. In plane 0, there are eight taps, while in planes 1, 2, 3, and 4, there are five. These static pressure taps are distributed circumferentially to cover a single stator pitch. Given the stator's configuration with 100 blades, there is a 3.6° angle between each blade. After determining the angle for each pressure tap, it can be normalized with respect to the pitch angle. Floor means to take only the decimal part. The results are shown in table 2.2.

$$\alpha = angle\,of\,the\,Pressure\,tap \quad \beta = Rotor\,pitch\,angle = 3.6 \tag{2.18}$$

$$\beta_{norm} = \frac{\alpha}{\beta} - floor(\frac{\alpha}{\beta}) \tag{2.19}$$

Static pressure tap	β_{norm}[Deg]
1	0.33333
2	0.66666
3	0.83333
4	0
5	0.16666

Table 2.2: Normal pitch distribution of the static pressure tap

Static Pressure taps: Uncertainty

As this instrument is similarly connected, like the outlet rakes, to a pressure scanner operating with a maximum capacity of 15 psi,please refer to the previous section for the measurement of the uncertainty.

2.2.4 Traversing instrument: Pneumatic probe

Figure 2.11: Pneumatic probe

The pneumatic probe is a cylindrical device with a single port located near its tip, enabling measurements within the flow boundary layer. As previously discussed in section 2.1.3, radial measurements are achieved through electrical mechanisms.
Additionally, the probe can be rotated around its axis, enabling its use in a virtual 3-hole configuration to replicate the behavior of a three-hole pressure probe, as depicted in fig.2.12.

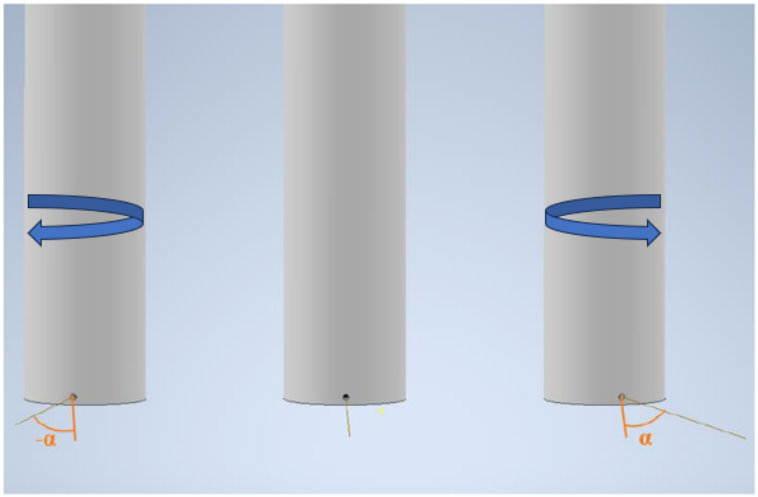

Figure 2.12: Rotation of the pneumatic probe during the measurements

In this configuration, pressure measurements are taken while the probe is rotated by a user-defined angle (α). This enables the measurement of pressures in the central hole ($P_{central}$) and the hypothetical lateral stem ports of a bidirectional probe (P_{left} and P_{right}). The 3 hole-virtual probe provides information about flow direction and Mach number by combining total and static pressure measurements with aerodynamic calibration.

To ensure that the probe remains within the specified angular calibration range during rotation, it is initially positioned axially in plane 4 and set at 33°. This angular setting corresponds to the averaged outlet flow angle at the rotor mid-span, specifically at the rotor outlet.
The probe needs to be calibrated through the following steps:

- Static Calibration: The primary objective of this step is to establish a linear correlation between the probe's output voltage and pressure.
- Aerodynamic Calibration: is vital for establishing a correlation between the probe outputs, flow direction, and Mach number. It is explained in detail in Appendix A.

Pneumatic probe: Uncertainty

Once the pneumatic probe is traversed into the DREAM test section at a specific radial position, an external motor starts the probe's rotation, while the scanner records measurements for $P_{central}$, P_{left}, and P_{right}. Given that the instrument remains unchanged, it follows that all these measurements share the same level of systematic uncertainty:

$$\delta P_c = \delta P_l = \delta P_r = \delta P_{meas} = e_{s,scanner} \tag{2.20}$$

$$\delta P_{avg} = \frac{\sqrt{2}}{2} \cdot \delta P_{meas} \tag{2.21}$$

The yaw angle, denoted as α, is a function of both Mach number and Kyaw. Therefore, recalling equation 2.6, the uncertainty calculation for α is as follows:

$$\delta\alpha = \sqrt{(\frac{\delta\alpha}{\delta K_{yaw}} \cdot K_{yaw})^2 + (\frac{\delta\alpha}{\delta Ma} \cdot Ma)^2} \tag{2.22}$$

The value of K_{yaw} depends on the pressure measurements and K_{yaw} itself:

$$\delta K_{yaw} = \frac{\delta P_{meas}}{P_c - P_{avg} \cdot \sqrt{2 + \frac{3}{2}K_{yaw}^2}} \tag{2.23}$$

In the same way δK_{tot} and δK_{din} can be computed:

$$\delta K_{tot} = \sqrt{(\frac{\delta K_{tot}}{\delta\alpha} \cdot \delta\alpha)^2 + (\frac{\delta K_{tot}}{\delta Ma} \cdot \delta Ma)^2 + \delta K_{tot,meas}} \tag{2.24}$$

$$\delta K_{dyn} = \sqrt{(\frac{\delta K_{dyn}}{\delta \alpha} \cdot \delta \alpha)^2 + (\frac{\delta K_{dyn}}{\delta Ma} \cdot \delta Ma)^2 + \delta K_{dyn,meas}} \tag{2.25}$$

Where K_{tot} and K_{dyn} arrive from:

$$K_{tot}(Yaw, Ma) = \frac{P_0 - P_{central}}{P_{central} - P_{avg}} \tag{2.26}$$

$$K_{dyn}(Yaw, Ma) = \frac{P_s - P_{avg}}{P_0 - P_{avg}} \tag{2.27}$$

Using the K_{tot} and K_{dyn} definitions, the total pressure can be retrieved:

$$\delta P_{tot} = \sqrt{[(P_c - P_{avg}) \cdot \delta K_{tot}]^2 + [\frac{3 \cdot K_{tot}^2}{2} + 2K_{tot} + 1] \cdot \delta P_{meas}^2} \tag{2.28}$$

The new Mach number is then computed using the updated pressure values and their respective uncertainties, applying the uncertainty propagation expressed in Eq. 2.29. It's worth noting that the limitation of this procedure lies in the potential accumulation of uncertainty resulting from the iterative process, which continues until the residual Mach number reaches the predefined threshold

$$\delta Ma = \delta P_{meas} \cdot \sqrt{\frac{\gamma - 1}{2\gamma^2}} \cdot [(\frac{P_c}{P_{avg}})^{(1-\gamma)/1}]^{-\frac{1}{2}} \cdot \sqrt{(P_{avg})^{\frac{1-\gamma}{\gamma}} (P_c)^{\frac{2}{\gamma}} + ((P_{avg}^{\frac{1-2\gamma}{\gamma}}) \cdot (P_c^{\frac{\gamma-1}{\gamma}}))^2} \tag{2.29}$$

This comprehensive methodology is crucial for ensuring precise measurements in the complex aerodynamic environment of the compressor, particularly when dealing with a 3-hole virtual probe.

2.2.5 Traversing instrument: Thermocouple

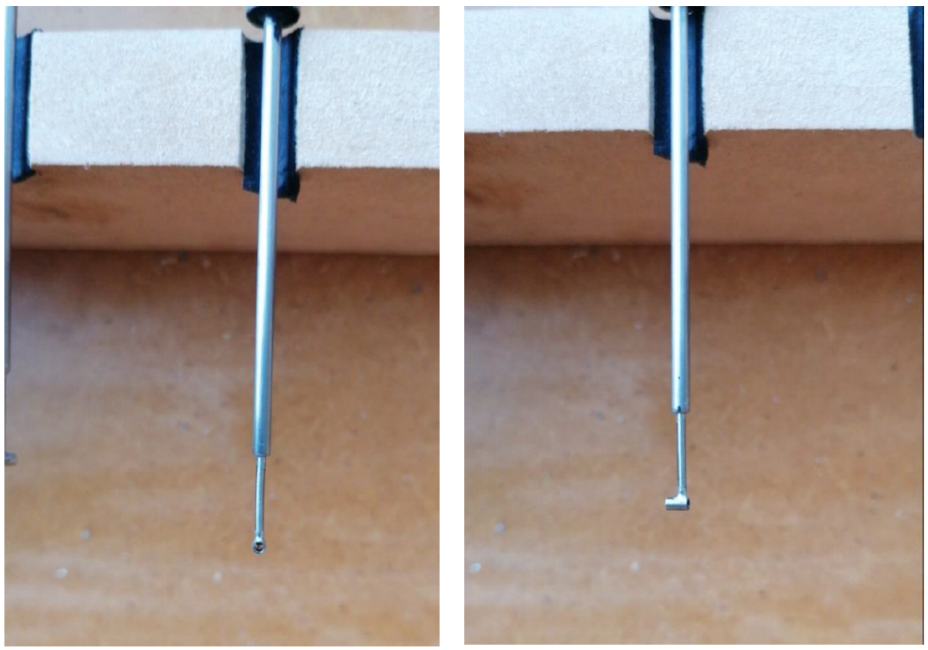

Figure 2.13: Picture of a Thermocouple

The thermocouple design, in fig.2.13, shares similarities with the rake configuration by incorporating a Kiel head to minimize the influence of flow angles on total temperature measurements.
Furthermore, the thermocouple utilized corresponds to the T-type employed in the rake probes, allowing for the replication of the same setup used in the previously described aerodynamic calibration. Notably, the outer head diameter of the thermocouple is smaller than that of the rakes. This reduction in size results in less perturbation of the flow field during instrument insertion.
As mentioned for the pneumatic probe the radial measurements are realized by means of electrical mechanism.
In contrast to pneumatic probes, thermocouples do not require rotation about their own axes, as our primary concern pertains solely to temperature evaluation rather than the assessment of flow angles.
The measurement methodology employed for this probe mirrors the procedure used for the rakes described in Section 2.2.2.2.

2.2.6 Fast response pressure probe

The flow field's detailed characterization involves time-resolved measurements, recquiring the use of a fast-response pressure probe. This probe can operate at pressures up to 25 PSI and was configured with a sampling frequency of 500 kHz.

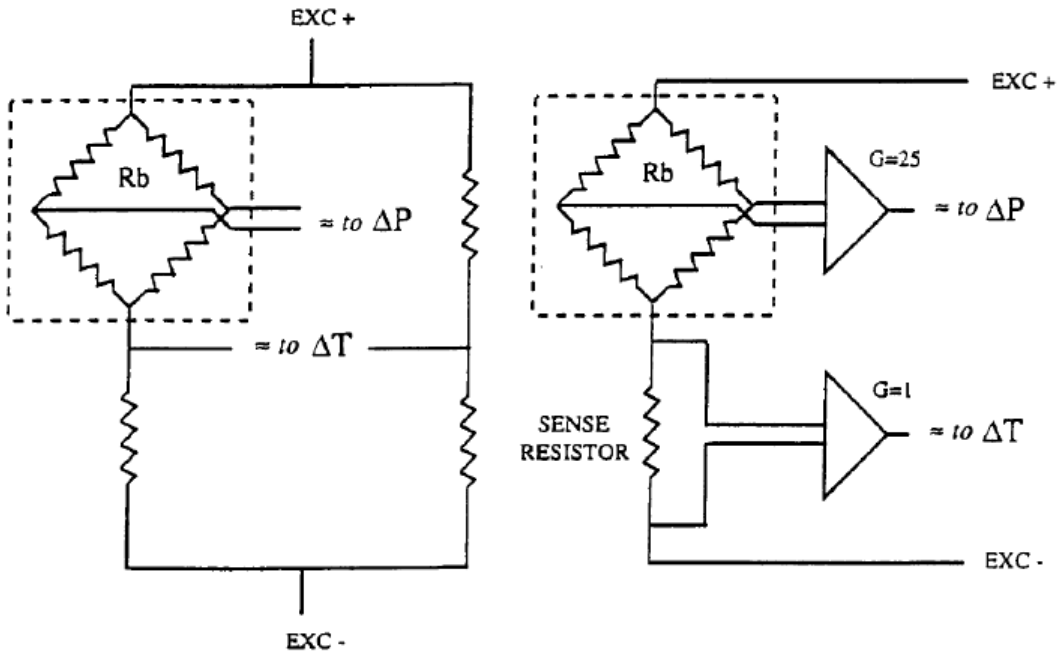

Figure 2.14: Active compensation configurations: Wheatstone bridge (left) and sense resistor in series with the bridge (right) [6]

Fast-response pressure probes typically feature silicon-piezoresistive sensors, consisting of a silicon diaphragm with four strain gauges arranged in a Wheatstone bridge configuration. Diaphragm deflection causes changes in strain gauge resistance and generates an output voltage proportional to the applied pressure. Notably, this sensor type is sensitive to temperature variations due to the temperature-dependent resistance of its elements. To mitigate this sensitivity, compensation methods can be employed:
Passive compensation involves providing a pre-corrected voltage to counteract temperature effects, typically through the use of external resistors to reduce the bridge's sensitivity to temperature. Manufacturers often supply passive compensation modules.
Active compensation, conversely, entails characterizing the sensor's temperature sensitivity and numerically correcting it during post-processing. This can be achieved by incorporating the Wheatstone bridge within an external Wheatstone bridge. A simpler approach is to use a resistor in parallel with the sensor bridge, where the voltage across the resistor remains proportional to the sensor's temperature. Both active compensation methods are reported in fig 2.14. In our case the double Wheatstone bridge method is utilized for active compensation.

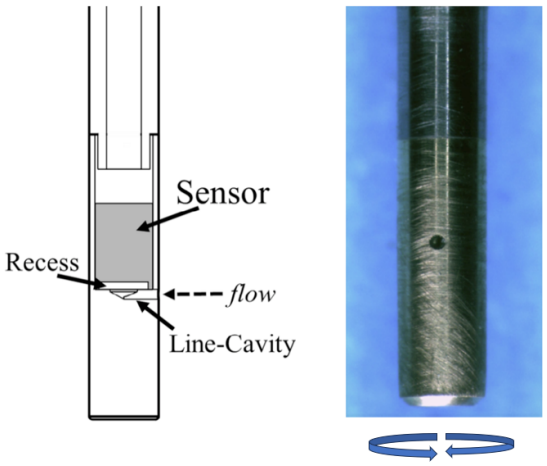

Figure 2.15: Fast response pressure probe [7]

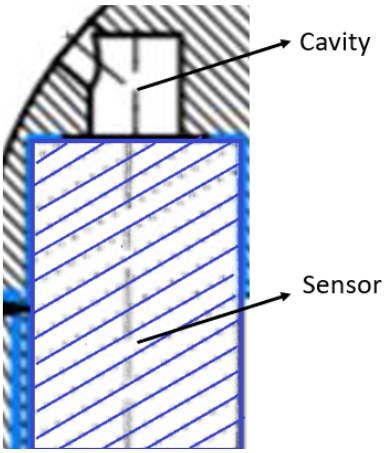

Figure 2.16: Cavity system for fast-response pressure probe

As shown in fig. 2.15 and 2.16, the transducer's sensing membrane is not flush-mounted but recessed within the transducer packaging, resulting in an additional cavity volume that significantly influences the probe's dynamic response performance.
Despite being a single-hole probe, it was used in virtual mode to mimic a multi-hole pressure probe's behavior. For these purposes, calibration included static calibration, aerodynamic calibration, and dynamic calibration. Dynamic calibration was conducted to comprehend the probe's dynamic behavior and define the instrument's frequency response function, with specific consideration of the cavity's presence.

2.2.6.1 Probe frequency response

The spectrum obtained at the VKI-R4 facility using the mentioned probe is presented in fig. 2.17. The power spectral density (PSD) is computed from data acquired at a 500 kHz sampling rate during a 1-second duration. The sensor's natural frequency is estimated to be approximately 300 kHz. As our focus lies on phenomena characterized by lower frequencies and not above 5 Blade Passing Frequencies (BPF), the decision was made to limit the bandwidth to 60 kHz using a low-pass filter.

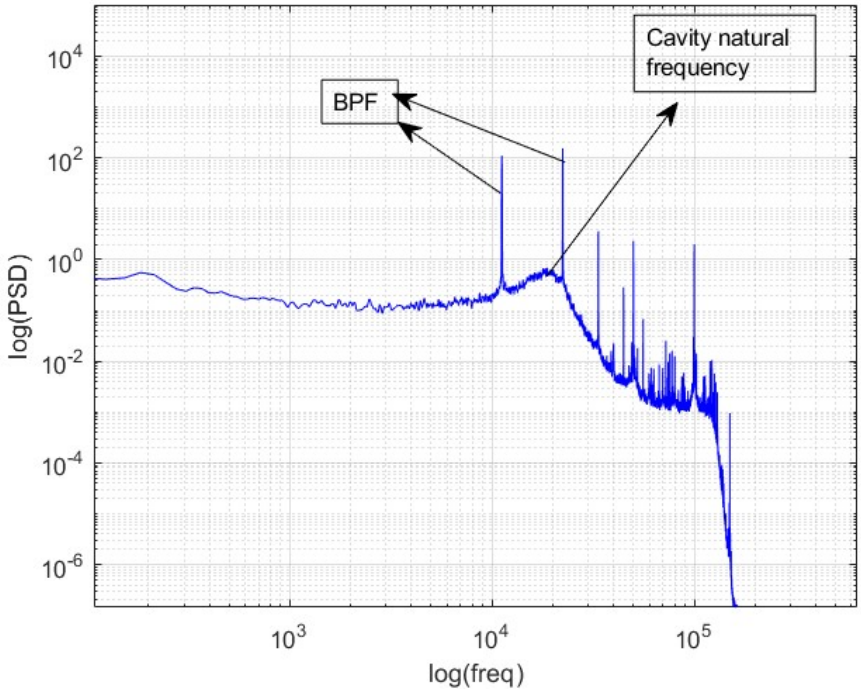

Figure 2.17: Typical spectrum retrieved with the FP3 probe in the VKI-R4 facility.

2.2.7 Casing Kulite pressure sensors

As mentioned in the introduction, even in the stable operating points of the booster, many unsteady phenomena arise, and the region where vortex formations are expected to occur is the tip. In order to measure the unsteady static pressure on the rotor casing, it is imperative to employ a sensor with a sufficiently high bandwidth. Having a nominal rotational speed of 8748 RPM with 76 rotor blades, results in a Blade Passing Frequency (BPF) of 11080.8 Hz. Therefore, the use of a sensor with a significantly high bandwidth, along with its harmonics, is crucial for the effective detection and analysis of phenomena associated with these frequencies.

The set-up instrumentation includes 15 Kulite sensors mounted in the rotor casing (for the present experimental campaign only 8 of them were correctly working). The Kulite (model XCS-062) is a 15 PSI (1034 mbar) piezo-electric differential transducer (fig. 2.18). The piezoresistive transducer mechanism consists of a diaphragm that divides the pressure measurement from a reference pressure side. On the diaphragm are positioned four strain gauges along the perimeter of the membrane, arranging a Wheatstone bridge. The only upper limit for detecting a phenomenon corresponds to the sensor resonance frequency, which is 200 kHz (over 18 times more than the DREAM BPF).

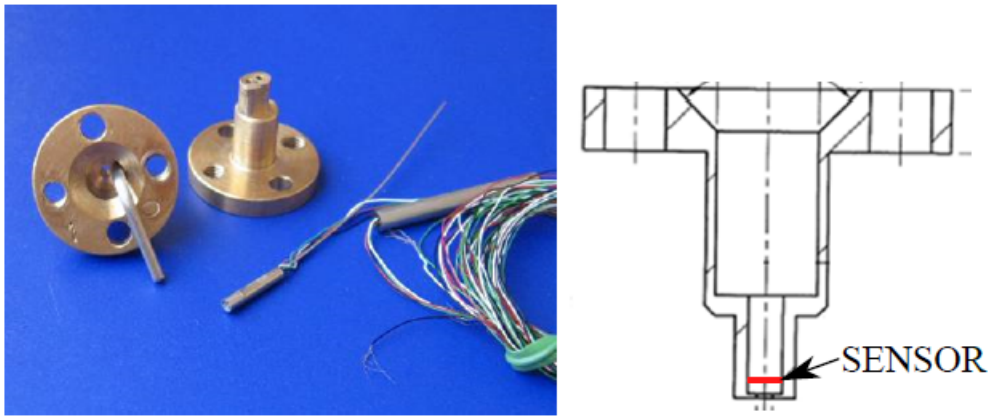

Figure 2.18: Fast-response casing sensors configuration[8]

2.3 Probe Placement and acquisitions

Rakes

Four rakes are strategically positioned at planes 0 and 4, corresponding to the inlet and outlet of the stage. Each rake is equipped with six Kiel heads, and their distribution is non-linear, designed to concentrate all the heads within the same area, as illustrated in fig 2.19. At the inlet, the rakes are precisely situated at 90°, while at the outlet, they are positioned at 90° with a slight adjustment to ensure a representative average across the entire stator pitch.

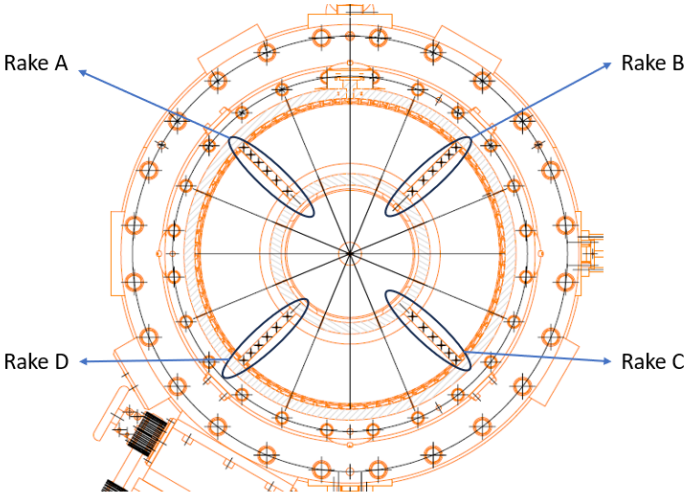

Figure 2.19: Rakes's head radial distribution

Pneumatic probe

The pneumatic probe was positioned downstream of the stator, specifically on Plane 4. As previously indicated, the probe's traversing was conducted in virtual mode. The figure illustrates the radial positions at which the measurements were acquired.

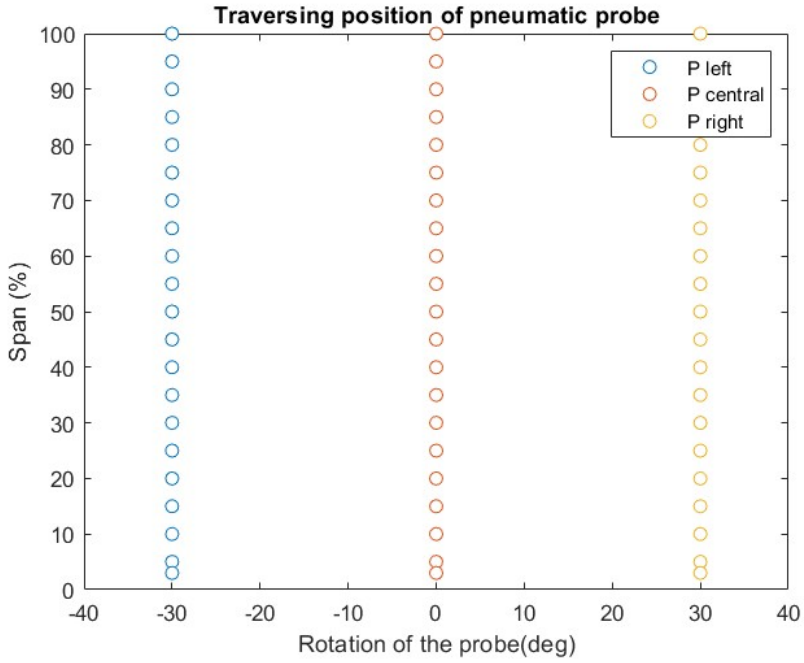

Figure 2.20: Traversing of the pneumatic probe

The figure displays data from 21 spanwise positions, differing by 5% span, starting from 100% span. In each spanwise position, the probe was rotated to simulate the left, central, and right holes.

Fast response pressure probe

The fast response pressure probe was situated in Plane 3. The acquisition procedure employed for this probe mirrors the one used for the pneumatic probe.
The probe operated at a sampling rate of 500 kHz with a one-second pre-trigger configuration. This allowed the probe to continuously acquire data, and upon receiving a trigger signal from the computer, it recorded all acquired data points in a MATLAB file from one second before the trigger. As the acquisition was set to one second a total of 500,000 data points were obtained for Pleft, Pcentral, and Prigh.

Casing fast-response pressure sensors

The casing sensors are positioned axially along the rotor, with their axial distribution displayed in Figure 2.23 and their circumferential distribution shown in fig. 2.21. The

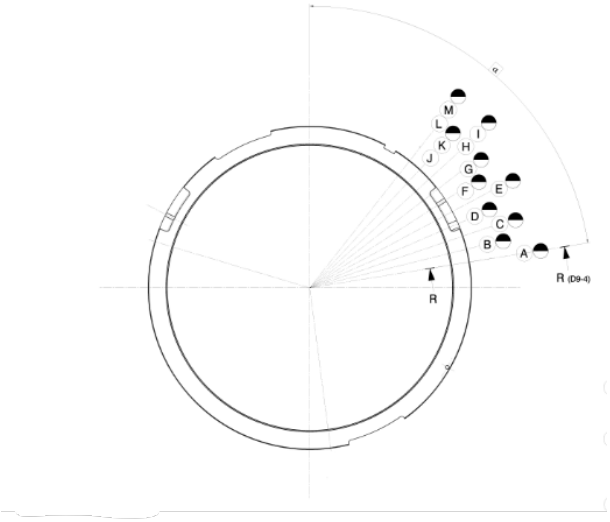

Figure 2.21: Kulite angular position

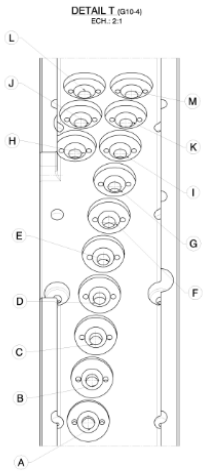

Figure 2.22: Kulites and axial position

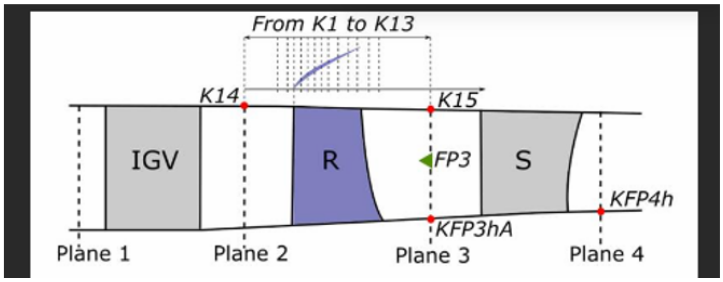

Figure 2.23: Kulites axial position

Kulite sensors were configured with identical fast response settings for both pre and post-trigger intervals, operating at a 500 kHz sampling frequency. It's essential to note that, as previously mentioned, not all Kulite sensors were functional. Specifically, as shown in fig. 2.23, only sensors k1, k3, k5, k6, k7, k8, k9, k14, and k15 were operational.
These sensors span a 42° arc, with K3 and K4 at the extremes, located at 80° and 38°, respectively, and are evenly spaced by one rotor pitch. The sensors are axially positioned between plane 2 and plane 3, as indicated in fig. 2.23. K14 is situated in plane 2, while K15 is in plane 3.

3

Performance and steady-state acquisition

In turbomachinery, a standardized form is adopted for the purpose of comparing different compressors and ensuring that performance evaluations are independent of test conditions. Through dimensional analysis, the performance depends on four non-dimensional parameters[18] [19]:

- Reynolds Number
- Mach number
- Heat capacity ratio
- Ratio between the peripheral velocity and the speed of sound

It can be demonstrated that if two geometrically similar compressors share these four parameters, they will yield identical pressure ratios and efficiency. This principle elucidates why tests are conducted on a scaled model of the actual compressor. The results can then be extrapolated to determine the performance of the real compressor, even if there are differences in dimensions or ambient conditions, as long as the principle of similarity is maintained.
The heat capacity ratio depends only on the nature of the fluid. Thus, if two machines operate in the same way, it could be assumed as a constant.
Reynolds number instead is more significant, but for similar dimensions, operating points and boundary conditions, it leads to slight differences in the compressor characterization. However, the compressor can be tested at different Reynolds conditions to correct the eventual Reynold effects.
Other variables are the Mach number and the ratio between the peripheral velocity and the speed of sound. For determining the ratio between the peripheral velocity at the tip of the blades and the speed of sound, it is often difficult to measure the temperature at

the tip of the blades, which is necessary to determine the speed of sound at this location. This explains why the inlet total temperature, T_0^0, is often used instead.
The loading coefficient Ψ and the flow coefficient ϕ can be expressed in the function of Mach number and the ratio between the peripheral velocity and the speed of sound[19]:

$$\Psi = \frac{\Delta h^0}{U_{tip}^2} = \frac{c_p \Delta T^0}{c_p T_0^0} \cdot \frac{c_p T_0^0}{U_{tip}^2} = f\left(\frac{\dot{m}\sqrt{c_p T_0^0}}{D^2 P_0^0}, \frac{ND}{\sqrt{\gamma R T_0^0}}\right) \tag{3.1}$$

$$\phi = \frac{c_{ax}}{U_{tip}} = \frac{\dot{m} R T_0^0}{P_0^0 A_0 U_{tip}} = f\left(\frac{\dot{m}\sqrt{c_p T_0^0}}{D^2 P_0^0}, \frac{ND}{\sqrt{\gamma R T_0^0}}\right) \tag{3.2}$$

The second parameter is closely related to the ratio between peripheral velocity and the speed of sound. However, it differs in that it incorporates the dynamic component of the total inlet temperature instead of relying on the static temperature for calculating the speed of sound. This choice is primarily driven by the ease of calculating total temperature, particularly in the blade's tip region. Assuming a constant passage section at the inlet and a constant value of γ and R:

$$\frac{ND}{\sqrt{\gamma R T_0^0}} \propto \frac{N}{\sqrt{T_0^0}} = N_{corr} \tag{3.3}$$

Where N is the mechanical rotational speed.
The first variable on the other hand is intrinsically Mach number-dependent. Indeed, when breaking down the mass flow into:

$$\dot{m} = \rho A U = \frac{\rho}{\rho_0} A \cdot M \frac{a}{a_0} \rho^0 a^0 = \frac{\rho}{\rho_0} A M \sqrt{\frac{T}{T^0} \rho^0 a^0} \tag{3.4}$$

Assuming a constant inlet passage section and treating the flow as adiabatic (without heat exchanges) and isentropic (without shock waves), the isentropic relations between temperature (T and T^0) and density (ρ and ρ^0) can be applied:

$$\frac{\dot{m}\sqrt{c_p T_0^0}}{D^2 P_0^0} = \sqrt{\frac{\gamma}{R}} M (1 + \frac{\gamma - 1}{2} M^2)^{\frac{\gamma+1}{2(\gamma-1)}} \propto \frac{\dot{m}\sqrt{T^0}}{P^0} = WR \tag{3.5}$$

This parameter is called corrected mass flow (WR) and as it is visible from eq.3.5 is a function of the Mach number and the heat capacity ratio γ.
To recap the two equivalent quantities which have just been defined are:

- Corrected rotational speed $N_{corr} = \frac{N}{\sqrt{T_0^0}}$ $[\frac{rpm}{\sqrt{K}}]$
- Corrected mass flow $WR = \frac{q_m \sqrt{T^0}}{P^0}$ $[\frac{Kg \cdot \sqrt{K}}{s \cdot Pa}]$

These parameters are expressed in units that may not have direct physical significance. To establish units that align more closely with physical reality, standard conditions are

employed, and corrected rotational speed and mass flow are defined as:

$$N_{corr} = \frac{N}{\sqrt{\frac{T_0^0}{T_{std}}}} \ [rpm] \tag{3.6}$$

$$WR = \frac{q_m \sqrt{\frac{T_0^0}{T_{std}}}}{\frac{P_0^0}{P_{std}}} \ [Kg/s] \tag{3.7}$$

Another important parameter is the Reynolds number which is computed using:

$$Re = \frac{\frac{P_{t0M}}{\left(1+\frac{\gamma-1}{2}Ma_{CFD}^2\right)} C\,W}{\mu_{ref}} \tag{3.8}$$

Where C is the rotor blade chord and W is the relative velocity at the tip of the blade.
Employing these variables, the experimental characterization of the booster can be conducted. This involves the acquisition of compressor maps and the determination of compression ratio and efficiency as functions of the corrected parameters. This approach serves to minimize the impact of inlet boundary conditions.

3.1 Performance maps

3.1.1 Operative procedures

Before starting the compressor, a mandatory preliminary check of the sensor output is conducted to ensure their proper operation. Once the control checks are completed, the initial step of the test involves accelerating the motor with the throttle valve. During the acceleration phase, close attention is directed towards critical parameters, which include:

- Monitoring water temperature inside the heat exchanger
- Supervising the compressor shaft's acceleration
- Continuously tracking temperature and pressure profiles at the compressor's inlet and outlet

The LabVIEW® user interface displays and records all of these parameters, acquiring and calculating derived values in real time. The acceleration rate is controlled manually at a rate of approximately 25-50 rpm/s. Once the nominal corrected speed is achieved, the acceleration phase concludes.
Holding the same corrected speed and throttling down the compressor, the corrected mass flow decreases while the compression ratio increases, following the characteristic curve of the compressor. Once the characteristic curve arrives near the stall, the throttle valve control is switched from automatic to manual. When the stall occurs, it leads to drastic performance reduction. The fast-opening security valve is activated to re-stabilize

the machine from the stall to the stable regime. By keeping the corrected speed constant and the valve fully open, the compressor operation returns to its choke condition, the iso-speed cycle ends, so that another speed can be selected.
The next target corrected speeds are reached, gradually decelerating the DC motor and keeping the valve completely open. A new iso-speed cycle starts when the corrected speed and the other parameters are stabilized. When the last iso-speed cycle is taken, once the compressor is stabilized at the latest choke point, its rotational speed is gradually reduced to zero, and the test is over.

3.1.2 Parameters acquisition routine

It is feasible to ascertain the stage's performance in terms of the total-to-total pressure ratio and efficiency as a function of corrected mass flow. This assessment relies on data gathered from static pressure, total pressure, and total temperature measurements obtained from the pressure taps and the rakes positioned in Plane 0 and Plane 4. The pressure taps are situated according to the configuration detailed in Section 2.2.3, both at the hub and on the casing aligning with the circumferential position of the rakes. To obtain static pressure values at the same six radial locations as the rake heads, linear interpolation is employed between the static pressure at the hub and the static pressure at the tip. Exploiting these measurements, it is then possible to determine all the variables of interest in Plane 0 and Plane 4 at the six radial measurement positions:

$$\frac{P^0}{P_s}(r_i) = \left(1 + \frac{\gamma - 1}{2} Ma(r_i)^2\right)^{\frac{\gamma}{\gamma-1}} \tag{3.9}$$

Where r_i is the radial position. As P^0 is the total pressure obtained from the rakes and P_s the static pressure obtained by interpolating the pressure taps, it is now possible to evaluate the Mach number in each radial and circumferential position:

$$Ma(r_i) = \sqrt{\left[\frac{P^0}{P_s}\left(r_i\right)^{\frac{\gamma}{\gamma-1}} - 1\right]\frac{2}{\gamma - 1}} \tag{3.10}$$

Once the Mach number is known, the static temperature can be determined thanks to the total temperature measured by the rakes :

$$T_s(r_i) = T^0(r_i)\left(1 + \frac{\gamma - 1}{2} Ma(r_i)^2\right)^{-1} \tag{3.11}$$

This allows the determination of the air speed and then the absolute velocity of the flow

$$a(r_i) = \sqrt{\gamma R T_s\left(r_i\right)} \qquad U\left(r_i\right) = a\left(r_i\right) \cdot Ma \tag{3.12}$$

The density of the fluid can be determined using the ideal gas law:

$$\rho(r_i) = \frac{P_s(r_i)}{RT_s(r_i)} \tag{3.13}$$

Considering that the 6 Kiel probes for each rake are strategically positioned to cover portions of equivalent area, so that A_1=A_2.....=A_6. This arrangement allows for the calculation of mass flow at each position:

$$q_m(r_i) = \rho(r_i)V(r_i)A \tag{3.14}$$

Then the total mass flow for the stage is obtained by computing the mean of the results obtained for each rake.
A recap of the five key parameters for performance maps is presented:

- $WR = \frac{q_m\sqrt{\frac{T_0^0}{T_{std}}}}{\frac{P_0^0}{P_{std}}}$ $[Kg/s]$
- $N_{corr} = \frac{N}{\sqrt{\frac{T_0^0}{T_{std}}}}$ $[rpm]$
- $Re = \frac{\frac{P_{t0M}}{\left(1+\frac{\gamma-1}{2}Ma^2_{CFD}\right)}CW}{\mu_{ref}}$
- $\beta_{tot} = \frac{P_4^0}{P_0^0}$
- $\eta_{is} = \frac{\left(\frac{P_4^0}{P_0^0}\right)^{\frac{\gamma-1}{\gamma}}-1}{\frac{T_4^0}{T_0^0}-1}$

3.1.3 Results

The average performance map of the Dream compressor stage, obtained from rake measurements, is presented in fig 3.1,3.2 and 3.3. These figures illustrate the relationship between total-to-total pressure ratio, efficiency, and total temperature ratio with corrected mass flow. Each case includes standard deviation values to provide insights into the variability of these performance metrics during operation.
The ref value depicted in the graphs corresponds to the conditions at 100% of the nominal speed in design conditions. To comprehend the transition from the raw signal to the averaged maps, please consult Appendix B.
In terms of maximum efficiency, the corrected speeds of 90% and 96% Nn demonstrate a higher value compared to the 100% Nn corrected speed, contrary to initial expectations.
The map corresponding to 96 Nn does not exhibit the typical pre-stall behavior observed at 100 and 90 Nn. This is because the compressor at 96 Nn has not been pushed to stall conditions.
The standard deviation consistently begins with a higher value at the design point and decreases to a lower value as it approaches near-stall conditions. For instance, at 100 Nn, the pressure ratio standard deviation is approximately 0.6% at design and decreases to around 0.2% at near stall.

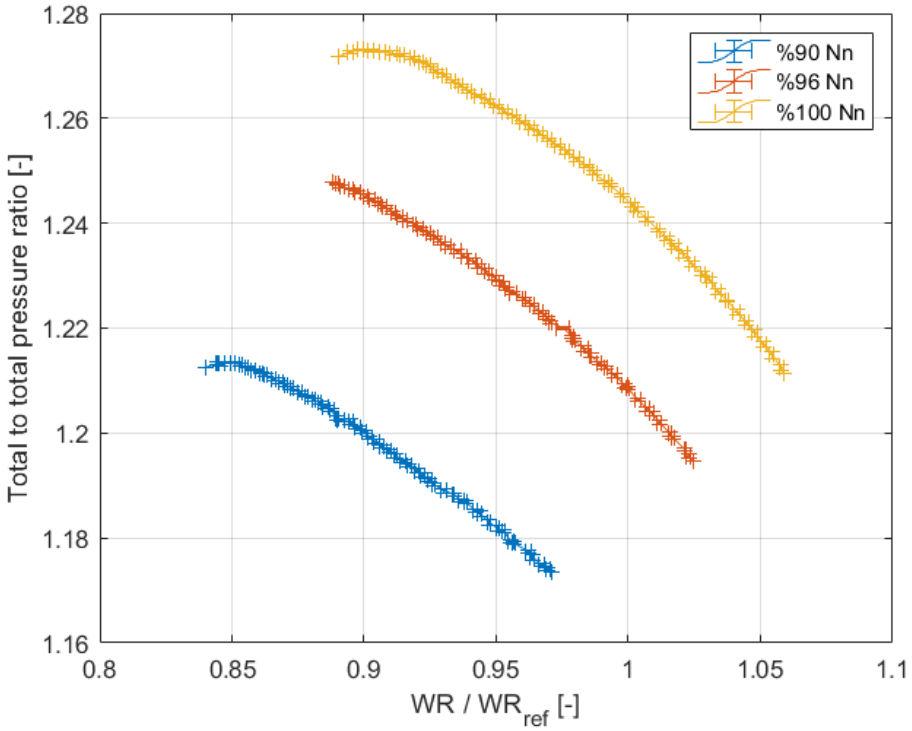

Figure 3.1: Stage total to total Pressure ratio performance map with standard deviation

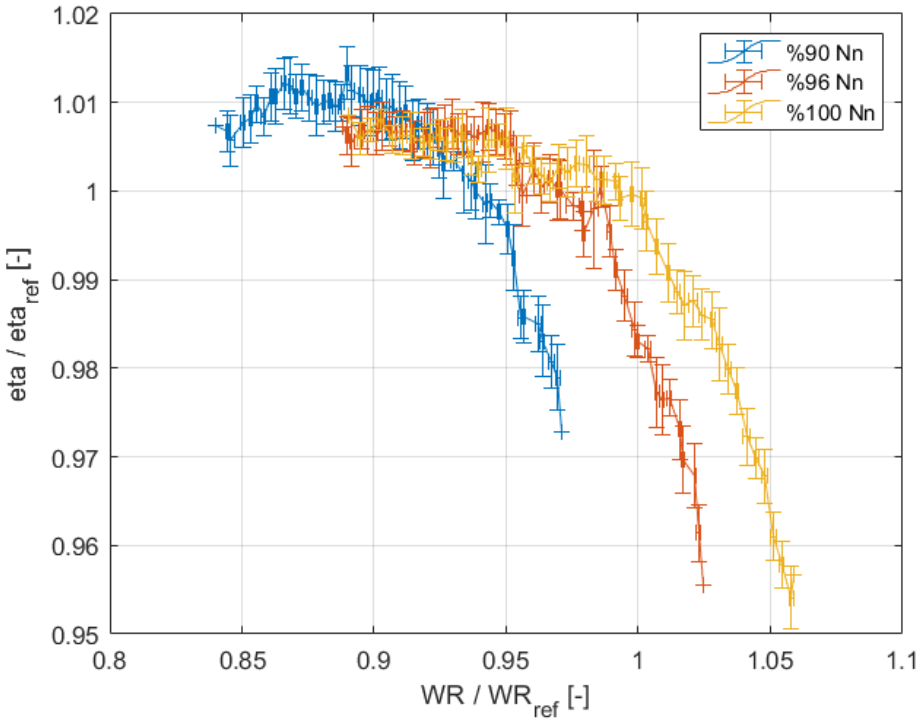

Figure 3.2: Stage efficiency performance map with standard deviation

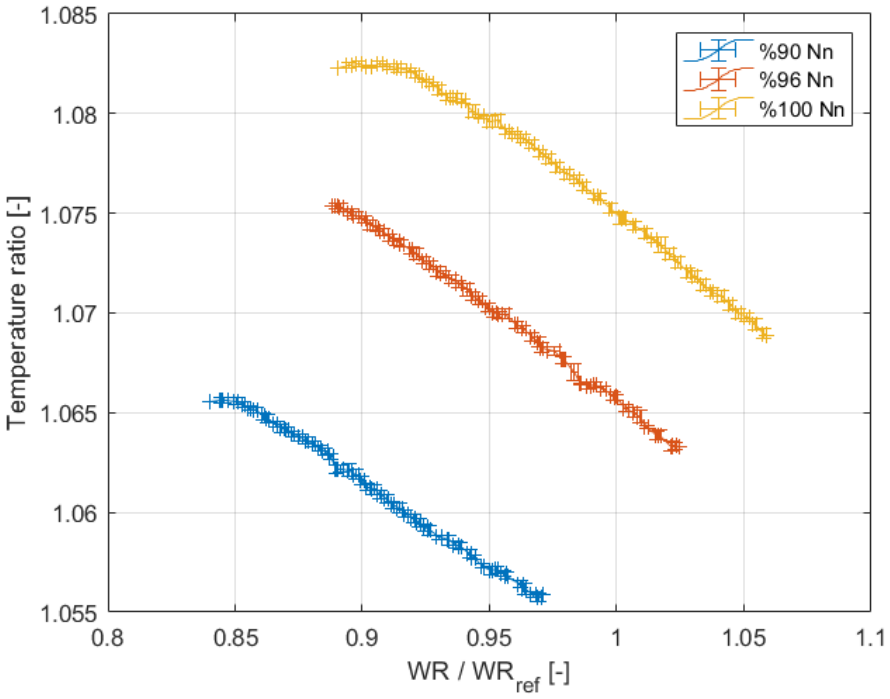

Figure 3.3: Stage total to total temperature ratio performance map with standard deviation

As detailed in section 1.4, the acquisition of performance maps involved stator traversing in conditions ranging from the design to near-stall. The stator, controlled electronically, was capable of rotating up to 2 stator pitch angles. The results of this maneuver are illustrated in fig.3.4 and 3.5. These figures highlight the importance of stator blade positioning in the evaluation of performance, specifically in terms of total pressure ratio and efficiency.

The stator traversing at the design point results in a more pronounced shift in performance maps compared to traversing near stall, affecting both total pressure and efficiency maps. In fig. 3.5, at the design condition, the relative stator blade positioning introduces approximately a 4% variation in the efficiency compared to their values at a stator angle of 0°. This error is reduced to just over 2% when traversing at near stall.

Performance maps reported in fig.3.1 were processed without stator traversing to avoid a substantial rise in the standard deviation within the design and near-stall regions.

Section 2.1.1 discusses the presence of a highly sensitive test section on the opposite side of the loop, necessitating the prevention of excessive pressure build-up within that area. To address this, several adjustments were made, involving the control of bypass valves and the regulation of inlet total pressure. Regrettably, these adjustments led to a reduction in the precision of performance mapping at 100% Nn.

Subsequently, the tests were repeated with enhanced control of the aforementioned parameters.

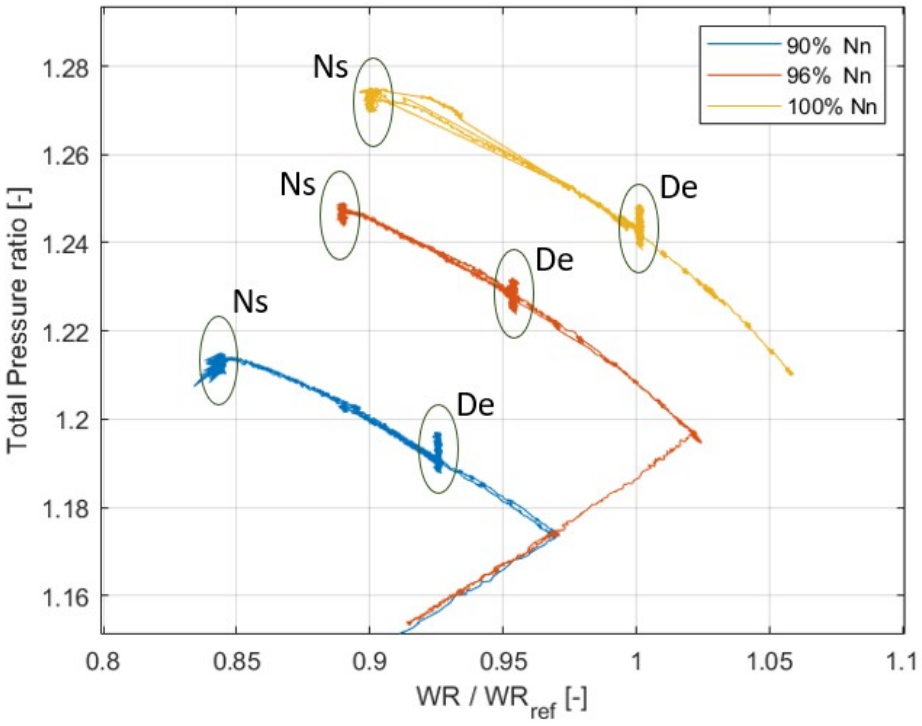

Figure 3.4: Performance map total to total pressure ratio with stator traversing

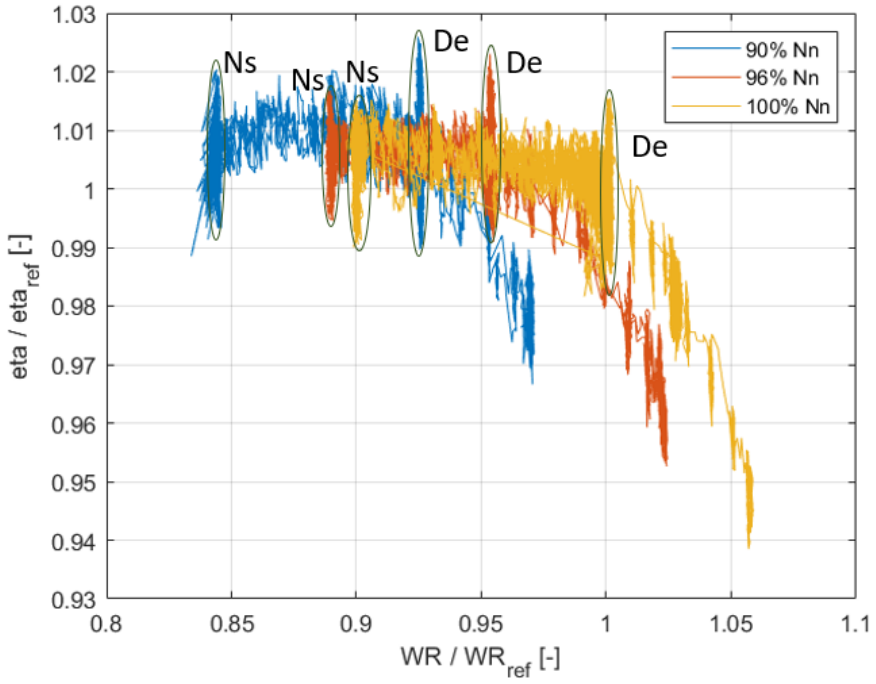

Figure 3.5: Performance map efficiency with stator traversing

The tests at 100 Nn were repeated, with particular attention given to maintaining constant inlet pressure and Reynolds number. Fig.3.8 highlights a significant Reynolds number variation during the first test. A comparison of the two tests reveals the influence of Reynolds number on the total pressure and efficiency.

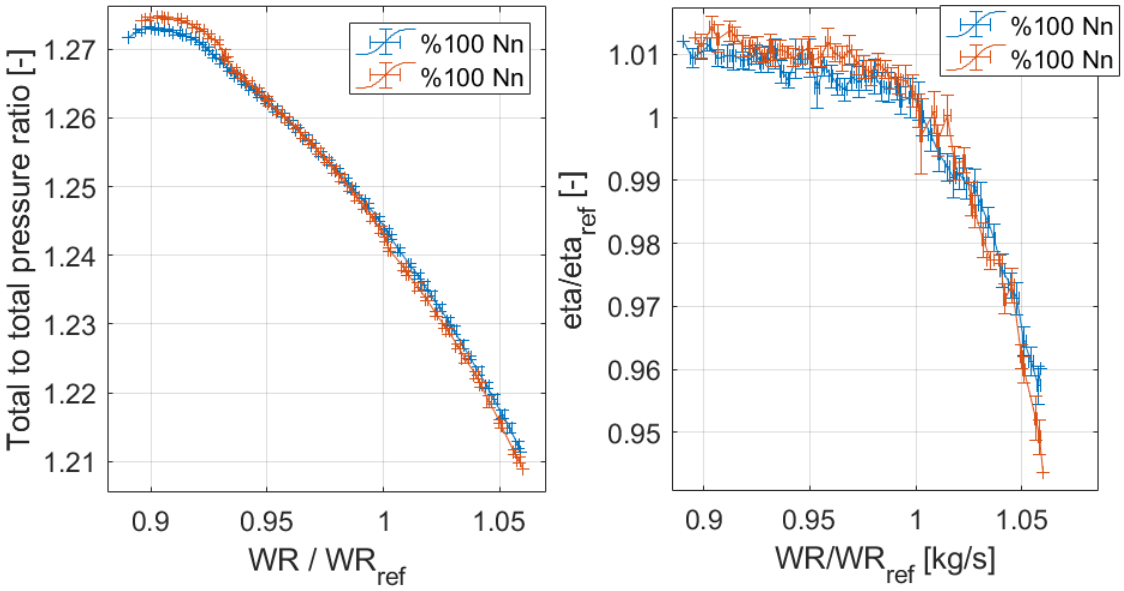

Figure 3.6: Reynolds impact on averaged performance map 100Nn

Left: Pressure ratio

Right: Efficiency

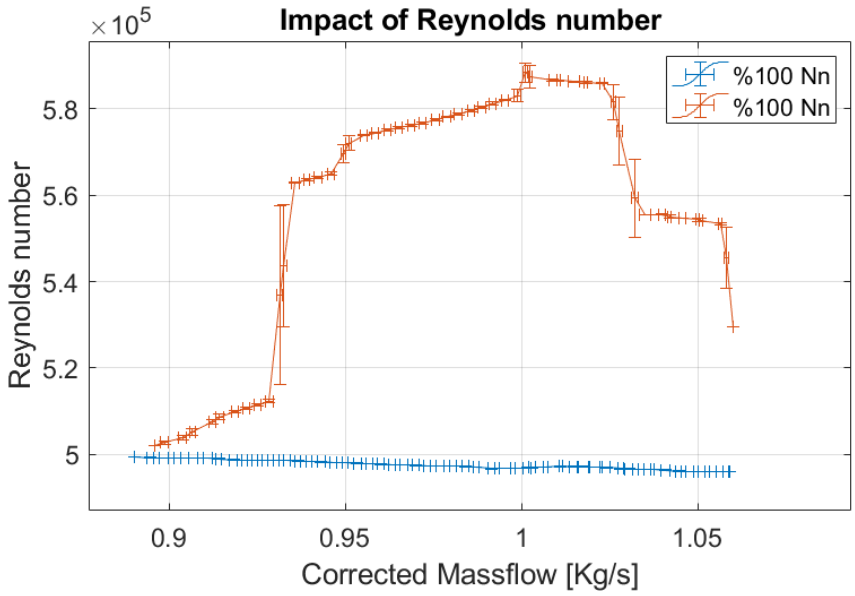

Figure 3.8: Reynolds variations

3.2 Span-wise distribution and maps at stator outlet using rakes

To comprehensively analyze the flow field at the stator exit, multiple shots were captured during experiments conducted at 100% Nn, both at the design and near-stall conditions.The procedure comprised 2 pitch steps with a 0.1 pitch increment, resulting in 21 shots, each corresponding to a different stator position. These shots were post-processed to extract insights into the stator exit flow field.
Only the figures for total pressure and total temperature will be displayed. This omission of Mach and flow rate is based on the fact that total pressure and total temperature provide nearly identical trends since they are computed from each other, as demonstrated in fig. 3.9. For a detailed flowchart outlining the process of calculating mass flow from the total pressure measured by the rakes, please refer to Appendix C.

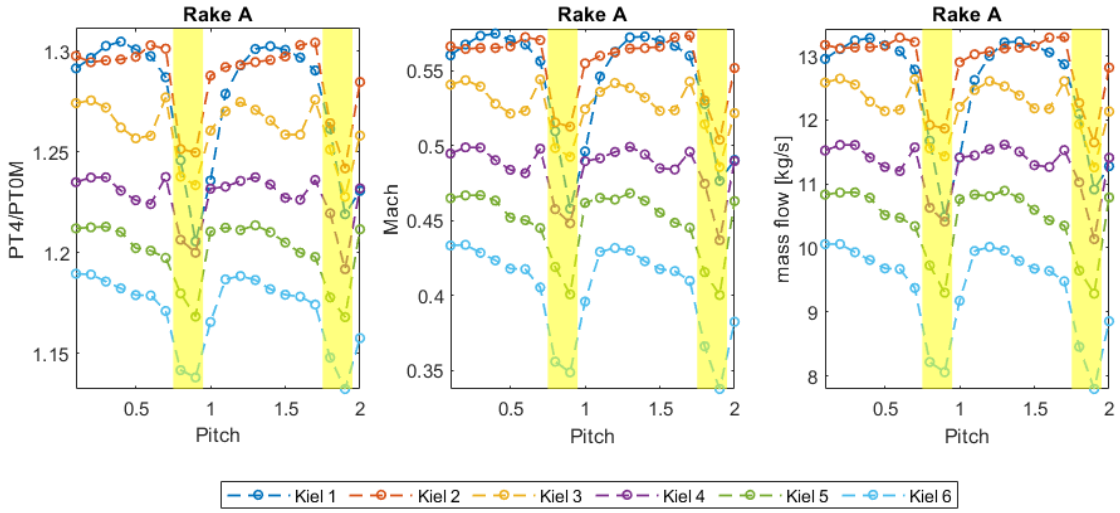

Figure 3.9: Comparison of mass flow trends, compression ratio, and Mach number

Fig.3.10 in the next page depicts the trends of the total pressure ratio and temperature difference for each Kiel probe on each individual rake.

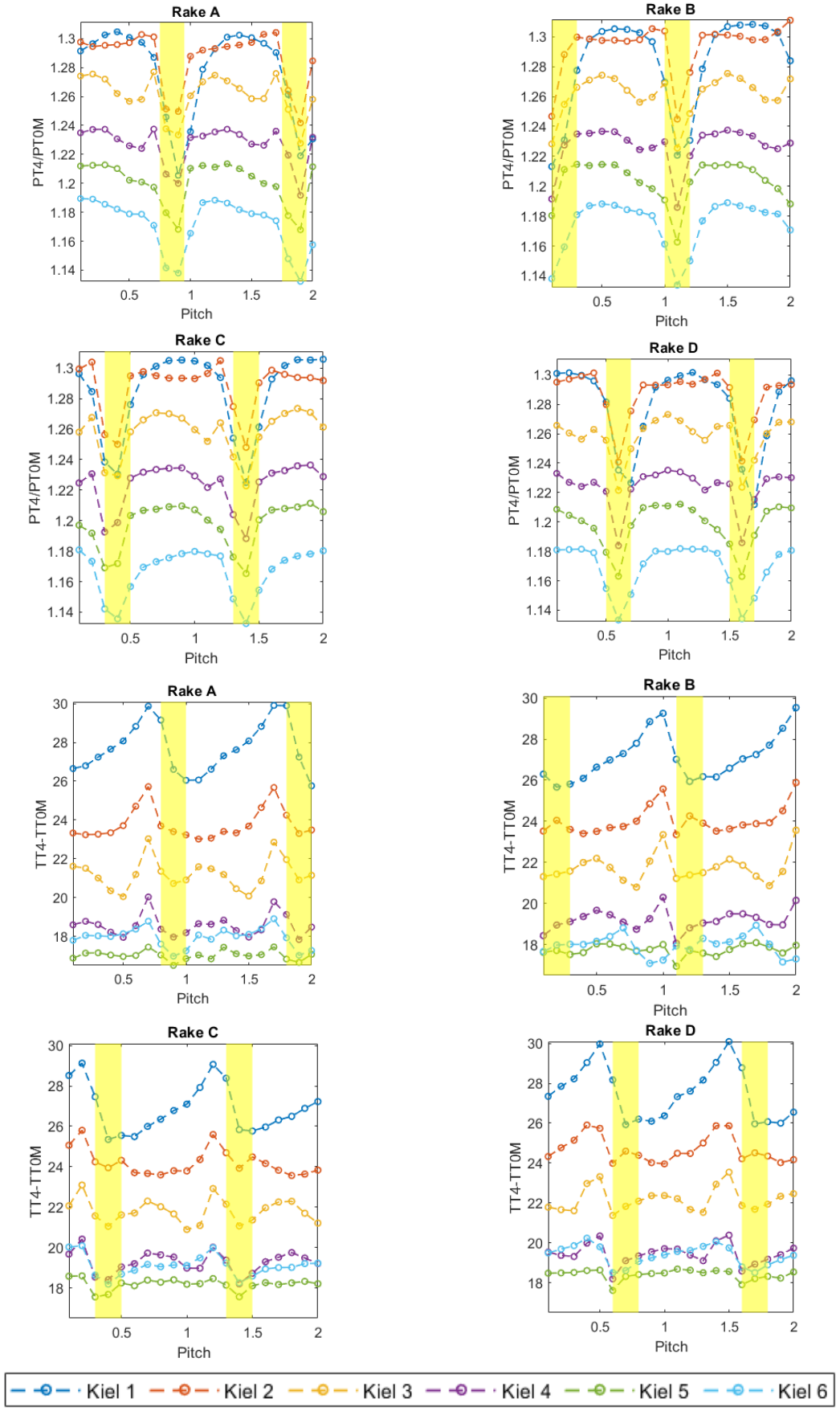

Figure 3.10: Total pressure ratio and total temperature difference for the 2 stator pitches at 100% Nn design

The wake of the stator is clearly visible in all the rakes and highlighted in yellow. As the stator is rotated in increments of 0.1 pitch, there comes a point when a stator blade aligns with the rake. This alignment results in an abrupt reduction in total pressure, Mach number, and mass flow. However, the effect of the stator wakes on total temperature differs noticeably with a more gradual increase in total temperature, in contrast to the total pressure ratio.
Each rake encounters the stator wake at a different pitch position. This is because the four rakes are strategically positioned to cover various stator pitch positions.

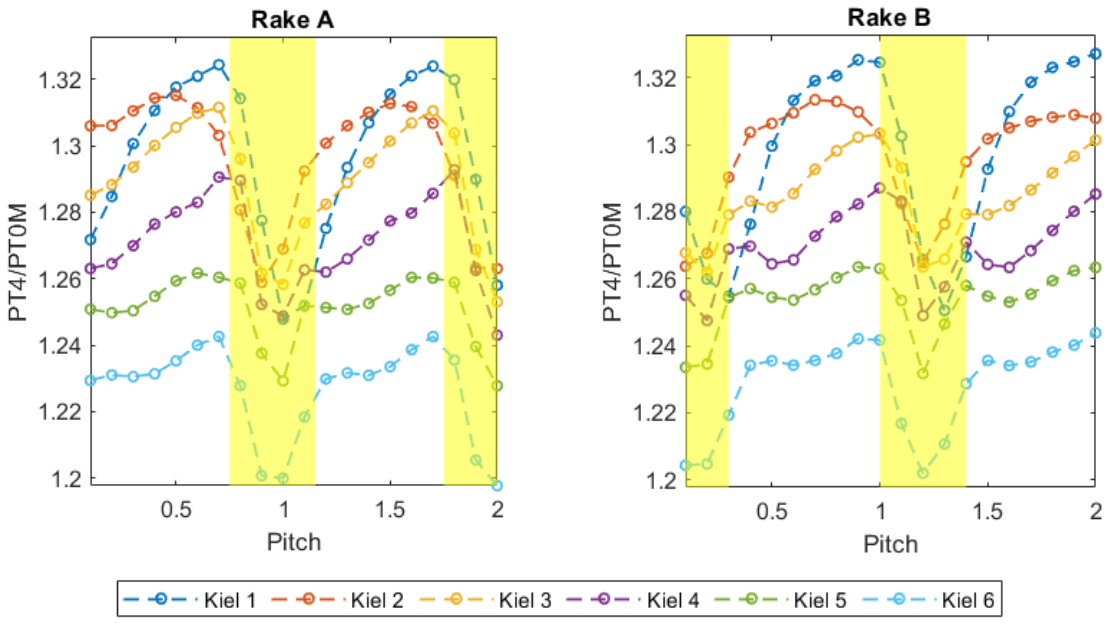

Figure 3.11: Total pressure ratio and total temperature difference 2 stator pitches at 100% Nn near stall

Looking at fig.3.11 the wake of the stator near stall is thicker than that at the design point. This is primarily due to the decrease in axial speed as the compressor approaches near stall conditions, leading to an augmented incidence angle and so to a thicker wake. Another noticeable observation in the design and near stall figures is that the wake associated with Kiel probe 1, corresponding to the hub, is thicker and results in a more significant reduction in total pressure compared to that observed at the tip. This phenomenon can be attributed to the hub-loaded nature of the Dream compressor, which leads to greater incidence at the hub and, consequently, a thicker and more intense wake.

In Fig. 3.12, the spanwise profiles of total pressure ratio and temperature difference are presented for various stator positions, spanning from S=0 to S=1. The data solely includes results from rake A, as other rakes exhibit consistent behavior, as evident from earlier figures. Average values for each rake are depicted in black (Avg), while the red value (AVG_{tot}) represents the overall average across all rakes.

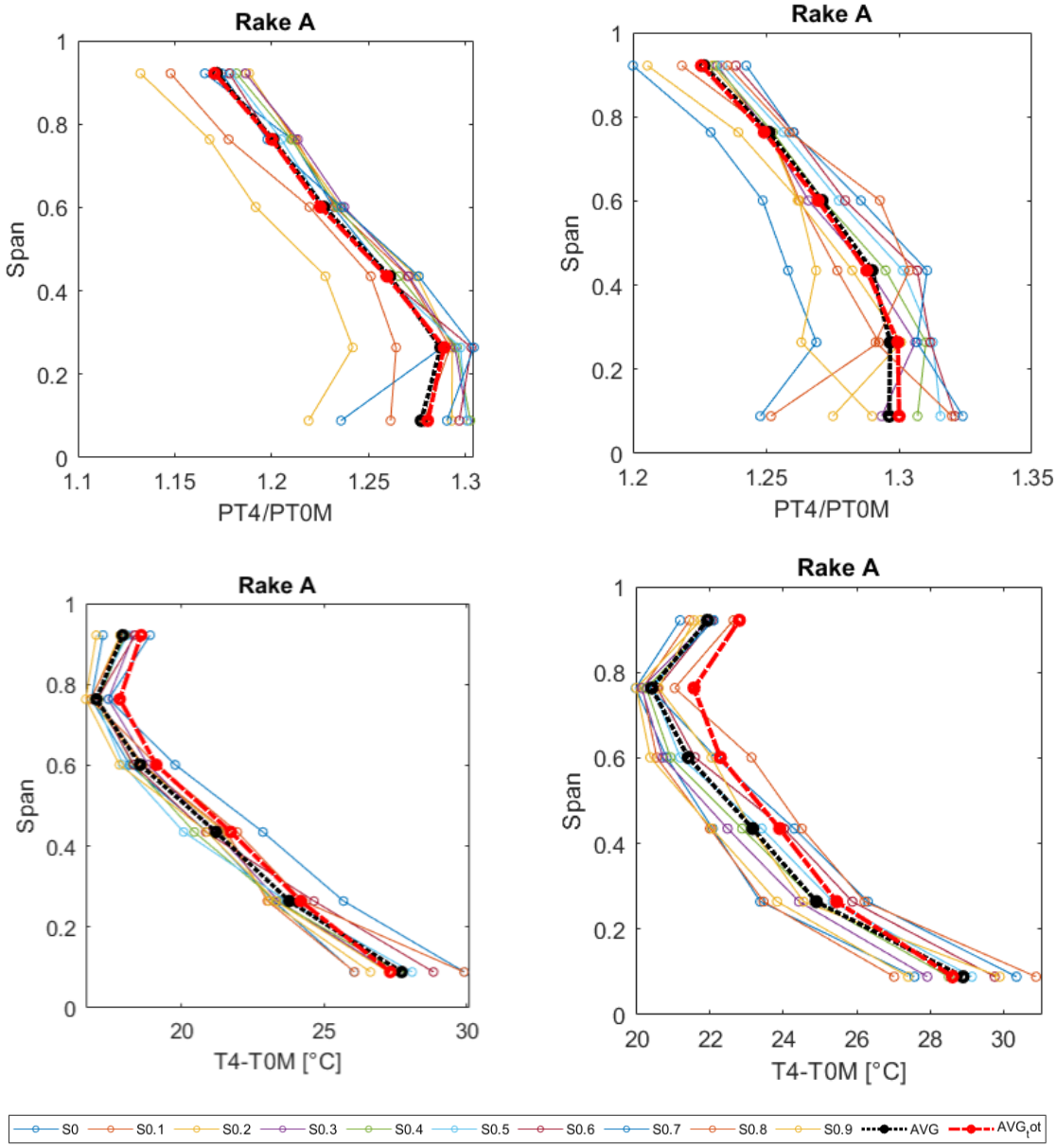

Figure 3.12: Span-wise distribution of total pressure ratio and total temperature difference for one pitch.

Left: Design Condition

Right: Near Stall Condition

The figures demonstrate that, for pressure ratio, the mean values of each rake align with the collective mean of all rakes. The mean temperature difference rake A exhibits a 2° difference in the tip region compared to the overall average. In conclusion, for an initial assessment of average fluid behavior in plane 4, a single rake's mean pressure ratio suffices, obviating the need to calculate the mean of the entire dataset.
Under design conditions, loading increases by 10% from tip to hub, reducing to around 5% reaching near stall.

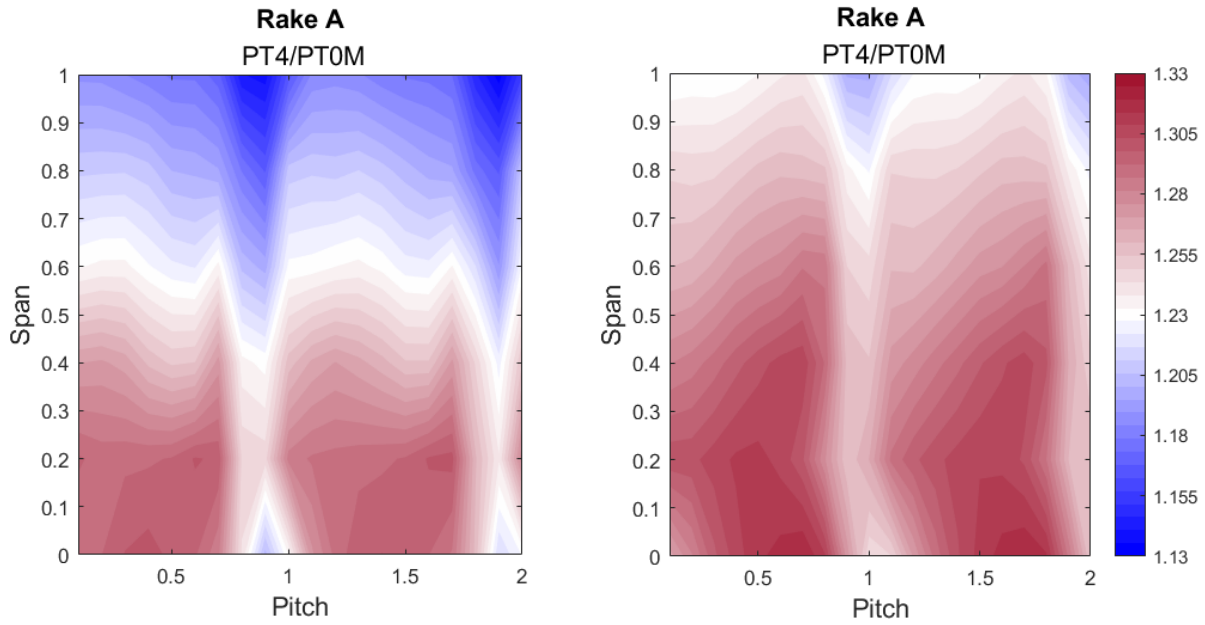

Figure 3.14: 3D map of Pressure ratio at 100%.

Left: Design Condition

Right: Near Stall Condition

Fig.3.14 displays the 3D pressure ratio map obtained through stator traversing at both design and near stall conditions in position 'A'.

During the transition from design to near-stall conditions, the pressure ratio increases, while axial velocity decreases due to reduced flow rate. This reduction in axial velocity results in higher incidence and loading, leading to the presence of a thicker wake. These figures also reveal the presence of stator hub corner separation. The phenomenon is clearly evident in the near stall conditions, where a pronounced thickening in the wake is observed. This thickening aligns with the suction side, consistent with the hub corner separation theory.

An additional analysis was conducted on Plane 4 using data acquired through rake instrumentation. Specifically, for each span position, a subtraction of the mean value was performed to highlight potential singular regions. This process generated the graphs presented in fig.3.21.

A region of losses becomes apparent, interacting with the stator wake. This phenomenon is less evident at design conditions but becomes pronounced under near-stall conditions, where a zone of low total pressure interacts with the stator wake. The existence of this low-pressure area can be attributed to the propagation of the Inlet Guide Vane (IGV) wake at the stator outlet.

Therefore, this low pressure zone can alter the incidence at the stator inlet, with a consequent impact on the generation of possible separations on the stator blade. Additional analysis of the wake interaction will be conducted in the following section using pneumatic probe on plane 4.

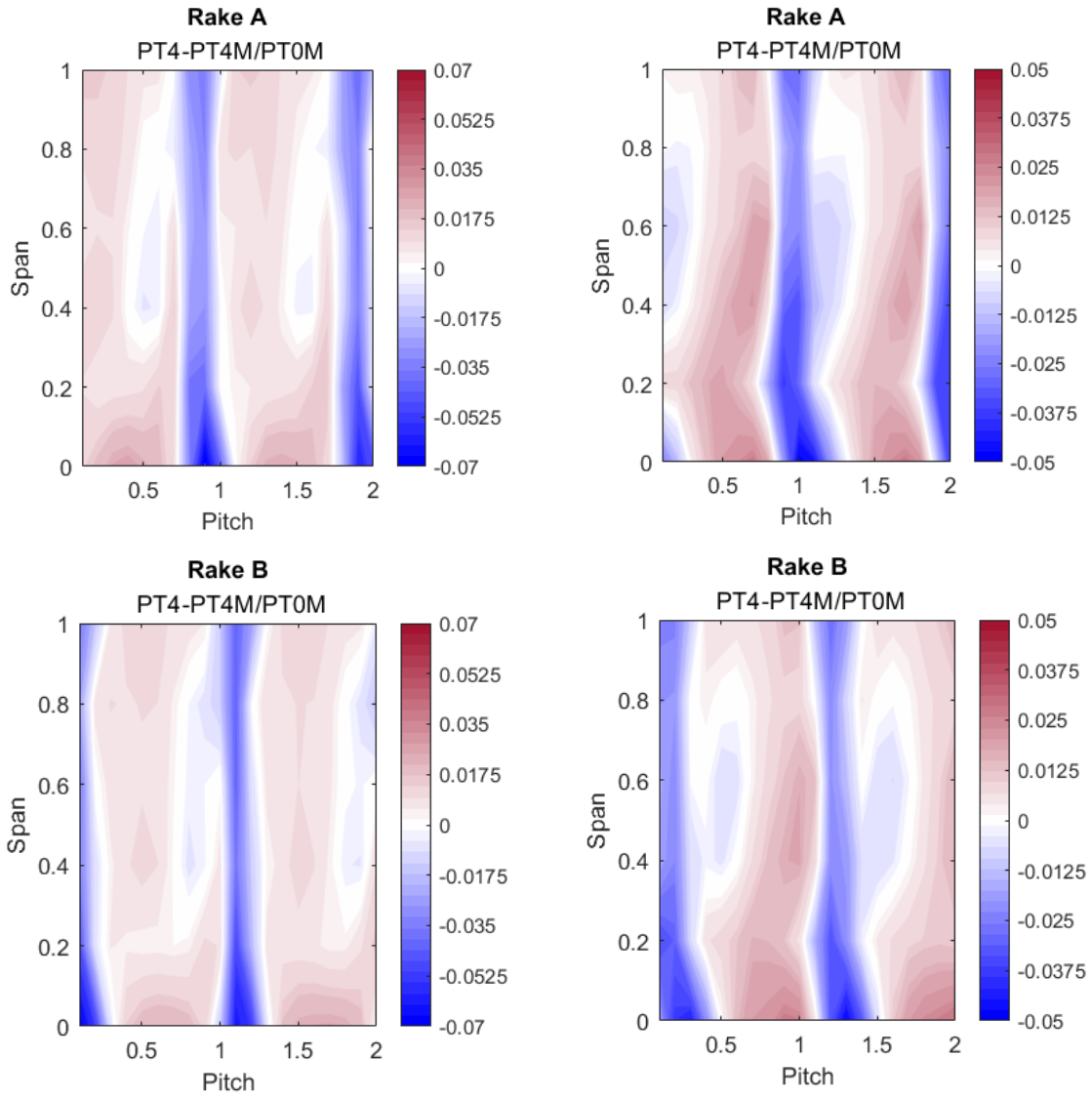

Figure 3.16: 3D Map of Pressure Ratio Related to P_{t0M} at 100% Nn:

Left: Design Condition

Right: Near Stall Condition

3.3 Span-wise distribution and performance maps at stator outlet using pneumatic probe

The traversing conducted with the pneumatic probe at Plane 4 was executed as outlined in section 2.2.4, employing a virtual approach and involving 21 spanwise positions. For each virtual measurement taken at each spanwise point, stator traversing was also performed. The traversing was first undertaken to acquire information regarding the exit angle of the flow, a parameter not attainable through the rakes. Secondly, the traversing

at 21 spanwise positions allowed for an improved spatial resolution and reconstruction of the flow field with respect to rakes.
The results, reported in fig.3.18, show the variation in total pressure and yaw angle as a function of span for 5 different pitch positions. The red line corresponds to a pitch rotation of 0.2, aligning the pneumatic probe with the stator wake. This alignment results in lower compression ratio values and lower angles.

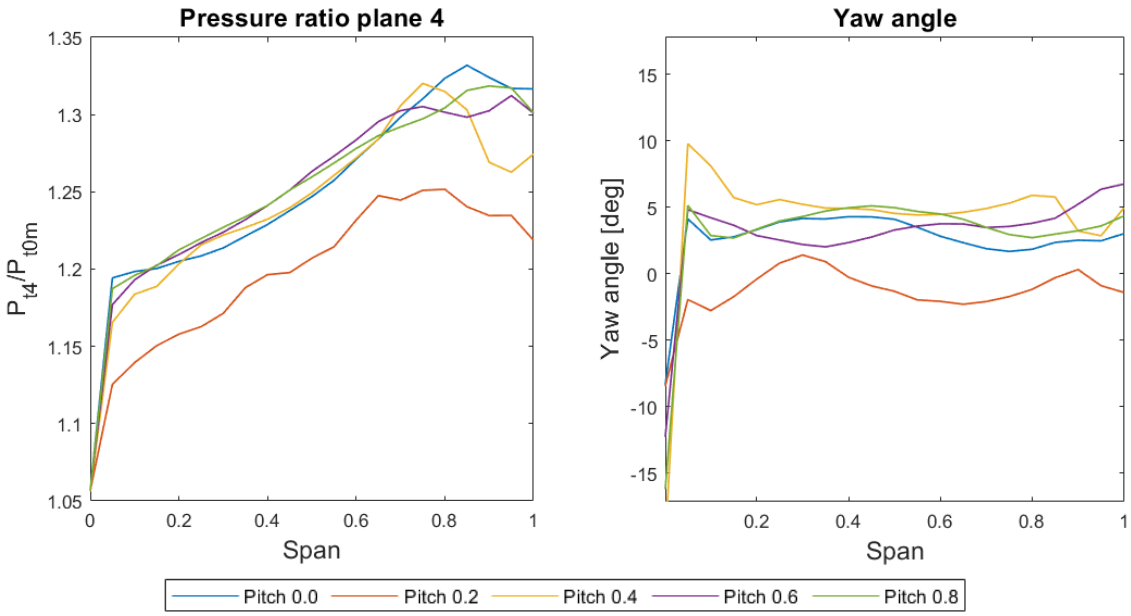

Figure 3.18: Pitch-wise distribution of Pt4/Pt0M and Yaw angle over span obtained with a pneumatic probe at 100Nn Design point

Fig.3.18 shows how the influence of stator traversing on performance and yaw angle assessment is evidently significant.
In fig.3.19 a 3D map highlites the total pressure ratio variation with respect to pitch and span for design and near stall conditions. These figures faithfully follow the trend previously anticipated using rakes, offering the significant advantage of enhanced detail. The stator hub corner separation is evident,resulting in a thickening of the wake on the suction side of the blade, with an increasing trend towards near-stall conditions.
The presence of tip leakage flow at the rotor tip is a well-established theoretical concept and it propagates downstream through the rotor, but the pneumatic probe's operating frequency is too low to capture this phenomenon. Nevertheless,the tip leakage flow generates a region of low axial velocity that propagates downstream. This region results in increased incidence and loading. Hence, in the tip region, a thicker wake is observed for this reason.

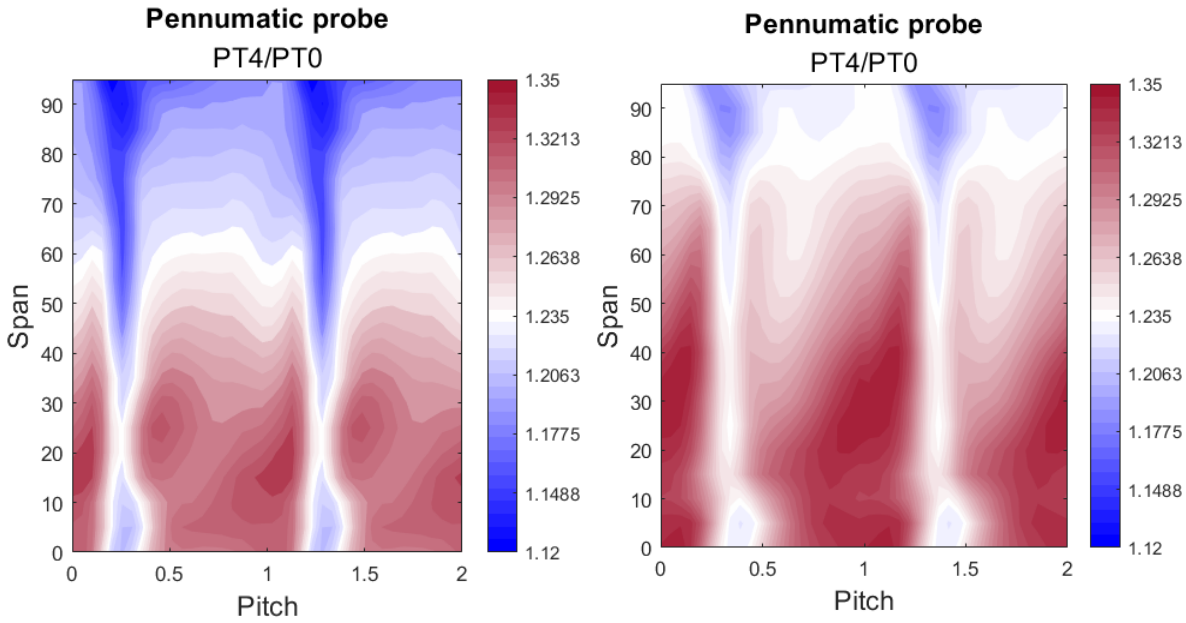

Figure 3.19: 3D map of Pressure ratio obtained with a pneumatic probe at 100Nn

Left: Design Condition

Right: Near Stall Condition

In fig.3.21 same procedure was applied as with the rakes, involving the subtraction of total pressure from the mean total pressure value for each span position. The resulting ratio with Pt0M confirms previous observations. Notably, a distinct area with lower pressure is evident, and this phenomenon is more pronounced at near stall. As already discussed this phenomenon is related to the IGV.

The acquisition with the 3 hole-virtual pneumatic probe generates also 3D maps for the yaw angle, as illustrated in fig 3.22. These maps show the impact of the IGV wake propagation at the stage outlet. Close to the stability limit of the machine, an incidence variation of 6° is expected at the stator inlet, with consequent impact on the generation of possible separations on the stator blade.
The stator wake become thinner within the span range of 60% to 80%, while a noticeable thickening occurs from 30% to 10% of the span, particularly at near stall conditions when the low-pressure area is more pronounced. A the stator inlet the flow encounters this low-pressure area, which creates a blockage effect, causing a redistribution of mass flow across different span positions. Consequently, an increase in flow rate within the span range of 60% to 80% leads to a rise in axial speed, reducing the loading and obtaining a thinner wake. In contrast, the span region between 10% and 30% experiences a notable reduction in flow rate, leading to an increased loading and a consequential alteration in flow angle at the stator outlet. This alteration causes a slight twisting of the wakes.

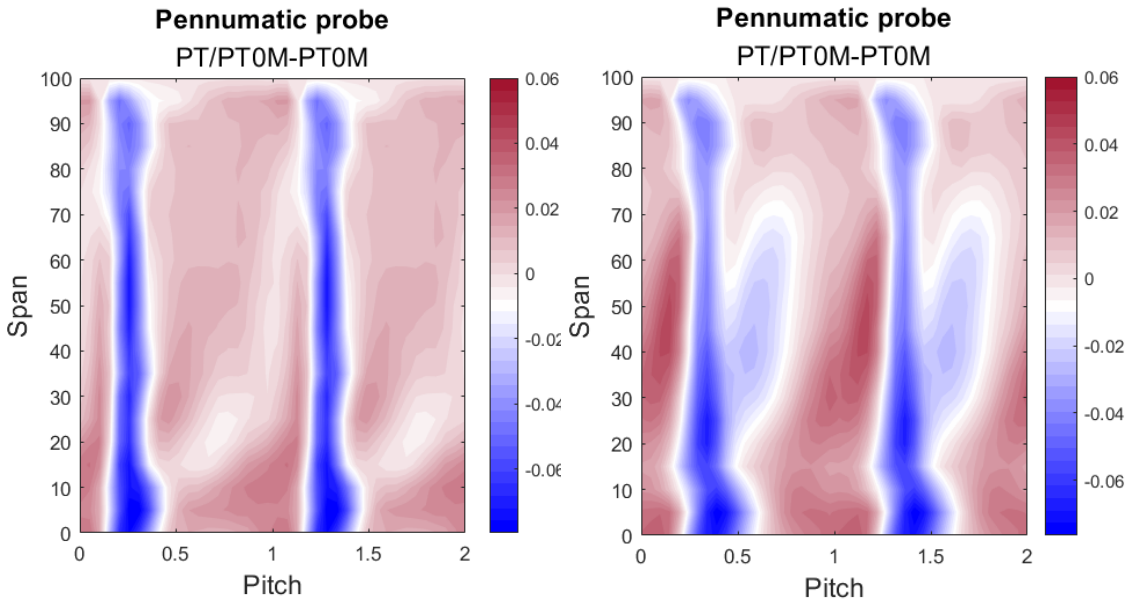

Figure 3.21: 3D map of Pressure ratio related to PT0M obtained with a pneumatic probe at 100 Nn

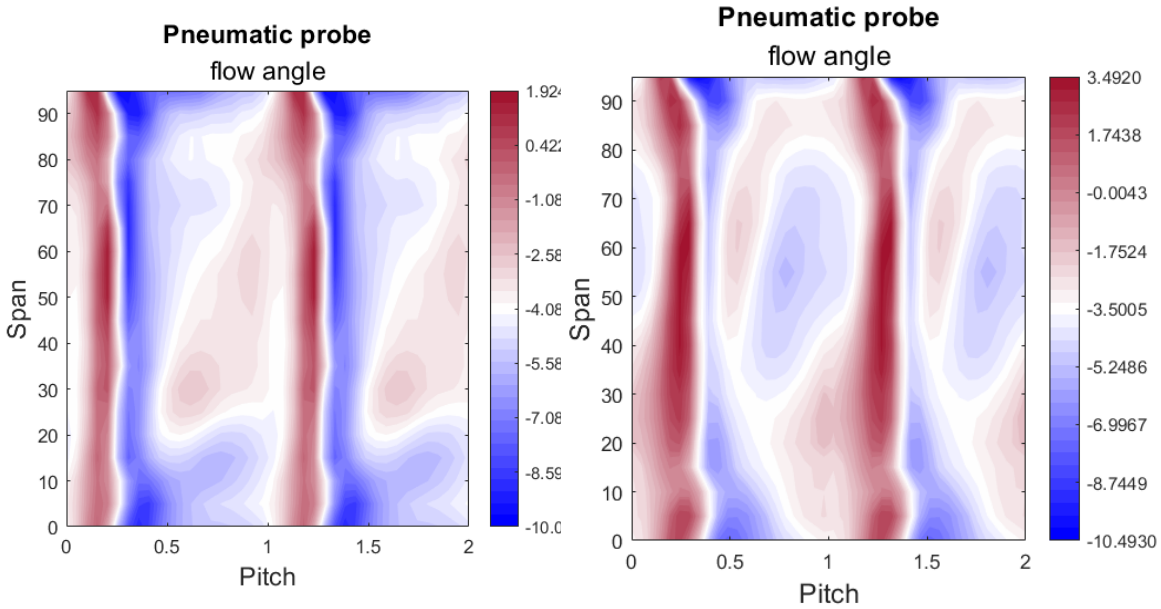

Figure 3.22: 3D map Yaw angle obtained with a pneumatic probe at 100Nn

Left: Design Condition

Right: Near Stall Condition

4

Detailed characterization of the flow-field at rotor exit

4.1 Fast response pressure probe

A complete unsteady flow characterization at the rotor outlet is performed. Total pressure, Mach and Yaw angle have been executed with a 3 hole-virtual fast response pressure probe. Measurements have been realized at 90% Nn, 96% Nn and 100% Nn at two operating points: design and near stall. This probe has been moved radially in order to have the total pressure distribution along the span, from 100% to 2.5% of the blade height. Traversing ended at the 2.5% span position to prevent any contact between the probe head and the hub, avoiding potential damage. The recorded signals have also been time averaged in order to have the mean pressure level along the span.
The Phase Lock Average (Explained in detail in Appendix D) was applied to the unsteady pressure signals, with the aim of assessing the averaged flow field in the relative frame of reference of the rotor. Subsequently, the total pressure and its fluctuations were non-dimensionalized with respect to the inlet total pressure.
The Phase Lock Average maps for total pressure, static pressure and yaw angle at 100% Nn conditions, are presented in fig.4.1, 4.3 and 4.5 for design and near stall conditions.
In the total pressure distribution, the wake is evident as a region of low pressure and unsteadiness, with higher values of RMS. Notably, the wake thickens as it approaches the hub. This phenomenon is attributed to the presence of hub corner separation, the theory of this aerodynamic feature is provided in section 1.5.2. Numerous examples in the literature highlight the growth of hub corner separation as loading increases, eventually leading to hub corner stall (Gbadebo, [cite]). In fig.4.1 a significant increase in hub corner separation is evident, extending from the design to near-stall conditions.

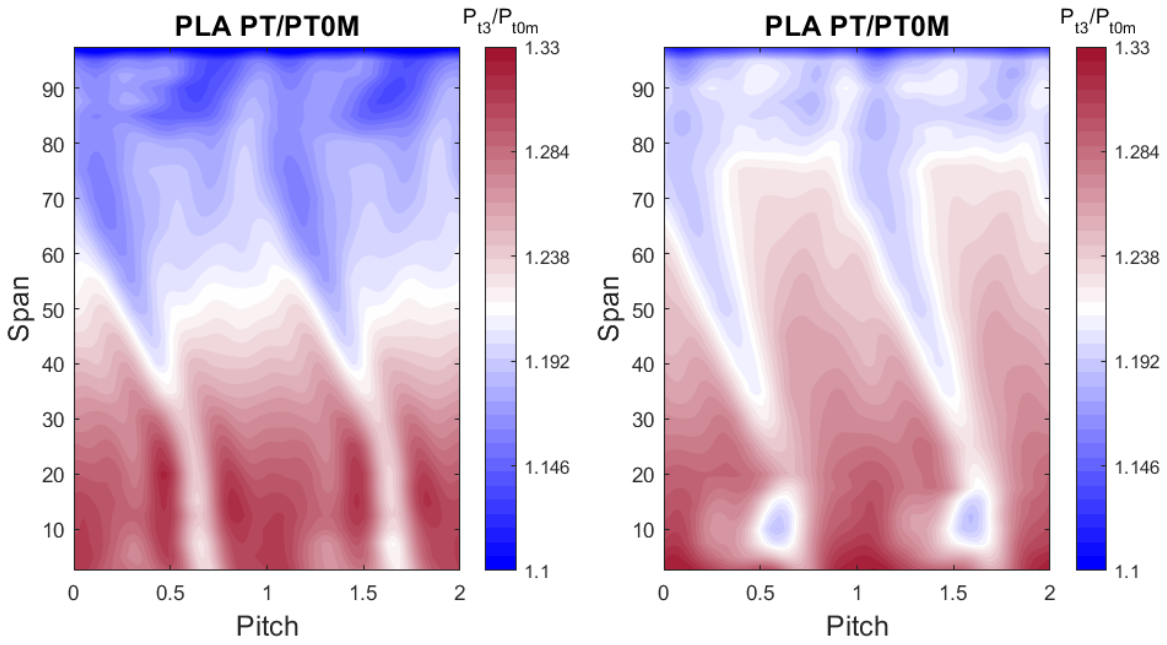

Figure 4.1: Total pressure phase locked average (PLA) map at 100% Nn

Left: Design Condition

Right: Near Stall Condition

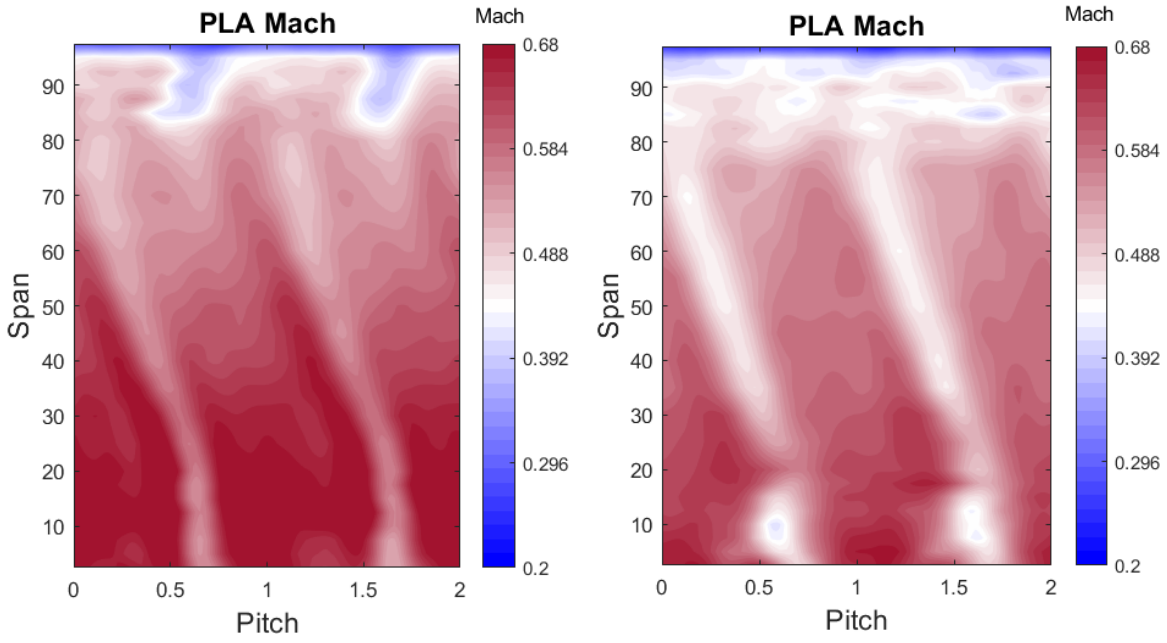

Figure 4.3: Mach phase locked average (PLA) map at 100% Nn

Left: Design Condition

Right: Near Stall Condition

In fig.4.3, the Mach number exhibits less distinct wake patterns compared to the total pressure, yet the presence of hub corner separation is consistently evident, especially at near stall conditions..
Regarding the flow angle map, a significant increase in the angle is observed both in the tip and hub regions as the stall point is approached. This increase is attributed to the thickening of instability vortices associated with hub corner separation and tip leakage.

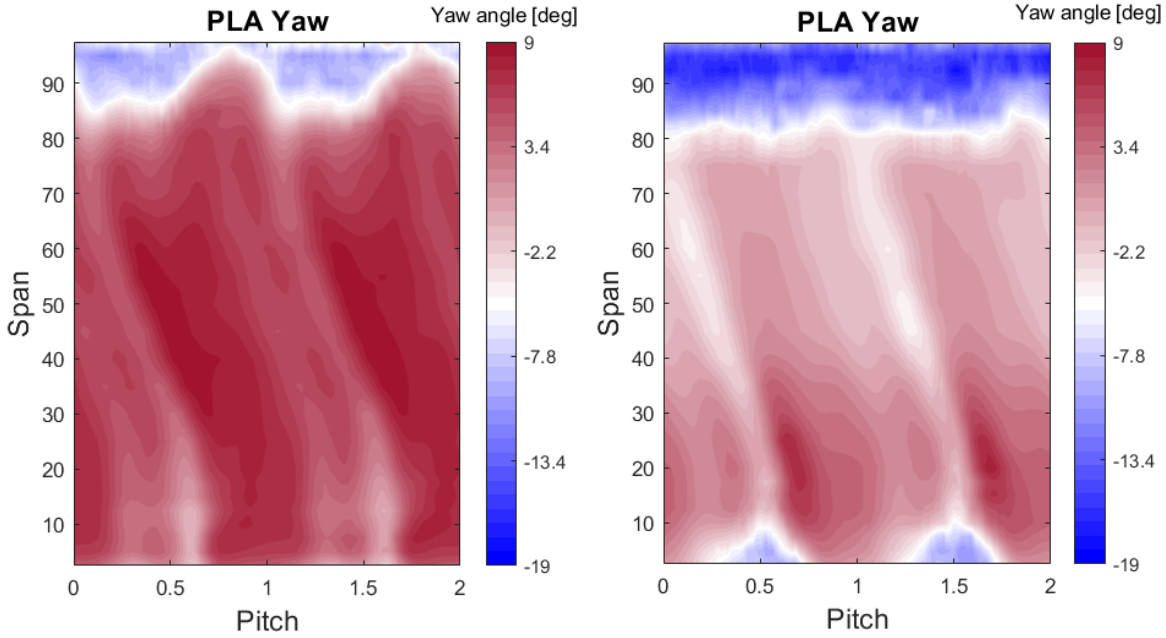

Figure 4.5: Yaw phase locked average (PLA) map at 100% Nn
Left: Design Condition
Right: Near Stall Condition

The combined analysis of the phase-locked average maps and RMS maps allows the description of the flow field and distinguishes the unsteady flow structures appearing in the blade passage. In Fig. 4.7 and 4.8, the total pressure maps obtained using the PLA technique are presented alongside the RMS fluctuation maps for both the design and near-stall configuration.

The same color scale has been consistently applied to all working conditions for the purpose of facilitating comparison. An observable transformation can be identified as the compressor moves from its design point to near-stall operating conditions. Specifically, the low-pressure region at the hub of the blades expands, and the turbulence fluctuations in this area intensify during the transition. At design conditions, high RMS values occupy approximately 10% of both the pitch and span. However, at 100% Nn near stall, hub corner separation occupies about 40% of both the pitch and span.
Similar behavior can be observed at the tip where there is an increase in the intensity of turbulence at the core of the tip leakage vortex moving from design point to near stall.

The hub-corner separation is more significant than the tip leakage flow phenomena. Therefore, the pronounced flow separation occurring at the hub may be regarded as the primary cause of the onset of rotating stall within the compressor.

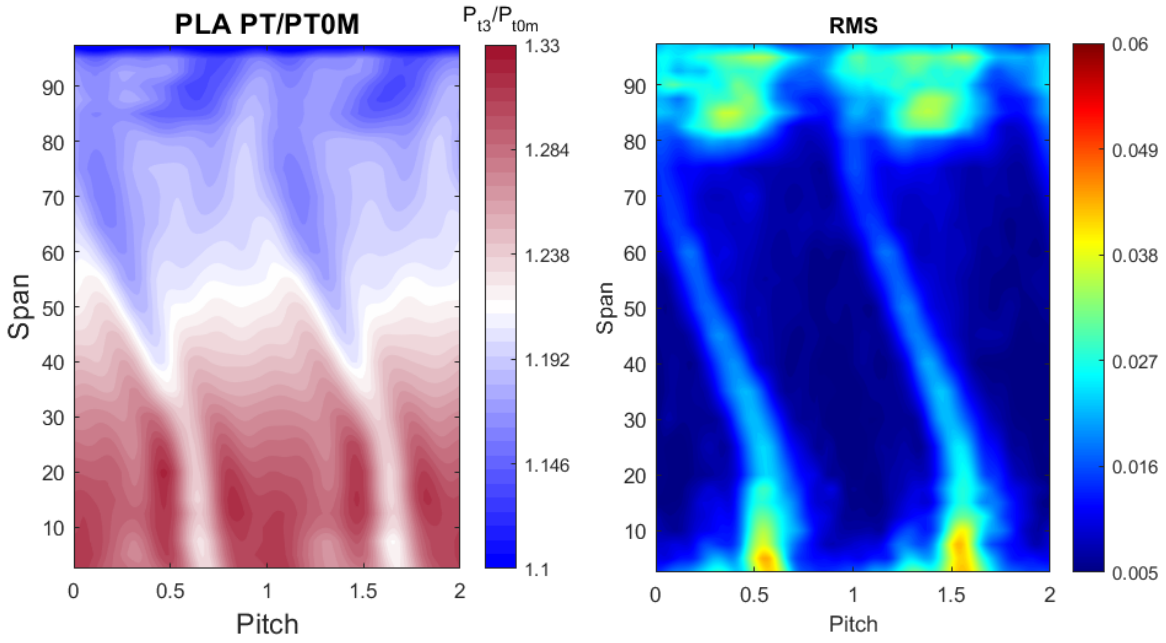

Figure 4.7: Total pressure phase locked average (PLA) map and corresponding RMS 100% Nn, design operating condition

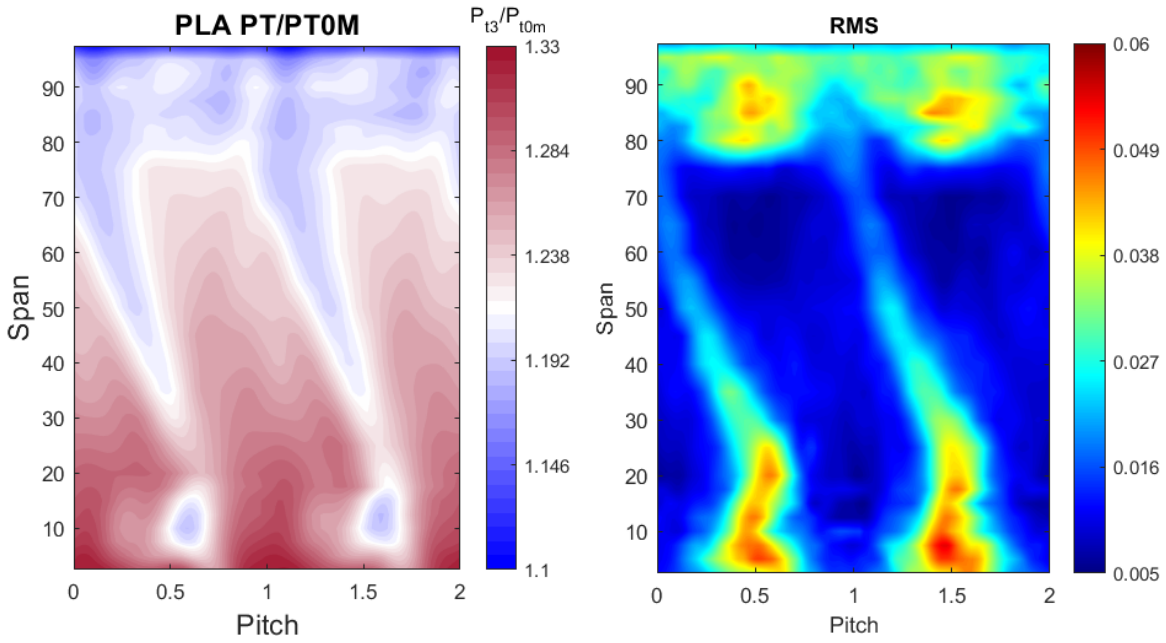

Figure 4.8: Total pressure phase locked average (PLA) map and corresponding RMS 100% Nn, near stall condition

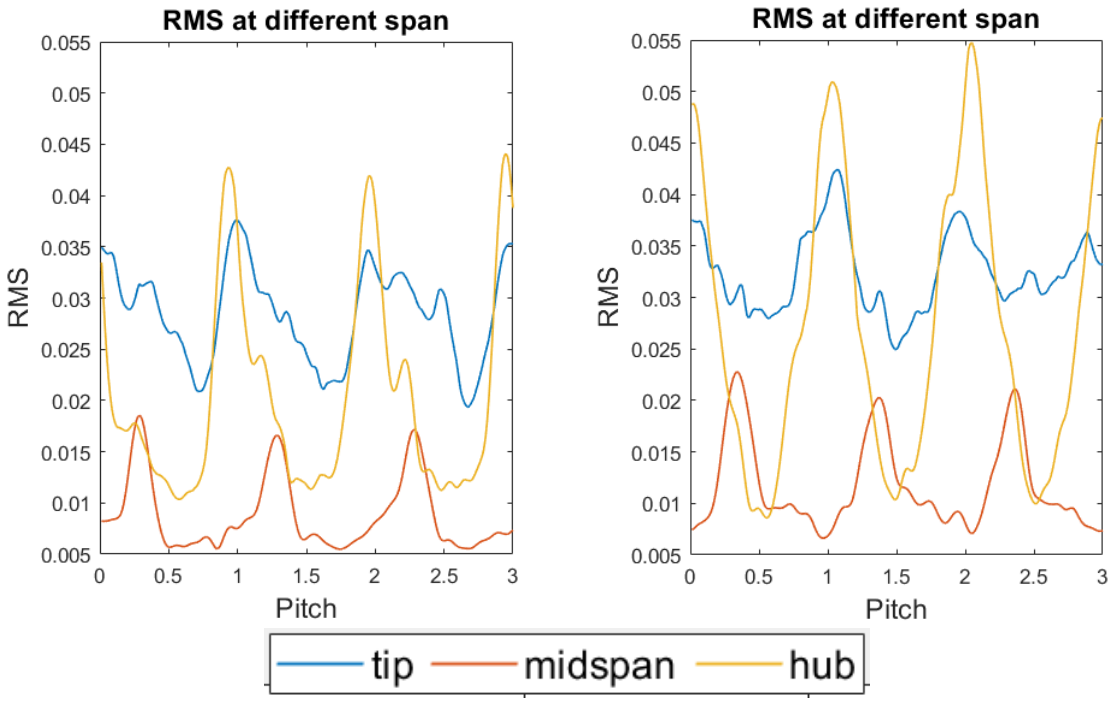

Figure 4.9: RMS signal comparison at different spans at 100% Nn

left: design condition

right: near stall condition

In the graph, it is evident that the RMS at the tip exhibits a high value, which can be attributed to all the unsteady phenomena associated with the passage of the blades such as the tip leakage flow and the tip leakage vortex which induce a high level of turbulence. Conversely, at midspan, the value is low, and the peaks associated with blade passage are barely noticeable. In the hub region, the RMS peaks related to blade passage are much higher, which could be explained by the presence of the hub corner separation, leading to a highly turbulent wake.

The analysis of fluid dynamic phenomena is focused primarily on total pressure and RMS maps, as these are sufficient to understand the evolution of these phenomena. Therefore, in the following sections, only these maps will be presented for the other two speeds.

Fig. 4.11 and 4.12 show the flow behavior at 96% Nn, using the same scale as the 100% Nn case for easy comparison. Notably, the reduction in speed and pressure ratio leads to a decrease in tip leakage intensity. Similarly, in the hub area, the hub corner separation phenomenon is less pronounced compared to 100% Nn case.

A notable escalation in the hub corner phenomenon is evident when transitioning from design to near-stall conditions, mirroring the pattern observed at 100% rotation speed. This is attributed to the reduction in flow rate, which leads to a decrease in axial speed, an increase in loading, and subsequently, a substantial enhancement of hub corner separation and tip leakage.

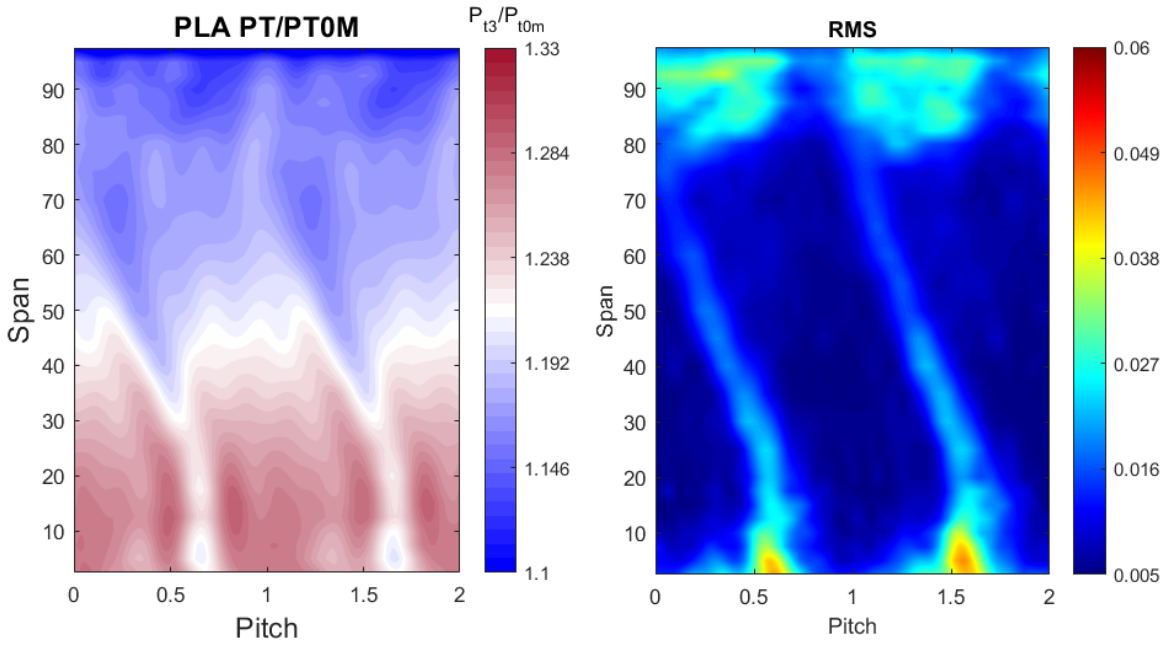

Figure 4.11: Total pressure phase locked average (PLA) map and corresponding RMS 96% Nn, design operating condition

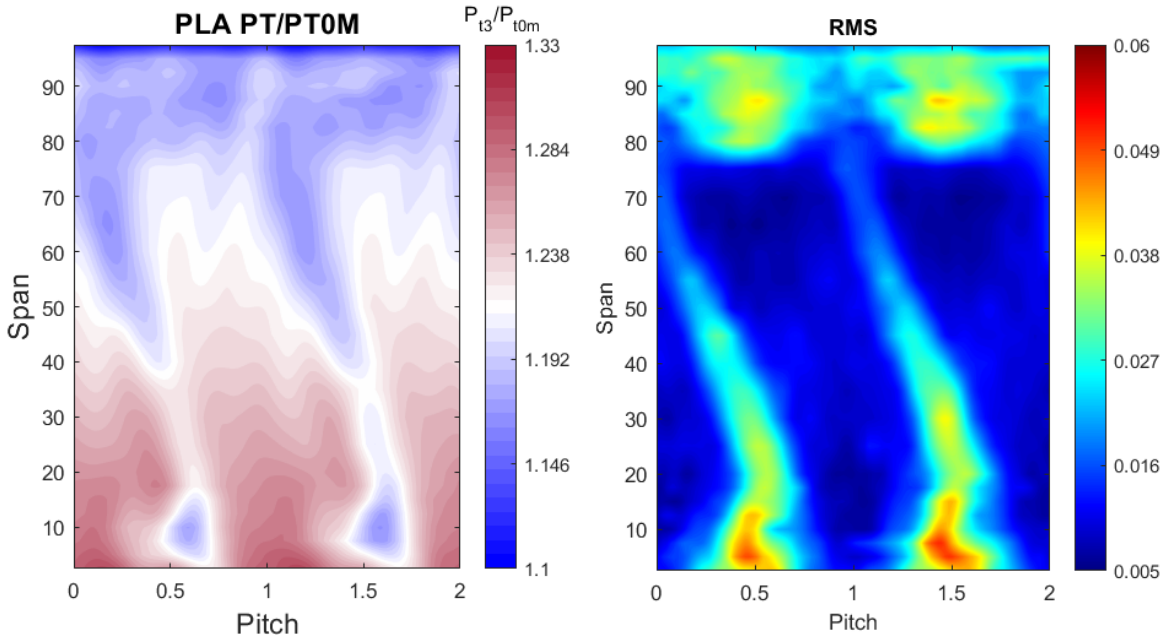

Figure 4.12: Total pressure phase locked average (PLA) map and corresponding RMS 96% Nn, near stall

In conclusion, even at 96% Nn, the primary cause of stall is the pronounced increase of the hub corner separation.
In all the 3D total pressure maps presented, the presence of a faint secondary wake at both speeds is revealed. The analysis of the power spectral density (PSD) of the total

pressure signal at midspan, after applying the transfer function, is presented (fig.4.13) and is obtained using the Pwelch method. Notably, the logarithmic scale values associated with 1BPF and 2BPF are within the same order of magnitude. This observation allows for a connection between the faint secondary wake observed in the figures and the second blade passing frequency (BPF).
Further investigations will be conducted to determine the underlying physical cause of this significant secondary Blade Passing Frequency (BPF).

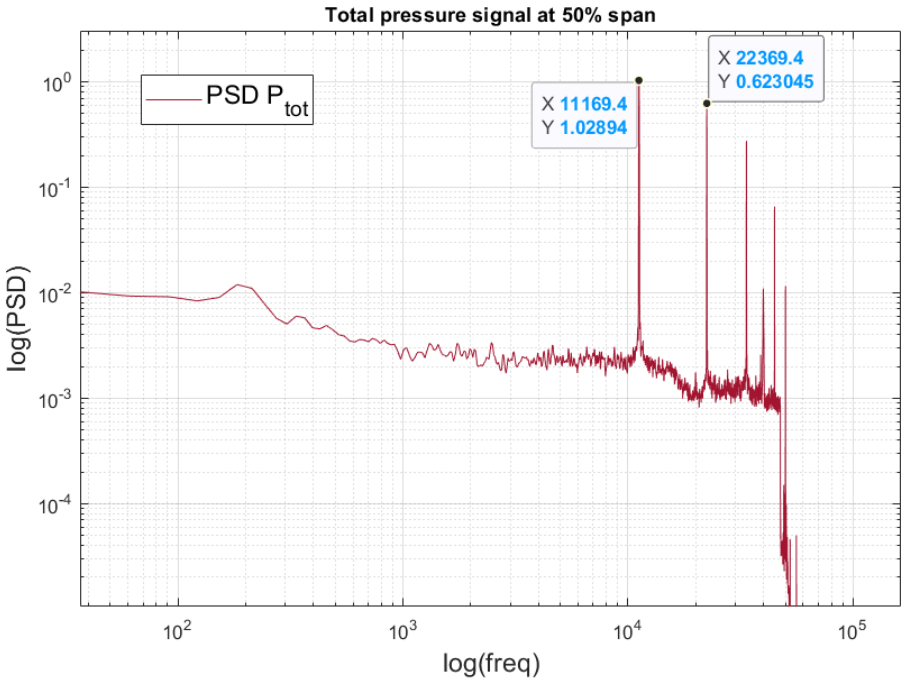

Figure 4.13: PSD of the total pressure signal at midspan for 96% Nn de

Fig. 4.14 and 4.15 describe the flow behavior at 90% Nn.
Comparable observations could be done to the conditions at the lower speed, mirroring those conducted at 96% Nn. The hub corner separation is notably diminished in the design condition, and similarly, the tip leakage flow is significantly reduced compared to higher speeds. Approching near stall conditions, the hub corner separation becomes pronounced once more, emerging as the primary factor contributing to the stall. In fig. 4.14, the distinct presence of the secondary wake associated with the 2BPF is prominently evident.

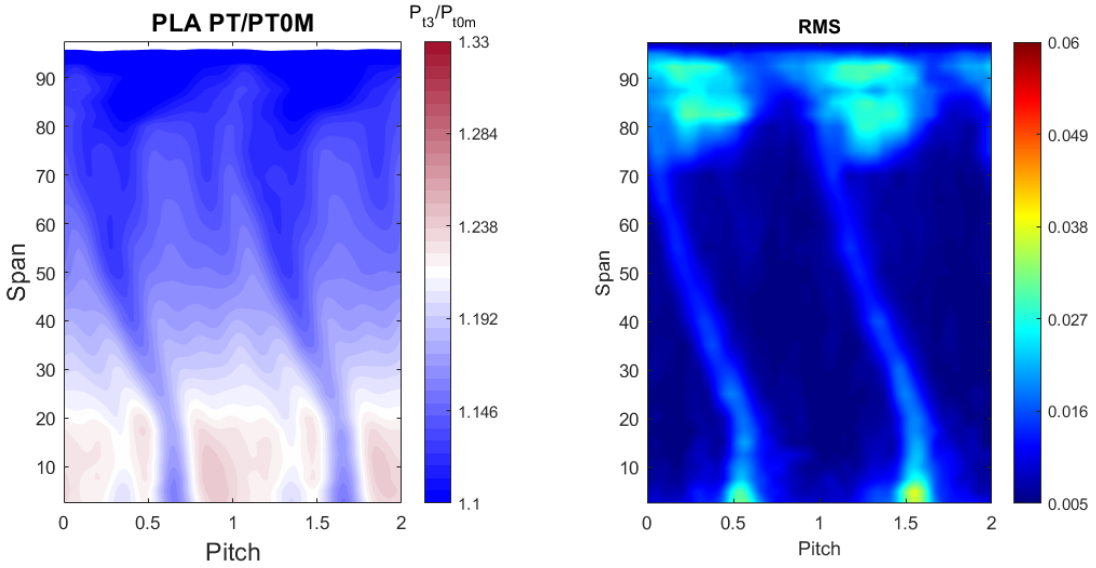

Figure 4.14: Total pressure phase locked average (PLA) map and corresponding RMS 90% Nn, design

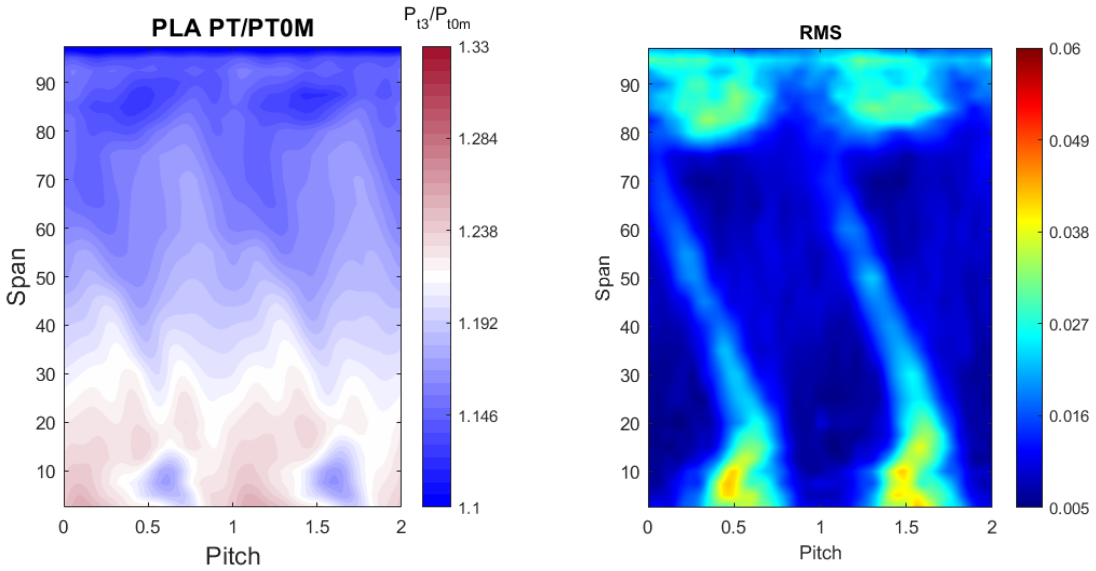

Figure 4.15: Total pressure phase locked average (PLA) map and corresponding RMS 90% Nn, near stall

4.2 Kulite casing sensors

The time-resolved pressure measurements obtained using the sensors discussed in Section 2.2.7 enable the examination of the flow near the rotor tip. The rotor casing static pressure is analyzed using the phase-locked averaging technique, which is employed for the fast response measurements and comprehensively explained in Appendix D. Axially, the interpolation domain is defined by the position of Kulite 14, located upstream of the rotor at -0.75 times the length of the chord, and Kulite 15, positioned downstream of the rotor row at twice the length of the chord. The locations of these Kulites are illustrated in Fig.2.23. Notably, Kulites 2, 4, 9, 10, 11, 12 and 13 were non-functional during the data acquisitions,Resulting in an ill-defined 3D map.
Concerning the circumferential extension of the interpolation domain, it corresponds to one rotor pitch. With the interpolation domain established, the subsequent step involves defining the interpolation grid. A 50x480 grid is chosen as it strikes an optimal balance between grid quality and computational efficiency. The selected interpolation method is linear. Lastly, it is worth noting that the interpolation direction does not align with the flow direction, limiting the overall quality of the generated maps.
To generate the 3D map, it is essential to consider the angular spacing between the sensors. These sensors span the rotor casing from its inlet to its outlet in the axial direction but are also displaced by 38° in the circumferential direction. Therefore, the signals need to be appropriately rephased. The angular spacing shift, denoted as $\Delta\theta$, corresponds to a time delay,ΔT, when considering a specific phenomenon rotating at an angular speed. This time delay, which requires compensation, can be expressed as follows:

$$\Delta T = \frac{\Delta\theta}{\Omega} \tag{4.1}$$

The non-dimensional casing wall static pressure field obtained with this interpolation is represented in fig.4.16, for the 100% Nn case at design and near-stall conditions. The solid black vertical lines represent the casing Kulites that were operational during the acquisition, while the white dotted lines represent the Kulites that were non-operational.

Initially, there is a static pressure increase from the upstream to the downstream of the rotor blades. This observation aligns with expectations, as the primary purpose of the rotor is to increase the pressure as the flow passes through its blades.
A second aspect in this pressure map is the existence of a low-pressure region along the suction side of the blade. This low-pressure area originates from the formation of the tip leakage vortex and its extent corresponds to its path within the flow passage, as elucidated in the literature review.
The extension of the tip leakage vortex within the flow passage corresponds to the pressure trough observed on the suction side of the blade.
Upon closer examination of these figures, it is possible to discern that the compressor

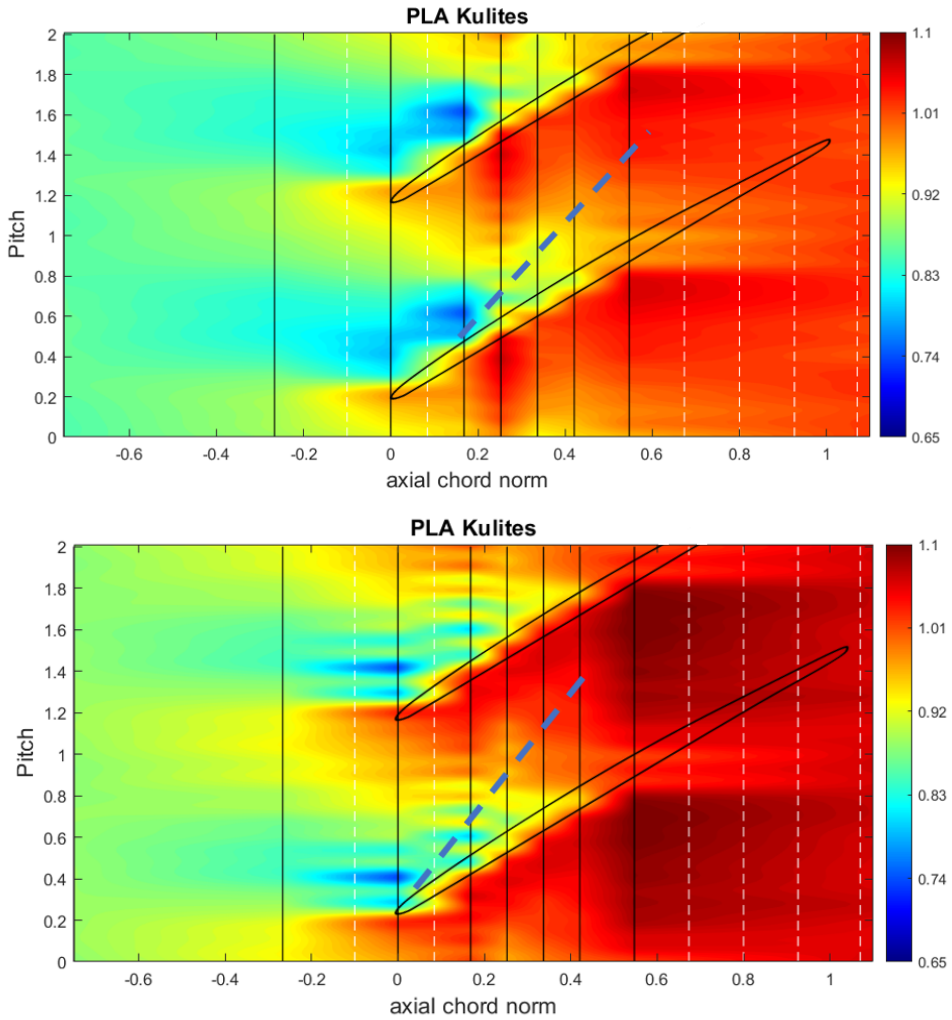

Figure 4.16: Wall casing static pressure ratio field at 100% Nn

Above: design condition

Below: near stall condition

throttling and the subsequent reduction in mass flow induce a significant change in the starting point of the tip leakage vortex. Specifically, the vortex's initiation point shifts towards the leading edge of the blades.

It is expectable also an increase in the vortex angle concerning the axial direction due to compressor throttling. This phenomenon arises from the dynamic equilibrium between the momentum of the primary flow and that of the tip leakage flow. Indeed, the main flow velocity is reduced by the throttling of the compressor while the intensity of the tip leakage flow is increased by the higher loading of the blades. Consequently, this alteration in momentum equilibrium between the primary and tip leakage flows results in a modification of the vortex angle.

Improving post-processing is essential for refining the tip leakage vortex representation. Incorporating stator angle direction interpolation offers an effective solution.

5
Conclusions

The first objective of this work was to conduct an extensive experimental campaign in the stable operating range of a state-of-the-art booster providing an overview of the leading mechanisms for aerodynamic stall in clean conditions while identifying the critical flow features for stability.

First, a description of the stage performance on the basis of total pressure and total temperature measurements by means of rakes located at the inlet and at the outlet of stage is provided.
A complete unsteady flow characterization at the rotor outlet is performed by means of a 3 hole-virtual fast-response pressure probe. This characterization is realized at three different rotational speeds: 100% Nn, 96% Nn and 90% Nn, as they represent the most relevant conditions for the development of critical structures driven by the increased incidence. Two different operating points were analyzed: design and near stall (close to the stability limit of the machine).
A phase-locked averaging (PLA) is applied to the unsteady pressure signals acquired at the rotor outlet, with the aim of assessing the averaged flow field in the relative frame of reference of the rotor. The RMS of the fluctuations was also computed. Rakes and 3 hole-virtual pneumatic probe were used to characterized the flow at the stage outlet.
The analysis of the performance highlighted the importance of the IGV/stator position on the computation of the pressure ratio and efficiency of the machine under investigation, with a maximum percentage variation up to 2.5% at design condition and 100% speed. Tracking the IGV/stator location and impact is therefore of primary importance to correctly quantify performance for future clean and distorted experiments.
As expected from the high loading and degree of reaction of the compressor at low span, the hub corner separation appears to be a critical flow feature possibly impacting aerodynamic stability. The core of the hub corner separation presents maximum unsteadiness up to 0.06 of the stage inlet total pressure. Despite the tip leakage/main flow interface does not exhibit any critical behaviour at the stall boundary, its evolution should be tracked

for future experiments as it appears as a second region of large unsteadiness.
Insights into the stator outlet flow field showed the impact of the IGV wake propagation at the stage outlet. Close to the stability limit of the machine an incidence variation of 6° is expected at the stator inlet, with consequent impact on the generation of possible separations on the stator blade.
Such flow survey allowed to quantify the performance of the compressor and identify the main sources of stability loss. This knowledge will be fundamental for the assessment of the distortion impact.

Appendix A
Aerodynamic calibration

The aerodynamic calibration for a 3-hole probe consists into creating maps that relates Ma and Yaw angle with 3 coefficients:Ktot, Kyaw and Kdyn defined as:

$$K_{tot}(Yaw, Ma) = \frac{P_0 - P_c}{P_c - P_{avg}}$$

$$K_{yaw}(Yaw, Ma) = \frac{P_l - P_r}{P_c - P_{avg}}$$

$$K_{din}(Yaw, Ma) = \frac{P_s - P_{avg}}{P_0 - P_{avg}}$$

where P_0 is the total pressure,P_s the static pressure, while P_{avg} is the mean value of P_{left} and P_{right}.
Once the coefficient curves are obtained from the aerodynamic calibration, during the tests P_{left}, $P_{central}$ and P_{right} been measured. Later, an iterative procedure (summarized in Figure 5.1) computes the Mach, the yaw, the static and the total pressure.

The iteration starts with an initialization step, assuming that the total pressure is equal to P_c and the static pressure is obtained either from the pressure tap interpolation or from the virtual approach using P_{avg}.
Subsequently, K_{yaw} is computed following the Equation expressed before, while the Mach number is derived from the isentropic flow equation.
By inverting the relationship between K_{yaw}, Mach number, and yaw angle, an initial estimate for yaw angle is obtained. Using this estimate, the other coefficients $K_{tot}$and K_{din} can be determined, resulting in new values for P_0 and P_s as well as Ma, which are then utilized as inputs for subsequent iterations. The iterative process concludes when the absolute difference between the new and old Mach numbers falls below a prescribed threshold, denoted as ϵ.

An example of the calibration is reported in fig.5.2

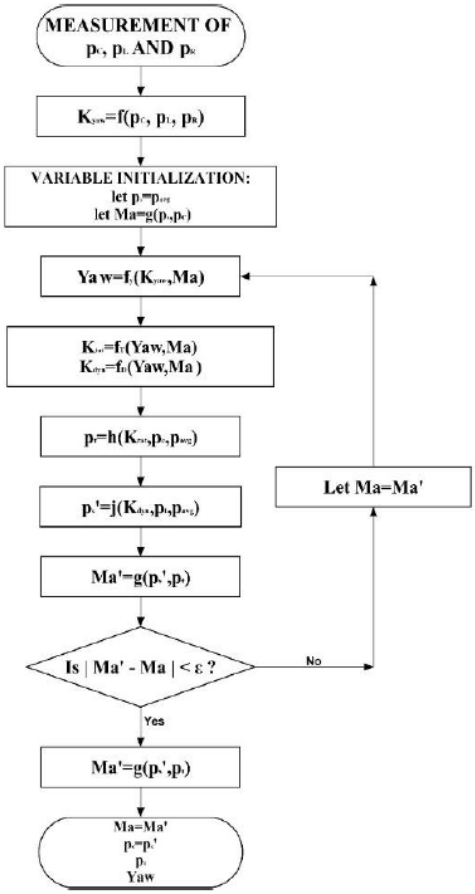

Figure 5.1: Iterative method

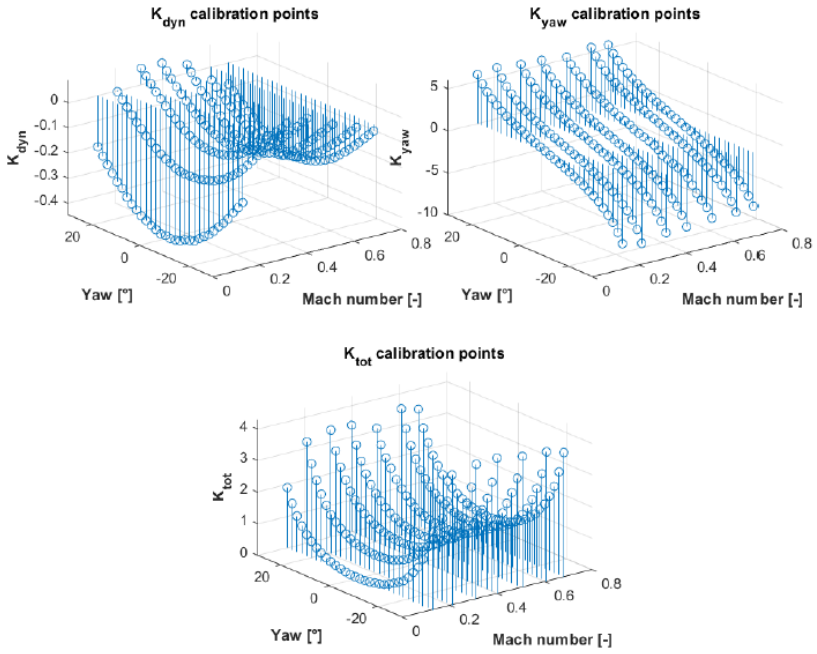

Figure 5.2: Calibration curves [9]

Appendix B
Post-processing from raw data to performance map

The acquisition system allows for the creation of a .log file that records all events that occur during the acquisition process. This .log file is then processed by a MATLAB routine, the methodology of which is extensively explained in [17]. Subsequently, the same .log file undergoes post-processing through a series of steps outlined below:

Removing the outliers

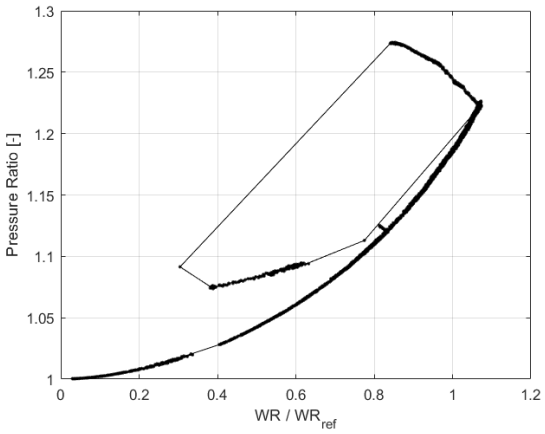

Figure 5.3: Total to total pressure performance map with .log file

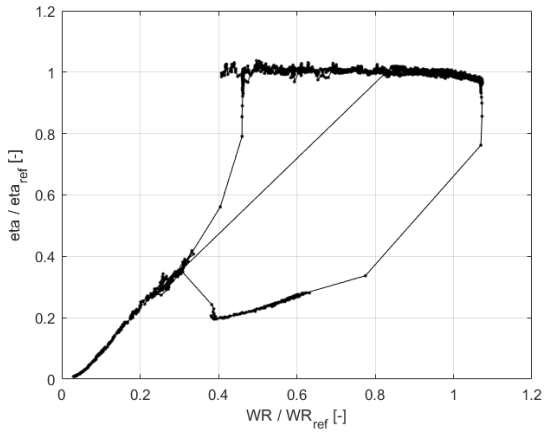

Figure 5.4: Efficiency performance map with .log file

In Fig.5.3 and Fig.5.4, it is evident that during the acquisition process, outliers in the data can be encountered. The routine allows for the manual removal of these values, thus providing the ability to choose which ones to retain.
Fig.5.5 and Fig.5.6 highlight in red the selected data points after the removal of outliers.

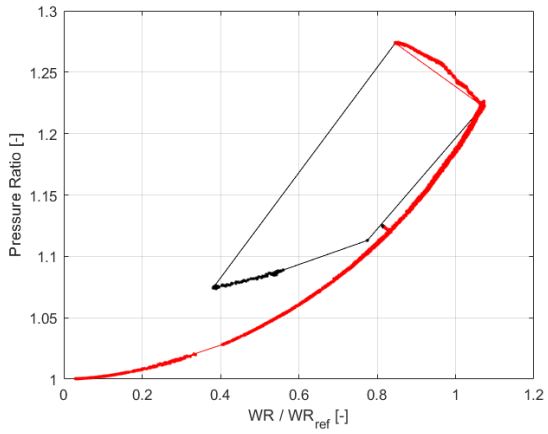

Figure 5.5: Removing outliers from total to total pressure performance map

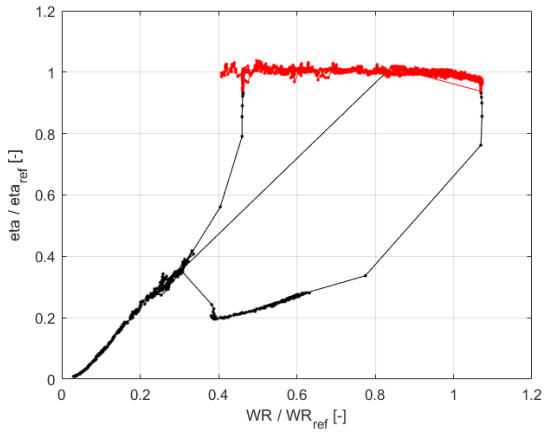

Figure 5.6: Removing outliers from efficiency performance map

After removing outliers, it is possible to consider the option of discarding some of the acquired traces. The acquisition process can be segmented into distinct traces, as illustrated in fig.5.7. One trace can be recorded until it attains the desired number of revolutions, denoted as "Trace 1" in the figure. Subsequently, a new trace can be generated exclusively containing data related to the compressor map, designated as "Trace 2." This approach facilitates streamlined post-processing, enabling the selective viewing and storage of just the raw compressor map-related data depicted in fig.5.8 and 5.9

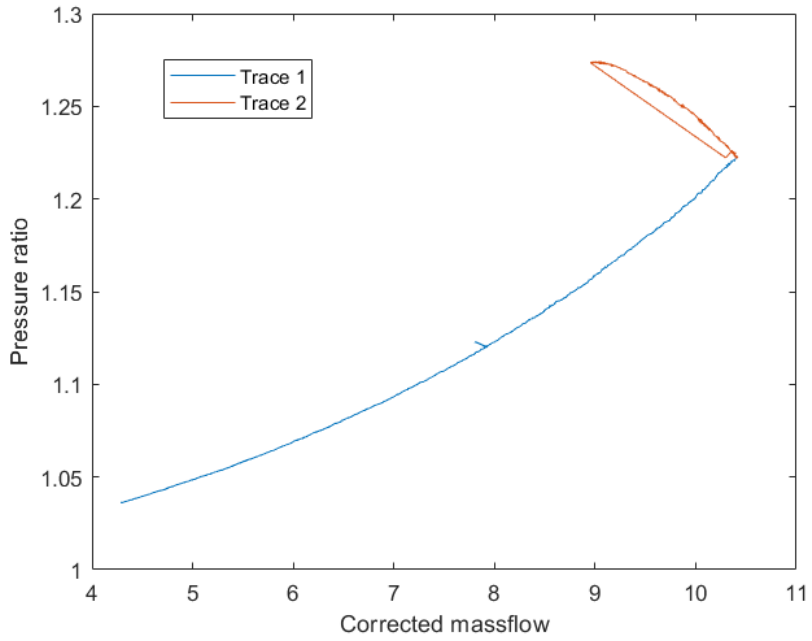

Figure 5.7: Example of different traces

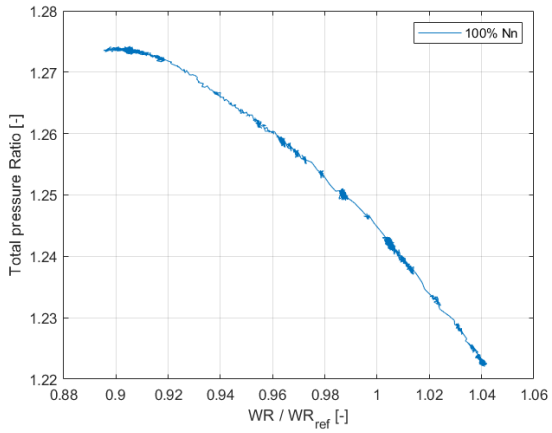

Figure 5.8: Raw total to total pressure performance map 100Nn

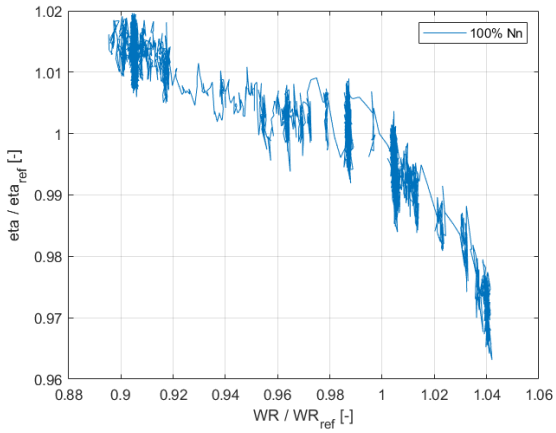

Figure 5.9: Raw efficiency performance map 100Nn

Subsequently, the script proceeds to perform the averaged maps using a method called 'Loading line averaging'.The loading line-averaging method lies in the circuit characteristic curve, defined by the equation 5.1, where λ is the throttle valve discharge coefficient, mainly dependent on the throttle valve position, and is defined in the static to total performance map.

$$\beta_{static} = 1 + \lambda \cdot Q_m^2 \tag{5.1}$$

The choke and near stall conditions identify the λ_{CH} and λ_{NS} by substituting their re-

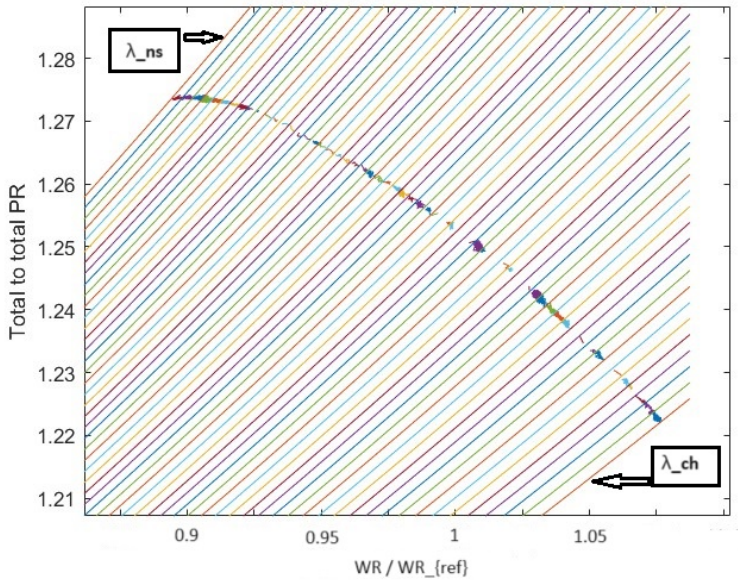

Figure 5.10: loading line averaging method.

spective mass flow and static pressure ratio values in equation 5.1. Hence, the λ_{CH} and λ_{NS}, identify the minimum and maximum discharge coefficients in the regulation range as it showed in fig.5.10

The method divides the latter into a finite number of classes with a $\Delta\lambda$. Next, the data points falling within the classes are averaged with respect to WR, β, and efficiency, and finally, their standard deviations are computed. Fig.5.10 summarizes the procedure for determining the data points within the intervals with 50 classes being chosen.
Fig.5.11and fig.5.12 represent the compressor maps for total pressure ratio and efficiency, with standard deviation after the averaging post-processing.

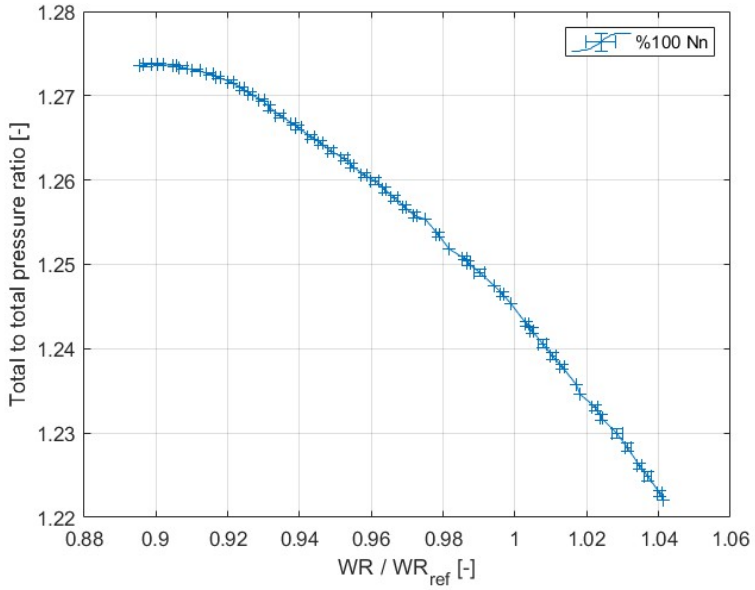

Figure 5.11: Averaged total pressure ratio performance map 100Nn

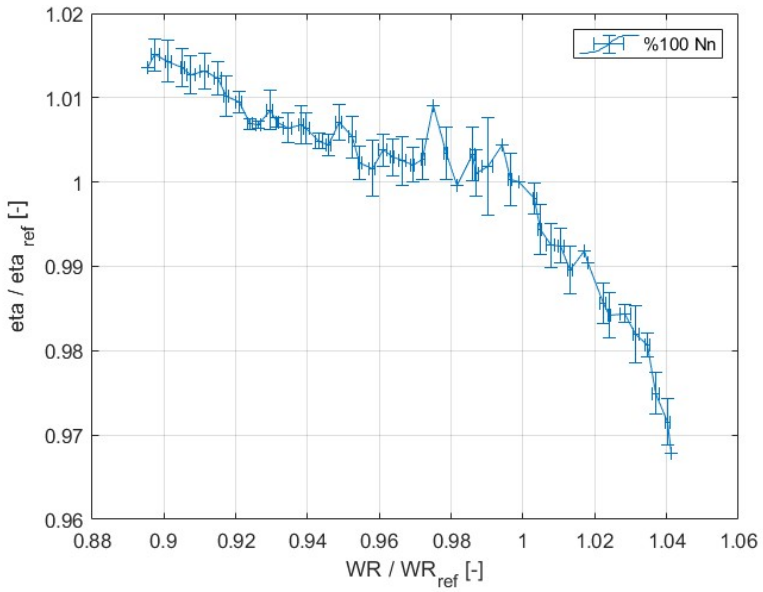

Figure 5.12: Averaged efficiency performance map 100Nn

Appendix C
Assessment of Mach number and mass flow at plane 4

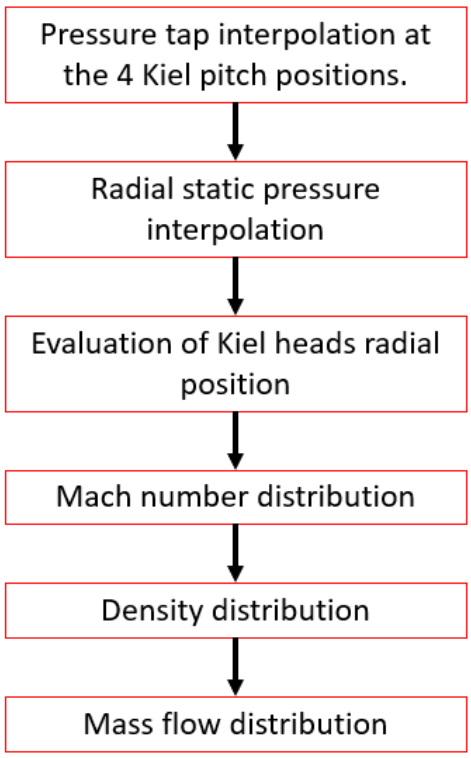

Figure 5.13: Flowchart for mass flow distribution evaluation.

In plane 4, five pressure taps were strategically positioned at both the hub and the tip to cover the rotor's flow field. Additionally, four rake probes were placed in corresponding positions. Arranging the six Kiel probes radially on the rake probes, total pressure was radially distributed at the four rake positions.
Linear interpolation was conducted using the five pressure values at both the hub and tip, utilizing only the four static pressure values corresponding to the rake's pitch position.

As indicated by the Computational Fluid Dynamics (CFD) results, static pressure demonstrates a predominantly linear trend mainly due to radial equilibrium. Therefore, linear interpolation is a valid approach for deriving intermediate span values, introducing minimal error.
Following the establishment of radial positions for the Kiel probes, six radial values for total pressure and static pressure were determined for the four rake probe positions, enabling Mach number calculations using the equation:

$$Ma = \sqrt{\left(\frac{P_{tot}}{P_s}^{\frac{\gamma-1}{\gamma}} - 1\right) \cdot \frac{2}{\gamma - 1}} \tag{5.2}$$

This process yielded distributions of total pressure and Mach number. Total temperatures were measured by thermocouples on the rake probes, and static temperature distributions were assessed using equation 5.3:

$$T_s = \frac{T_{tot}}{1 + \frac{\gamma-1}{2} Ma^2} \tag{5.3}$$

Subsequently, density distribution was determined based on the ideal gas law, using static temperature and static pressure distribution.
The velocity was computed from static temperature and Mach number using the speed of sound equation. With this information, along with knowledge of density, velocity, and area (total area divided by 6, as Kiel probes cover equal areas), the flow rate distribution was derived.

Appendix D
Post-processing data fot fast-response pressure probe

In this section, a summarized procedure of how the raw signal output from the fast-response probe is transformed into a Phase Lock Average (PLA) signal will be presented. The analysis will focus on the case corresponding to 100% of Nominal Speed (Nn) and midspan position.
The probe is positioned at midspan and it acquires data in a virtual mode. The probe records data for 1 second at a frequency of 500 kHz, resulting in a voltage signal composed of 500,000 data points for each position (left, central, and right). These voltage signals then undergo a static calibration process, converting them from volts to pressure. An example of a raw signal converted into pressure is shown in Fig.5.14.

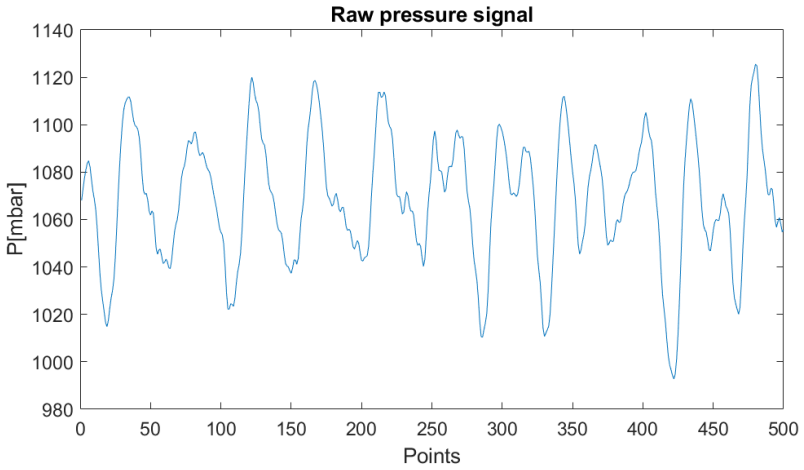

Figure 5.14: Signal of $P_{central}$ after the static calibration

Subsequently, a Transfer Function (TF), obtained through dynamic calibration as detailed in [9] and [20], is applied to each of the three signals. Once the TF is applied, Fig.5.15 illustrates how the signal changes significantly from the raw signal. This discrepancy is normal as the Transfer Function alters the signal's amplitude at specific frequencies and the phase. After correctly applying the Transfer Function, the signals are filtered at 60

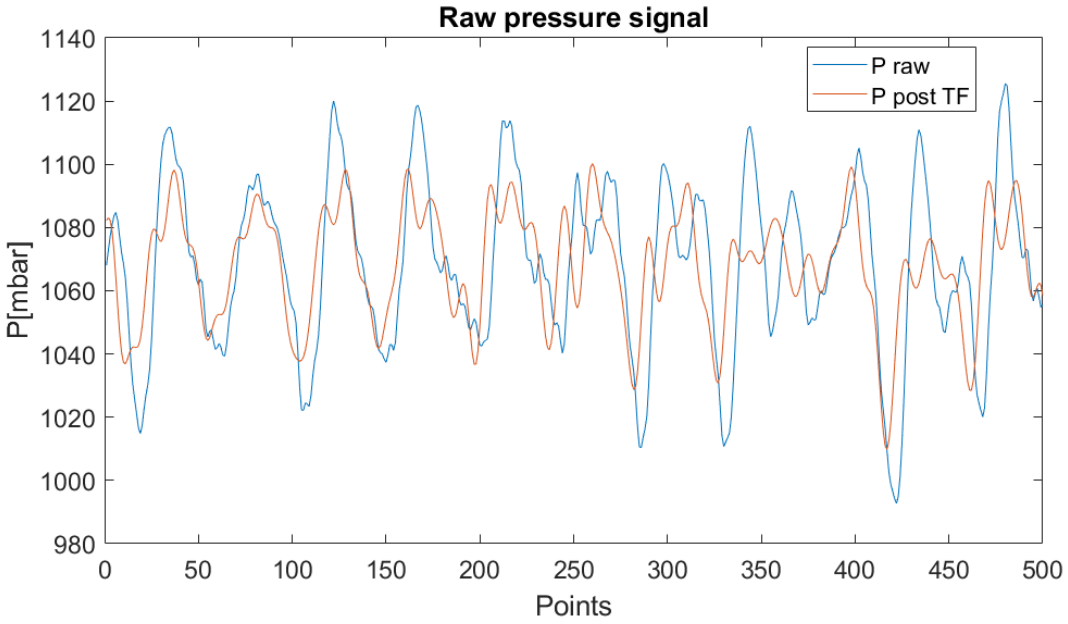

Figure 5.15: Comparison between $P_{central}$ raw and $P_{central}$ after the application of the TF

kHz. This choice is due to the fact that, at 100% of Nominal Speed (Nn), a bandwidth of approximately 11 kHz is obtained, and filtering at 60 kHz ensures the analysis covers up to the fifth armonic, which has been determined as the optimal value for this study.
Temporal synchronization of the signals is necessary since the acquisitions of the P_{left}, $P_{central}$, and P_{right} signals do not occur simultaneously. To achieve this, the "one rev" signal generated by the motor driving the compressor is utilized. The "one rev" signal is obtained through an optical device installed on the rotor shaft, allowing for the counting of rotor revolutions during data acquisition. This signal is used since the rotational speed may experience minor fluctuations to maintain a constant corrected rotational speed. In the event of an increase in the inlet total temperature, the mechanical rotational speed is adjusted to ensure the corrected rotational speed remains constant. The MATLAB routine uses the initial peak of the "one rev" signal to initiate each pressure signal (P_{left}, $P_{central}$, and P_{right}) from the same temporal point, ensuring that the signals start simultaneously. This method is summarized graphically in fig.5.16 and 5.17.

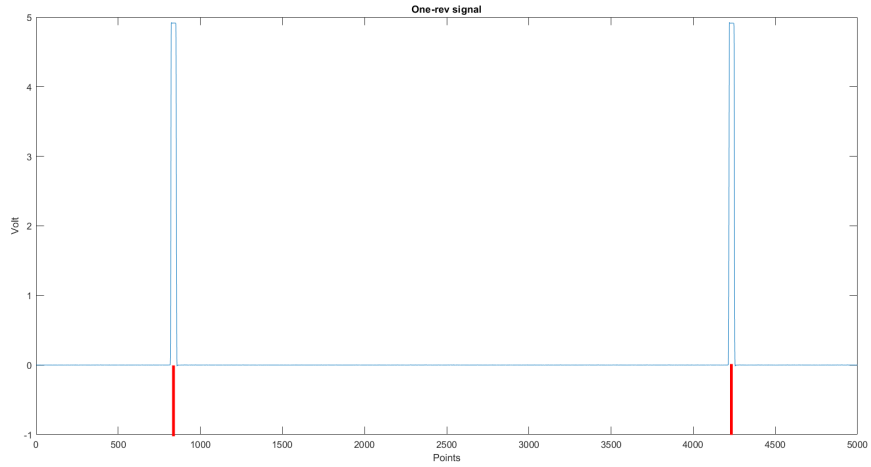

Figure 5.16: Signal One-rev acquired with $P_{central}$

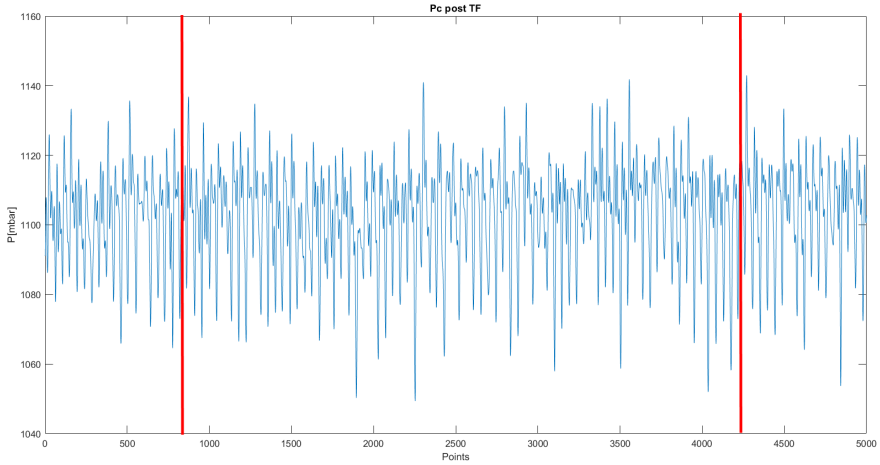

Figure 5.17: $P_{central}$ post TF corresponding to one revolution

The data acquisition was conducted at a sampling frequency of 500 kHz over a duration of 1 second, resulting in a dataset of 500,000 data points. Under conditions of 100% Nn, the rotational speed was 8748 rpm.
using equation 5.4 the probe yielded 3430 data points per revolution, equivalent to 45.6 data points per blade pitch.

$$500,000[\frac{points}{s}] \cdot \frac{1[min]}{8748[rev]} \cdot \frac{60[s]}{[min]} = 3430\frac{[points]}{rev} \tag{5.4}$$

To ensure a consistent and precise data resolution per blade pitch, thereby mitigating potential variations in angular velocity, a data interpolation was employed. An interpolation grid of 80 data points per pitch, amounting to 6080 data points per revolution, was chosen for this purpose. The results of this interpolation are presented in fig.5.18.

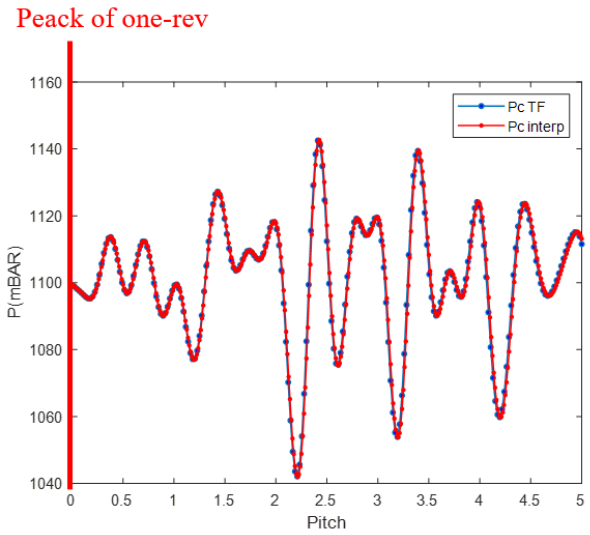

Figure 5.18: $P_{central}$ interpolated on 6080 points per revolution

In conclusion, the pressure signals undergo the steps of Transfer Function (TF) application, filtering, temporal synchronization, and interpolation before applying the aerodynamic calibration previously executed [9] to obtain the final values of total pressure, static pressure, Mach number, and yaw angle signals for each point of the span.

Phase lock average

A closer examination of specific blade passages within the static pressure signal, recorded by the fast response, is depicted in Fig.5.19. The horizontal dashed line in the graph represents the average pressure level. A blade passage can be discerned between two pressure drops, which correspond to the passage of an individual blade in front of the fast response pressure sensor. The periodicity of the signals governed by the blade passing

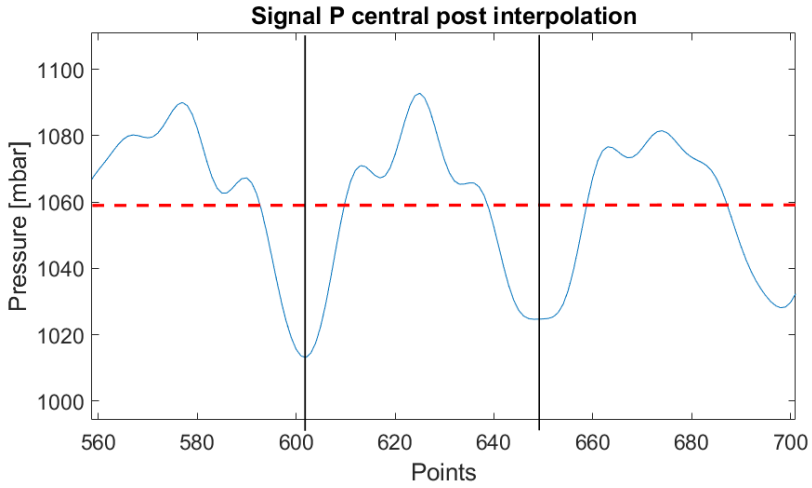

Figure 5.19: $P_{central}$ interpolated signal from fast response at 100% Nn design conditions

frequency enables to average them over one blade passage. After interpolating the signal, the number of points per revolution will be known. The interpolated signal is averaged among multiple revolutions to provide a representative average of the flow in the relative frame of reference of the rotor. This procedure of averaging the signal is called Phase Lock Average (PLA). The PLA process is applied to the signal after the aerodynamic calibration for each position of the span. An example of the PLA signal at 50% and 55% of the span is provided in fig.5.20.

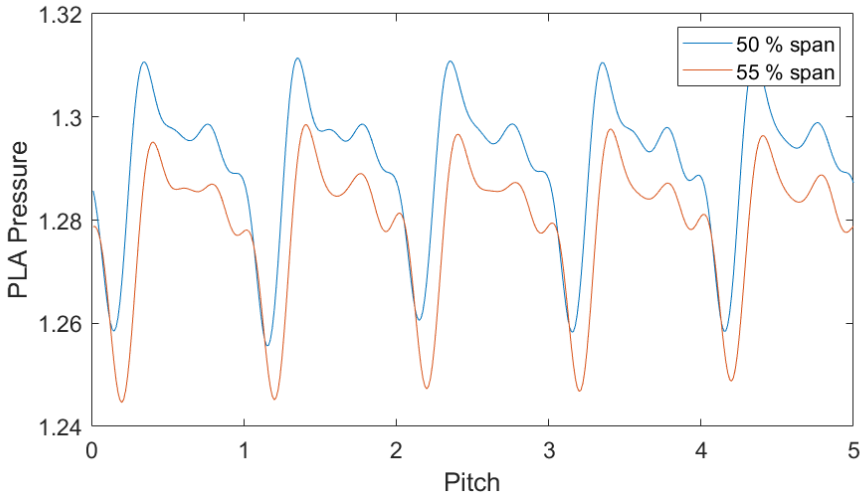

Figure 5.20: PLA of pressure signal at 100% Nn design point for two different span position

Root mean square (RMS)

Considering the significant number of blade passages within each acquisition, it becomes feasible to ascertain the variations in pressure for all blade passages in relation to the pressure profiles derived from the PLA process. This determination is accomplished by employing the RMS, defined as follows:

$$RMS = \sqrt{\frac{\sum_{i=1}^{N} (P_i - P_{avg})^2}{N}} \tag{5.5}$$

Bibliography

[1] C. T. G.T. Chen, E.M. Greitzer and F. Marble., "Similarity analysis of compressor tip clearance flow structure." *Journal of Turbomachinery,*, vol. 113, no. 2, pp. 260–271, 1991.

[2] . C. N. A. Storer, J. A., "Tip leakage flow in axial compressors," *Journal of Turbomachinery,*, vol. 113, no. 2, 1991.

[3] E. M. G. V-M. Lei, Z. S. Spakovszky, "A criterion for axial compressor hub-corner stall," *ASME Turbo Expo 2006*, May 8-11,2006.

[4] N. C. S.A. Gbadebo and T. Hynes., "Three-dimensional separations in axial compressors." *Journal of Turbomachinery*, 2005.

[5] N. HABOTTE, "Analysis of the stall inception process of a highly loaded low-pressure compressor stage," *Von Karman Institute for Fluid Dynamics*, Rhode-St-Genese, Belgium, 2013 - 2014.

[6] R. G. D. G. Norris and A. D. Smith, "Strut influenceswithin a diffusing annular s-shaped duct," *Volume 1: Turbomachinery. American Society of Mechanical Engineers,*, June 1998.

[7] B. C., "Impact of shrouded stator cavity flow on axial compressor performance and stability," *PhD Thesis, École Centrale de Lyon*, 2022.

[8] G. Dell'Era, "Experimental characterization of instability onsets in a high-speed axial compressor," *PhD Thesis,Von Karman Institute for Fluid Dynamics,Universitè catholique de louvain*, Rhode-St-Genese, Belgium, May 2017.

[9] A. Ferro, "Performance analysis and calibration campaign for the characterization of a highly loaded low-pressure compressor stage," rhode-St-Genese, Belgium,2022.

[10] L. H. Smith, "Wake ingestion propulsion benefit," pp. 74–82, 1993.

[11] E. J. Gunn and C. A. Hall, "Aerodynamics of boundary layer ingesting fans," *Turbine Technical Conference and Exposition*, 2014, Düsseldorf, Germany.

[12] C. Huges, "The promise and challenges of ultra high bypass ratio engine technology and integration," *NASA Glenn Research Center*, January 4 July 2011.

[13] U. S. H. Saathoff, "Tip clearance flow-induced end wall boundary layer separation in a single-stage axial-flow low-speed compressor," *Turbo Expo, Paper 2000-GT-0501,*, Munich, Germany,May 2000.

[14] H. Schultz and H. Gallus., "Experimental investigation of the three- dimensional flow in an annular compressor cascade." *Journal of Turbomachinery*, 2008.

[15] J.-F. B. Jerome Sans, "Dream project: Experimental study of two highly loaded low pressure compressors," *Von Karman Institute for Fluid Dynamics*, Rhode-St-Genese, Belgium, 2011-2012.

[16] Intelligent temperature scanner. [Online]. Available: https://scanivalve.com/products/temperature-measurement/dts-4050-intelligent-temperature-scanner/

[17] F. Fontaneto, "Report of the post-lemcotec measurement campaign," *von Karman Institute for Fluid Dynamics*, Rhode-St-Genese, Belgium, May 2020.

[18] N. Habotte, "Analysis of the stall inception process of a highly-loaded low-pressure compressor stage," *Master thesis, Universitè de Liege*, 2022.

[19] D.Pastrone, "Aeronautical engines," *Course notes, Politecnico di Torino*, 2022.

[20] B. E, "Development of methods for the characterization and uncertainty assessment of turbulent quantities in high speed compressible flows by hot wires and fast response pressure probes," *PhD Thesis, Universitè Catholique de Louvain,*, Rhode-St-Genese, Belgium,2021.